University of Southern Queensland
Faculty of Engineering & Surveying

In-Cylinder Radiation Heat Transfer in a Small Direct Injection Diesel Engine

A thesis submitted by

Mior Azman Meor Said

B.Eng., M.Sc.

in fulfilment of the requirements for the degree of

Doctor of Philosophy

Submitted: July, 2012

To my beloved parents, siblings, members of my extended families,
friends, colleagues and special ones.

Abstract

Diesel engine downsizing is of current interest because of the finite nature of crude oil reserves and the high efficiency of the diesel cycle. Scaling and downsizing studies can make substantial contributions to the optimization of small diesel engine designs but the scaling of heat transfer losses has not been the focus of recent studies. Radiation heat transfer can represent a significant fraction of the total in-cylinder heat transfer of the diesel engine and hence, developments in radiation heat transfer scaling can have an impact on the success of the overall diesel engine scaling efforts.

The present work contributes new radiation heat transfer data from a small direct injection diesel engine and investigates the relationship between radiation heat transfer and engine size. A radiation heat flux probe was developed based on the optical two-colour method. It was used to measure instantaneous radiation heat flux and the associated parameters KL and apparent flame temperature for a 0.21 L direct-injection diesel engine at 4 operating conditions giving indicated power values between 1.0 and 2.1 kW. A convective heat flux probe was also developed and used in the same engine for the measurement of instantaneous convective heat flux at these same operating conditions. In the radiation heat flux measurements, an approach based on post-run calibration of the probe in its sooted state was adopted to compensate for the problem of signal attenuation by probe sooting. In the convection heat flux measurements, the sooting problem on the thermocouple probe was compensated by deduction of the soot layer thickness

through the tuning of results during compression to match the motoring results obtained with a soot-free probe.

The radiation heat flux results from the present work are compared with results from other works which have used engines of a larger scale and the present radiation heat flux data are at the lower end of the overall range. The peak radiation values obtained in the present work are in the range of 0.14 to 0.38 $\mathrm{MW/m^2}$ which is about half the magnitude obtained with the nearest engine size reported in the available literature. These results point to the significant influence of the soot cloud volume in the radiation heat flux losses.

The convective heat flux values obtained in this work are in the same range of values identified from other published works. However, relative to the existing literature, the present work has produced the smallest values for the ratio of radiation heat flux to convective heat flux in terms of both peak and time-averaged values. This result also reflects the significant influence of engine size on radiation heat flux.

A radiation heat flux scaling analysis was performed based on the time-averaged and peak radiation heat flux experimental data from the present work and other published literature. The indicated power per unit piston area, IP/A_p has been adopted as a scaling parameter. The time-averaged data appears to be linearly related to IP/A_p while the peak radiation heat flux appears to scale via a power law relationship with an index of 0.83. The linearity of the time-averaged radiation heat flux scaling implies that the time-averaged radiation heat flux is strongly influenced by flame size effects while the peak radiation heat flux results are also influenced by emissions originating from soot particles near the surface of the flame.

A new empirical radiation model based on available KL data from various sources including the present work has been developed and implemented in a thermodynamic engine simulation tool. Results from these simulations support the notion

that both time-averaged and peak radiation heat flux are influenced by flame scale but that the peak radiation results are more strongly affected by emissions from soot particles near the flame surface.

Certification of Dissertation

I certify that the ideas, designs and experimental work, results, analyses and conclusions set out in this dissertation are entirely my own effort, except where otherwise indicated and acknowledged.
I further certify that the work is original and has not been previously submitted for assessment in any other course or institution, except where specifically stated.

Mior Azman Meor Said

W0082539

_____

Signature of Candidate

_____

Date

ENDORSEMENT

_____

Signature of Supervisor/s

_____

Date

Acknowledgments

I would like to acknowledge the academic and technical staff of the University of the Faculty of Engineering Southern Queensland for their contributions to the work resulting in this dissertation. I would like to especially thank my principal supervisor Professor David Buttsworth for his guidance, technical assistance and strategic advice over the duration of my PhD. My Associate supervisor, Assoc Prof Talal Yusaf contributed grounding advice, especially early in the candidature. I would also like to thank Dr. Ray Malpress for his advice and assistance in the fabrication of the probes, during engine tests and other lab work. The University of Queensland's Centre for Hypersonics are thanked for the use of their calibrated 1000 W lamp for the absolute calibration work reported herein. I also wish to thank my family, friends and fellow students who have contributed directly or indirectly to this work in a variety of ways.

Mior Azman Meor Said

University of Southern Queensland

July 2012

Contents

List of Figures

List of Tables

List of Acronyms

ATDC	After Top Dead Centre
BMEP	Brake Mean Effective Pressure
BP	Brake Power
BTDC	Before Top Dead Centre
CA	Crank Angle
CFD	Computational Fluid Dynamic
CIPR	Combustion Induced Pressure Rise
DAQ	Data Acquisition System
DI	Direct Injection
IC	Internal Combustion
IP	Indicated Power
IRIS	An Internal combustion engine simulation code
IMEP	Indicated Mean Effective Pressure
KL	KL Factor
LDV	Light Duty Vehicle
LHR	Low Heat Rejection
NA	Not Available

RPM	Revolution Per Minute
RHF	Radiation Heat Flux
RHT	Radiation Heat Transfer
TDC	Top Dead Centre
USQ	University of Southern Queensland

Chapter 1

Introduction

1.1 Future Prospects for Diesel Engines

With the prospect of fuel resource scarcity and the existence of climate change phenomena, the call for highly efficient and environmentally friendly internal combustion engines is now louder than ever. Diesel engines, which are widely used not only in automobiles but also in heavy vehicles and machines including trucks, boats and construction machines, have been given greater attention in the field of internal combustion engine research and development. The demand for diesel engines in the ever-expanding industry - automobile, agriculture, marine, mining, power generation, construction among others - is growing strongly in the face of high fuel prices and the increasing population, due to their high power and efficiency.

In the automobile industry, money-conscious new-vehicle consumers prefer diesel engine-powered cars to hybrid-powered cars. More than 23 percent of the total new consumers opted for clean diesel engines in 2007 which was double that of the previous year [10]. A report by UBS Limited in collaboration with Ricardo,

forecasts that the sales of diesel-powered vehicles in the US alone will be 1.5 million vehicles, which will be significantly larger than those of the hybrid-powered vehicles which will be at 1.2 million vehicles in 2012 [11]. In Europe, diesel engine-powered cars have accounted for around 50% of light-duty vehicles (LDV) sales over the past several years prior to 2012 [12].

It appears that no other power source used in agriculture, mining and construction industries is as reliable and durable as the diesel engine. The diesel engine has been the main workhorse that propels heavy machinery, moves huge structures and extracts earth materials. With the new generation of clean technology - ultra-low sulfur diesel fuels, advanced engine controls, emission controls technology - the diesel engine's place as a primary power source which can still conform to necessary emission regulations appears secure. Some of the largest diesel engines are used in the marine industry for transportation of millions of tons of freight each year. The economic importance of diesel engines in marine transportation cannot be overestimated as no other power source could match its efficiency, fuel economy and power.

New environmental regulations have driven the effort to produce clean and efficient diesel engine technology and have elevated the diesel engine as a viable environmentally friendly power source. The stricter Euro 6 Emission Legislation which stresses reducing the number of particulates and NOx has encourage developments in innovative emission technology such as diesel particulates filtering, selective catalytic reduction, advanced exhaust gas aftertreatment and the exhaust gas stream energy recuperation [13]. The debut of ultra-low sulfur diesel fuels and other biodiesel fuel developments have been helping diesel engine technology emerge as a popular technology platform for targetting ultra-low emissions.

Along with the advent of new diesel engine technology designed to reduce emissions, such as advanced engine electronic combustion control, advanced fuel injection systems, alternative fuels and ultra low sulfur diesel fuels, more emphasis has been placed on the development of highly efficient diesel engines [14].

1.2 Small Engines and Scaling Studies

Due to its high thermal efficiency and near-term manufacturing feasibility, small displacement direct-injection (DI) diesel engines have significant potential as the dominant power source for light- and medium-duty road vehicles in the near future [15]. Once considered 'dirty' engines and only viable for large-scale applications, diesel engines now compete with gasoline engines as the prime mover of medium- and small-sized road vehicles.

In the US, the market for sales of vehicles with small and medium engines has grown substantially. In 2011, the light market vehicles sales grew 11 percent, sales of light trucks increased 18.4 percent and sales of small and medium passenger cars increased 4.3 percent from the previous year [11]. New customers appear to prefer smaller engine vehicles which are more fuel efficient and yet reliable in performance; such vehicles typically rely on advanced technology including high pressure charging and advanced control systems.

With the advent of hybrid electric vehicle technology and advanced stationary power systems for local electricity generation, more attention has been given to the production of smaller diesel engines. Engine scaling studies consider the manner in which significant engine parameters are influenced by engine size whereas downsizing refers to an effort to decrease engine size while maintaining the combustion characteristics of the engine. The process of downsizing the combustion chamber involves studies of maximizing specific power output and torque while minimizing fuel consumption and having to deal with the reduced air intake for combustion and the higher surface area-to-volume ratio [16]. The study of scaling of the heat transfer losses complements other aspects of downsizing investigations.

Recent scaling work has been performed using numerical approaches based on 3D computational fluid dynamics (CFD) software. Scaling laws have been developed to characterise the down-scaled engine parameters engines based on those of a higher displacement engine with the goal of maintaining combustion characteristics and engine emissions [17, 18]. In the work of [17], an optimized 450 cc DI-diesel engine was down-scaled to 400 cc, corresponding to a geometric scaling factor of about 0.96 while in the work of [18], a DI-diesel engine was down-scaled from 2336 cc to 292 cc, corresponding to a geometric scaling factor of 0.5, based on the engine bore. Direct geometric scaling was adopted, and the target engine speed of the scaled engine was considered to be the reciprocal of scaling factor. The scaling applied in the computational environment appeared to be successful with minimal differences in the simulated combustion characteristics and emissions.

In-cylinder radiation heat transfer can represent a significant fraction of the total in-cylinder heat transfer – and values between 5 and 40 % are cited – depending on the engine operating conditions [19, 20, 21]. Therefore, the accuracy of the scaling of in-cylinder radiation can have an impact on the success of the overall diesel engine scaling efforts. Scaling studies [17, 18] have typically targeted limited geometric scaling factors relative to optimised engines and have relied on simulation – scaled prototypes have not been developed and hence, inaccuracies in the simulation of radiation scaling are not observed to have a large impact. A significant body of radiation heat transfer data now exists for a wide range of diesel engine sizes ranging from 860 cc to 2330 cc [9, 3, 22, 23, 24] so it is considered timely to consider this data in the context of diesel engine scaling efforts. Radiation measurements have mostly been performed on relatively large engines [23, 24, 22, 3, 8, 7, 21] – typical engine bore sizes are in excess of 100 mm for reported radiation studies in the literature. The role of radiation heat transfer in diesel engine scaling is not clear, so new measurements on small, direct injection diesel engines are required to assist modelling developments in this area. Ra-

diation heat transfer measurement should serve as a powerful diagnostic in the investigation of soot formation and oxidation of any advanced diesel combustion system. To assist diesel engine technology advances in the direction of smaller engine size, reliable information on radiation heat transfer in small diesel engine is needed and this will facilitate the development of more efficient and cleaner diesel engines.

1.3 Research Objectives

Radiation heat transfer represents a significant fraction of in-cylinder heat losses for diesel engines with values ranging from 5 to 40 % [20, 19, 21] depending on the operating conditions. However, most radiation heat transfer experiments have been performed on engines with displacements of more than 860 cc [9, 3, 22, 23, 24, 21]. It is not clear if such results are applicable to small direct injection diesel engines. Therefore, the present work aims to contribute new radiation heat transfer data from a small direct injection diesel engine and to investigate the relationship between radiation heat transfer and engine size. The objectives are:

1. Design and develop reliable instantaneous in-cylinder radiation and convection heat transfer probes for a small DI diesel engine.

2. Obtain experimental results on instantaneous radiative heat flux and convective heat flux from a small DI diesel engine over a range of operating conditions.

3. Assess the new experimental data within the context of previous researcher and investigate the relationship between the radiation heat flux and the engine size.

1.4 Dissertation Overview

The chapters presented in this dissertation are outlined in the following subsections.

1.4.1 Chapter 2, Literature Review

This chapter provides descriptions of the radiation and convective heat flux measurement techniques, probe designs, related issues and the findings drawn from previous researchers. Two radiation heat flux measurement technique were explored. The two-colour method, which has been the more popular choice, is an optical measuring technique which relies on emissions produced by the incandescent soot particles within the flame and uses an emission correlation model and the Planck's law for spectral emissions from a black body. The shielded thermocouple is the other technique and this involves the use of a fast-response thermocouple behind a translucent window so that only the radiation component of the heat transfer is measured. Two important issues in radiation probe measurements are also described: soot deposition and restricted field of view. Soot deposition reduces the magnitude of the radiation measurements. Although many researchers have applied several technique to minimize the effect of soot deposition, a preferred technique to circumvent or compensate for the problem has not emerged and uncertainties still remain. Most researchers have been content to have non-hemispherical radiation heat flux probes. Reliable techniques for deduction of the hemispherical radiation heat flux are yet to be demonstrated. Other researchers have generally focussed on their own experimental arrangements and only modest attempts have been made to unify results by comparing the measured values with literature. No previous works have investigated the influence of the engine displacement with the radiation heat loss.

1.4.2 Chapter 3, Radiation Heat Flux Model

This chapter reports a new radiation heat flux model. The model is implemented with the aid of a thermodynamic simulation of diesel engine combustion in Chapter 7. The objective of the new model and the thermodynamic simulation tool is to progress the understanding of radiation heat transfer in diesel engines and to explore the effect of the engine size changes on the radiation heat transfer. The chapter proceeds with some information on current radiation heat transfer correlations and this is followed by a description of the new model. The new radiation model is based on a correlation for KL values and this approach has been introduced in this work because the empirical Hottel-Broughton emissivity model has proven to be popular and is arguably successful in radiation heat flux measurements via the two-colour method. The KL distribution is modeled as bi-linear in form and its magnitude has been defined based on results from this study and those of other previous works [23, 7]. Given the KL data has been obtained using significantly different engine sizes it is anticipated that the new model will prove useful in the analysis of radiation heat flux results and the correlation of results across different engine scales.

1.4.3 Chapter 4, Apparatus

This chapter presents details of the hardware that was used to characterize the instantaneous radiation heat transfer and the convective component of the instantaneous heat transfer in a small, commercial, direct-injection diesel engine. All of the equipment used, the design and arrangement of the pressure and heat transfer probes, the optical system and other pertinent information relating to the experimental hardware are presented. Introducing in-cylinder pressure and heat transfer probes into a small, commercial, direct-injection diesel engine represents some engineering challenges and these are described. Two different heat flux gauges have been successfully designed, fabricated and tested in the direct injec-

tion diesel engine for measurement of radiative heat flux and related quantities, and for the measurement of convective heat flux. The radiation heat flux probe and associated detectors were configured to obtain data through a variant of the two-colour method. The initial problem of inadequate transmission registered on the photo-detectors was solved through the use of a combination of two glass bifurcated fiber optic bundles. The convective heat flux probe relied on a surface junction thermocouple for measurements of transient surface temperature. The purpose of the convection heat flux probe was to obtain complementary results to those derived from the radiation heat flux probe in order to better understand heat losses to the engine wall of the diesel engine.

1.4.4 Chapter 5, Results and Discussion: Radiation Heat Flux

This chapter presents the results and discussion of the new in-cylinder radiation heat flux measurements obtained in this study. Signal attenuation by probe sooting was successfully compensated by adopting an approach based on post-run calibration of the probe in its sooted state. The engine used in the current work was substantially smaller than other engines from which radiation heat flux data has been reported in the open literature. It is expected that the current results provide valuable information about the effect of combustion chamber size in radiation heat flux scaling. The apparent temperatures deduced from the two-colour method in this study are consistent with the results from other published works [23, 7, 22, 25] in terms of magnitude and the trend of decreasing peak values with increasing load. KL values obtained in this study are lower in comparison to other researchers [23, 7] heat flux with substantially larger engines (2.33 L). The radiation heat flux data obtained in the present work are low in comparison with other works [23, 24, 22, 3, 9]. These results point to the significance of the soot cloud volume in the radiation heat flux losses in constrast to the flame temperature, which appears to be similar for the range of engines for which data

is available.

1.4.5 Chapter 6, Results and Discussion: Convective Heat Flux

This chapter presents the results of the convective heat flux measurements on the engine arrangement as described in Chapter 4. Convective heat flux results have been produced from the measured temperature using an analysis based on an impulse response processing technique. The processing technique is described together with an approach to deduce an effective soot thickness in order to obtain the instantaneous heat flux at the edge of the soot layer, which is the interface with the hot gases. The approach in which the convective heat flux results obtained during compression are tuned to match motoring results obtained with a soot-free probe appears to have been effective. The convective heat flux values from the small engine are in the same range of values identified from other published works [26, 27, 3, 28]. The present work has produced the smallest values for the ratio of radiation heat flux to convective heat flux in comparison with other works [21, 29, 22, 27, 23, 3, 9] in terms of both peak and time-averaged values. It is suggested that this result also reflects the significant influence of engine size on radiation heat flux.

1.4.6 Chapter 7, Results and Discussion: Radiation Heat Transfer Scaling

This chapter provides details of a radiation heat flux scaling analysis performed using data from this study and from other works, through which data for a range of engine sizes, is available. The chapter proceeds with the introduction of some radiation heat loss scaling theory, details on the data sources, a description of the zero-dimensional thermodynamic scaling simulation and some discussion on the

results. The time-averaged radiation heat flux data obtained from different engine sizes, configurations and operating condition of this study and those of other researchers [23, 7, 9, 3, 22] appear to be linearly related to a parameter reflecting the engine size, IP/A_p. This linearity implies the time-averaged radiation heat flux is strongly influenced by volume effects. In contrast, the peak radiation heat flux data appears to scale via a power law relationship with an index of 0.66, indicating that in this case, it is weaker function engine size with surface radiation effects being more significant. As the soot cloud density is at a maximum value during peak radiation heat flux, the flame will appear more opaque at this time, and the surface radiation heat will be more significant. However, during times other than at peak heat flux values, radiation heat flux is more strongly influenced by volume effects.

The quasi zero-dimensional thermodynamic scaling simulations employed using the KL radiation model reported in Chapter 3 complement the experimental data although the differences between the time-averaged and peak heat flux results are not as striking. Values of the powerlaw index m of 0.76 and 0.64 were obtained from least squares fits to the simulation data in the case of time-averaged, and peak results respectively. Although stronger soot cloud surface radiation effects are indicated in the simulation results for the case of the peak values (the value of m is smaller in this case), soot cloud volume radiation effects play an important role in both time-averaged and peak radiation conditions.

1.4.7 Chapter 8, Conclusions

This last chapter reports the conclusions drawn from the investigations of instantaneous radiation and convection heat flux measurements, a modelling, and simulations performed in this study. The chapter proceeds with a summary of all the completed tasks and achievements of this study. The conclusions made from this study are also presented and recommendations for future work are described.

Chapter 2

Literature Review

2.1 Introduction

The earliest diesel engine radiation heat transfer experiments were performed in 1946 by Uyehara et al. [30]. Since that time, many researchers have adopted different approaches and made different contribution in this general area. This chapter contains a literature review of the radiation and convective heat flux measurement techniques, probe designs, related issues and the findings drawn from previous research.

2.2 Radiation Heat Transfer Measurement Methods

Over the past decades, researchers have engaged two main methods for measuring in-cylinder radiation heat transfer inside diesel engines. The methods are: the optical two-colour technique, and the other is the shielded thermocouple technique, in which a surface junction thermocouple is placed behind an optically

transparent window.

2.2.1 Two-Colour Method

The two-colour method is an optical measuring technique designed to determine the apparent flame temperature and an absorption coefficient value that relates to the soot concentration of a field volume inside a luminous flame that is subtended by the field of view of the optical measuring device. From these two values, instantaneous radiation heat flux of the soot inside the flame can be obtained, through the combination of Planck's law for the spectral emissivity of a black body and an equation for the emissivity of soot [2, 31, 32, 30]. There are currently two equations for the soot emissivity equation that could be used in the two-colour method. The most commonly applied is the emperical correlation by Hottel and Broughton [32] while the recently introduced equation proposed by Kamimoto and Murayama [1] provides a more rigorous theoretical basis for the spectral emissivity of the soot.

The two-colour method is based on optical pyrometry, and in general is relatively easy to implement inside combustion engines. The basic general set-up includes a translucent window set in front of a light guide that channels the radiation signal to the photodetectors that are screened with bandpass filters at a minimum of two specified wavelengths. The measurements are primarily sensitive to the emission intensity produced by incandescent soot particles as the major source of radiation heat transfer. Other sources of radiation heat transfer such as from hot gases and intermediate species are not measured and are ignored since their radiation emission are in narrowed spectral bands and are relatively diminutive in magnitude [14].

2.2.1.1 Planck Spectral Radiation Heat Flux

The two-colour method is based on optical pyrometry and it requires optical access to the combustion chamber, which can be challenging, depending on the diesel engine size and design. The method relies on measurements of emissions produced by the incandescent soot particles within the flame. Emissions measurements are typically obtained over relatively broad wavelength bands. The soot particles within the flame are considered as the major source of radiation heat transfer. Other sources of radiation heat transfer such as from hot gases and intermediate species during the combustion process are generally considered to have no impact on the measured radiation since emissions from such species are in narrow spectral bands and are relatively small in magnitude [14].

The two-colour method allows deduction of an apparent flame temperature and an absorption coefficient value that is related to the soot concentration and optical path length within the field of view of the optical measuring device. From these two values, the radiation heat flux from the soot within the field of view of the flame can be obtained through the combination of Planck's law for the spectral emissions from a black body and the Hottel-Broughton equation for the emissivity of soot [2, 31, 32, 30].

The spectral emissive power per unit area of a body (expressed in units of W/m^3, or perhaps W/m^2-nm or W/m^2-μm) can be written using Planck's Law as [2]

$$q_\lambda = \epsilon_\lambda \frac{C_1}{\lambda^5 \left(e^{\frac{C_2}{\lambda T}} - 1 \right)} \tag{2.1}$$

where the value of the emissivity ϵ_λ is also a function of wavelength λ in general, but it adopts a constant value of unity in the case of a 'black body'. The spectral emissive power per unit area of a body changes with wavelength in a unique manner for different temperatures T [2]. The constants in Equation (2.1) have the

values $C_1 = 3.7418\times10^{-16}$ W.m^2 and $C_2 = 14.388\times10^{-3}$ K.m. There are currently two emissivity models: the first by Hottel and Broughton and the second, by Kamimoto and Muruyama.

2.2.1.2 Hottel and Broughton Emissivity Model

Hottel and Broughton [32] have demonstrated that soot does not emit as a black body. They proposed that the emissivity of soot varies with wavelength according to

$$\epsilon_\lambda = 1 - e^{-\frac{KL}{\lambda^\alpha}} \tag{2.2}$$

where KL is the product of a non-dimensional soot concentration parameter K and the optical path length within the flame L, and the index α is a function of wavelength which depends on the flame structure and fuel type. For the visible wavelength region, Hottel and Broughton [32] obtained $\alpha = 1.39$ from direct measurements on steady luminous flames, while Matsui et al. [2] obtained $\alpha = 1.38$ from the spectroscopic analysis of soot layers sampled on a pyrex glass window attached to the cylinder head of a diesel engine. In the infrared region, for wavelengths higher than 0.80 μm, Hottel and Broughton [2] recommended the value $\alpha = 0.95$.

2.2.1.3 Kamimoto and Muruyama Emissivity Model

In 2011, Kamimoto and Murayama [1] introduced a theoretical expression for the emissivity of soot in diesel flames and presented it in a form which resembles the Hottel-Broughton expression. Kamimoto and Murayama demonstrate equivalence with the Hottel-Broughton approach except that the term $(1+\rho_{sa})/\lambda$ is used instead of λ^α. The symbol ρ_{sa} denotes the ratio of specific cross-sections

of scattering to absorption of the soot aggregates in the soot cloud. The effects of out-scattering of the soot cloud are included in the model by Kamimoto and Murayama [1]. The effective soot cloud emissivity model is given by

$$\epsilon_a = 1 - exp\left\{-(1+\rho_{sa})\frac{KL}{\lambda}\right\} \tag{2.3}$$

where the value of ρ_{sa} is obtained by a succession of equations based on soot aggregate scattering theory as presented in [1]. The variation of $1+\rho_{sa}$ in Equation (2.3) with wavelength according to [1] is shown in Figure 2.1.

Although the emissivity model by Kamimoto and Muruyama provides a better physical explanation than the Hottel-Broughton correlation, the difference between the two results in terms of the temperature and KL factor produced, is about $\pm 1\%$ only [1]. Based on this, the present research uses the Hottel-Broughton correlation as the basis for the two-colour method since it has been extensively used in prior work.

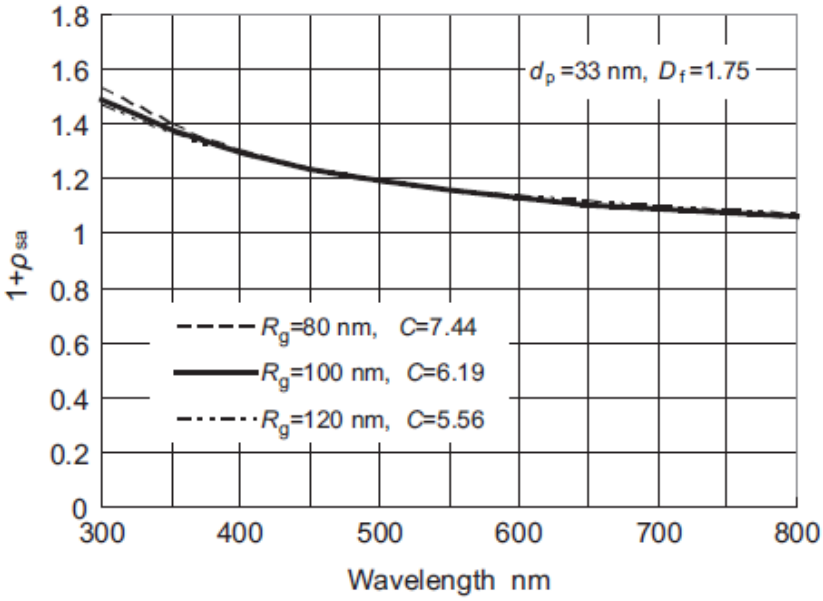

Figure 2.1: The relationship between $1+\rho_{sa}$ and wavelength [1].

2.2.1.4 Two-Colour Method Equations

The spectral emissive power per unit area of the soot cloud can then be described in a single equation as

$$q_\lambda = \left(1 - e^{-\frac{KL}{\lambda^\alpha}}\right) \frac{C_1}{\lambda^5 \left(e^{\frac{C_2}{\lambda T}} - 1\right)} \tag{2.4}$$

With the introduction of bandpass filters into the optical path, the optical detectors will respond to an emissive power which is an integrated effect over the range of sensitive wavelengths. Thus the emissive power per unit area of the soot cloud to which the detectors respond can be written

$$q_{detector} = \int_{\lambda_2}^{\lambda_1} \left(1 - e^{-\frac{K.L}{\lambda^\alpha}}\right) \frac{C_1}{\lambda^5 \left(e^{\frac{C_2}{\lambda T}} - 1\right)} \mathrm{d}\lambda \tag{2.5}$$

where the limits of integration λ_1 and λ_2 correspond to the arranged limits of the optical sensitivity of a particular filter and detector. Provided the optical bandwidth admitted by the filter to the particular detector under consideration is relatively narrow, the radiative flux for the detector can therefore be approximated using

$$q_{detector} = \left(1 - e^{-\frac{K.L}{\lambda^\alpha}}\right) \frac{C_1}{\lambda^5 \left(e^{\frac{C_2}{\lambda T}} - 1\right)} \Delta\lambda \tag{2.6}$$

where $\Delta\lambda = \lambda_2 - \lambda_1$ and $\lambda = (\lambda_2 + \lambda_1)/2$.

In the two-colour method, at least two different centre wavelengths λ (each possibly with a different value of $\Delta\lambda$) are used to provide different values of $q_{detector}$,

corresponding to the emissive power per unit area of the cloud within the wavelength band under consideration. From such a set of measurements, it is possible to deduce values of T and KL via corresponding expressions in the form of Equation (2.6).

Once values of T and KL have been deduced, the total emissive power per unit area of the cloud over all wavelengths can be obtained by integrating Equation (2.4) as

$$q = \int_0^\infty \left(1 - e^{-\frac{K.L}{\lambda^\alpha}}\right) \frac{C_1}{\lambda^5 \left(e^{\frac{C_2}{\lambda T}} - 1\right)} \mathrm{d}\lambda \tag{2.7}$$

Such an expression yields values by numerical integration and practically, the integration can be performed from zero to a sufficiently large number such that results are not significantly affected the finite upper limit of integration. Struwe et al. [24] performed the integration over wavelengths from 0.1 μm to 10 μm.

2.2.1.5 Assumptions of Two-Colour Method

Isothermal and homogeneous soot cloud conditions are assumed within the Hottel and Broughton emissivity approach, Equation (2.2), [2] leading to effective values for soot cloud emissivity and temperature since actual sooty flames will have gradients of both temperature and concentration. Despite such limitations, Struwe [7] emphasizes that the value of the Hottel and Broughton expression, Equation (2.2) is its provision of an essential tool for the practical description of soot radiation. Unless the assumption of an isothermal and homogeneous soot cloud is made, other assumptions concerning the distribution of thermal energy and particle concentrations will need to be combined with an analysis of radiation exchange between particles within the soot cloud and with the external

environment, the accuracy of which cannot be verified with current practical measurement techniques.

2.2.1.6 Selection of Wavelengths for Two-Colour Method

There are several principles for selecting the appropriate wavelengths in implementing the two-colour method, as reported by Ladommatos and Zhao [2] based on findings by Yan and Borman [23], Matsui et al. [25, 33] and Incropera and De Witt [34]. The principles for selecting the optimal wavelengths are: minimizing overlapping gaseous emission, maximizing signal sensitivity, maximizing optical hardware compatibility and avoiding reflections.

2.2.1.6.1 Minimizing Overlapping Gaseous Emission Radiant emissions in a diesel engine arise not only from the soot particles in continuum but also from spectral bands emitted by gaseous species [19, 2, 7]. However, radiation heat transfer measurements in diesel engine have typically been focused on soot radiation emission due to the difficulty of performing a quantitative evaluation of the gaseous emissions [7]. Soot radiation is comprised of a continuous spectrum while gaseous emissions occur within short wavelength ranges [19]. Wavelengths that are prone to substantial overlap with radiation from gaseous species need to be avoided. For example, the OH radical radiates strongly in diesel flames but it only emits significantly in ultra violet region [2]. Volatile radicals such as CH, C_2, HCO, NH, NH_2 also give substantial emission in the near ultra violet wavelengths while water vapour, fuel vapour, carbon dioxide and carbon monoxide emissions can dominate in the infrared region [25, 34].

2.2.1.6.2 Maximizing Signal Sensitivity Greater signal sensitivity is advantageous in maximizing the signal to noise ratio for the computation of the apparent flame temperature in the two-colour method [2]. The rate of change of

the spectral emissive power with respect to temperature is largest in the visible region of 0.4 - 0.7 μm when the temperature is around 1000 to 2000 K for a blackbody as shown in Figure 2.2. Due to this, the normal practice of the two-colour method has been to employ at least one of the wavelengths in the visible region.

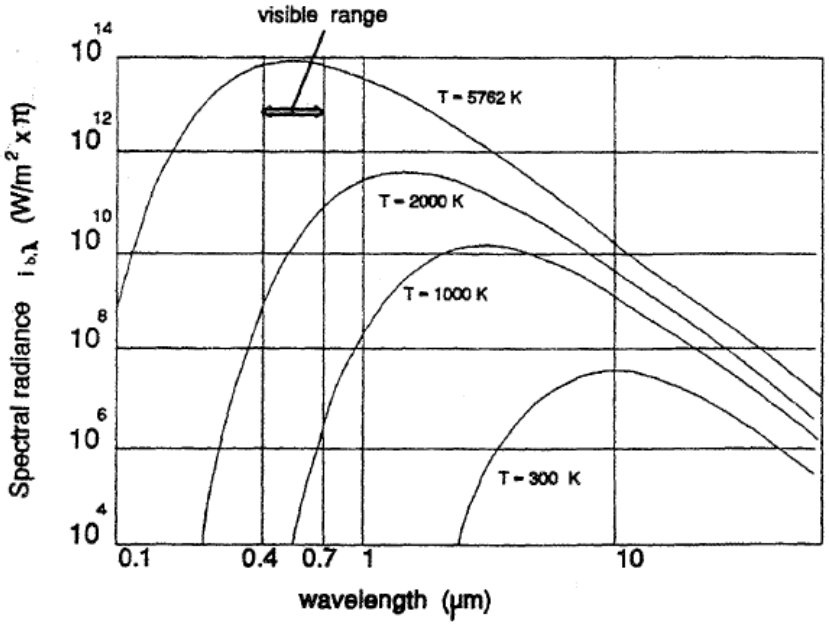

Figure 2.2: Spectral radiance of blackbody at selected temperatures [2]

2.2.1.6.3 Maximizing Optical Hardware Compatibility All related optical components that are involved in guiding and processing the radiation signals from the combustion chamber to the photodetectors have their own transmissivity and responsivity characteristics that vary with wavelength. Hence, care must be taken to ensure the transmittance will be maximized at the different selected wavelengths. Optical fibers can have high transmittance in the near infrared region while silicon photodetectors typically have greater responsivity in the visible. There are wide ranges of transmissivity characteristics for different types of material for the translucent windows and these have to be considered in the instrument design.

2.2.1.6.4 Avoiding Wall Reflections Radiation heat transfer detected by the two-colour probe through its window includes not only the direct radiation from the luminous flame but also from light reflected off the combustion chamber walls. According to Matsui et al. [33] as reported by Ladommatos and Zhao [2], the wavelength region which best avoids reflections from combustion chamber walls is the visibile region, where the effect of wall reflections are minimal compared to the infrared region.

2.2.2 Shielded Thermocouple Technique

The shielded thermocouple technique is a radiation heat flux measurement technique that uses a fast-response thermocouple behind a translucent window which acts as a screen for the convective component of the total heat transfer, so that only the radiation component is measured. The induced voltage produced in the thermocouple circuit arises due to temperature change with crank angle at the hot-junction, and in this case, the temperature change is related solely to the radiation heat flux.

The recorded temperature change is combined with a model for the transient heat conduction process within the gauge substrate in order to deduce the instantaneous heat flux received by the thermocouple. Provided the emissivity of the thermocouple surface is known, the deduced heat flux can be interpreted to give the instantaneous radiation heat flux. The process of deducing the transient heat flux can follow essentially the same methods used in convective heat transfer analysis as discussed in Section 2.5.2.

In Figure 2.3 a radiation heat flux probe of the shielded thermocouple variety as used by Jackson et al. [3] is shown. In this case, sapphire is selected as the translucent window to filter out the convective component of total heat transfer because of its high pass bandwidth [3] - 85 % transmission for wavelengths up to 5 μm. Materials used by other researchers include quartz, irtran II, lucalox and

these have varying transmission characteristics.

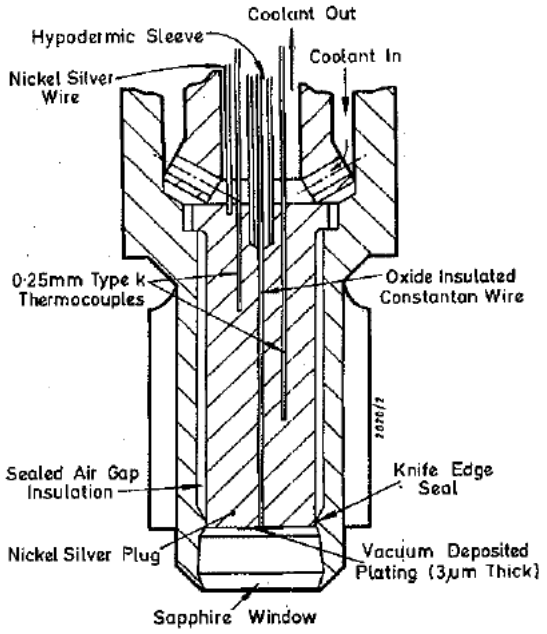

Figure 2.3: Shielded thermocouple radiation heat flux probe by Jackson et al. [3].

2.3 Selected Issues in Radiation Heat Transfer Probe Design

This section reviews two issues relating to radiation heat transfer probe design: soot deposition on the window and the field of view.

2.3.1 Soot Deposition on Window

Soot deposition on the window of the probe is the major contributor of error in radiation heat flux measurements as the soot absorbs and blocks the radiation signals coming into the optical system [24, 23, 2, 31]. There are several methods that have been employed by researchers to minimize this problem.

Ebersole et al. [21] and Qiong et al. [9] applied a purging technique in which a stream of inert gas was used to flush the soot off the window. However, the success of this method has not been quantitatively confirmed. Dent and Suliaman [27], Oguri and Inaba [29] and Jackson et al. [3] employed an injector tripping technique in which motored operation is employed and the wall temperature is brought up to its normal operating temperature by circulating water and oil through external heaters. The injector is then actuated through some rapid actuating mechanism and the first cycles of data are recorded. Other techniques that have been applied include the heating and the probe recession methods and these have resulted in considerable success [33, 35, 22]. Struwe and Foster [24] and Yan and Borman [23] have adapted the probe recession technique further with a cavity structure in front of the recessed window which produced a purging effect upon the window surface during operation. Corrective techniques based on the calibration results have also been used. In the work by [36] the calibration results obtained between pre and post test were averaged to solve the two-colour equations for the apparent temperature and KL value. Although all of these techniques and approaches have been claimed as successful in minimizing the effect of soot deposition by their respective authors, the attenuation of the signal is still evident in the results, especially when the engine runs for longer periods of time. There does not appear to be a single optimal method which can be claimed as the 'right approach'. Significant uncertainties in the existing experimental radiation data remain in all results due to the problem of soot deposition on the probes.

2.3.2 Field of View

Ideally, radiation heat flux probes should have a hemispherial field of view where the directional response follow the cosine law [23]. A perfect radiation heat flux measurement should gather all the radiation incident on the probe surface. However, due to restrictions from the acceptance angle of the window and the blocking

from the probe structure and orientation, the field of view is normally far from hemispherical. A large field of view will also improve the signal to noise ratio which can be useful in the deduction of KL and apparent flame temperature.

However, if the objective of the experiment is primarily the accurate measurement of the KL factor and flame temperature at a specific location, then a small field of view is preferred [31]. A smaller field of view will tend to limit inhomogeneity in temperature and soot concentration and hence a better representation of the actual local values of temperature and KL should be achieved.

Most researchers have been content to have a non-hemispherical radiation heat flux probe and have relied on local instantaneous radiation heat flux data to describe the total radiation heat transfer [23, 9, 22]. This may not be the right value to represent radiation heat transfer as not all radiation heat flux would be measured. Struwe and Foster [24] introduced a technique to extrapolate to the total radiation heat flux based on results from two probes with different fields of view. A relationship for the configuration factors of both probes was used together with a fictional yet mathematically-confirmed soot gradient function. The soot gradient function describes the ratio of the radiation heat flux at the beginning and end of radiation signals. However, this function lacks a physical basis and needs further investigation.

2.4 In-cylinder Instantaneous Radiation Heat Transfer

In this section, important findings and conclusions drawn from previous works are discussed in chronological order. The selection of research works reported herein is based on providing the insights they have provided into research issues that are relevant to the measurement of in-cylinder radiation heat transfer, regardless of measurement technique they used.

The first work relating to in-cylinder radiation heat transfer measurement in diesel engines was by Uyehara et al. [30] in 1946, where a two-colour method was successfully implemented in measuring apparent flame temperature and the KL factor, using electro-optical pyrometer. The engine used was a single-cylinder 4-stroke indirect-injection diesel engine. However, they did not attempt to produce any radiation heat flux data.

In 1963, Ebersole et al. [21] performed the first experiment using a shielded thermocouple technique to measure the radiant in-cylinder heat flux on a two-stroke, direct-injection single-cylinder diesel engine. They discovered that the time-averaged radiant heat transfer amounts to 5-10% of the total heat transfer at low engine load, and 35-45% at near full load. They also postulated that radiant heat transfer in excess of 35-45% of the total heat transfer is expected during the combustion and expansion portion of the engine cycle. Increased radiation heat flux was measured with a sooty window and this was attributed to the increase in surface absorptivity. However, the increase they reported remains unverified as most succeeding works present a significant decrease in radiation signals with sooty window surfaces.

Flynn et al. [22] determined instantaneous radiation heat flux in a direct-injection single-cylinder diesel engine using a variant of the two-colour method that involves measurement of monochromatic radiation emission intensity at seven wavelengths in the infrared, ranging from 1-4 μm. The experimental set-up includes the use of selenide photodector and infrared monochromator devices behind a removable quartz window. This removable window allows changing of the window during engine operation to circumvent the problem of window sooting. A transmittance lower than 70% was used as the threshold at which the window should be changed. They investigated the effect of changing the engine operating parameters (engine speed, fuel air ratio, manifold pressure, injection timing, nozzle hole pattern rotation) on the instantaneous radiation heat flux. Comparison to known total heat flux data was made and time average values of radiation heat flux were

found to account for 20% of the time average values of total heat flux. However, this percentage appears somewhat speculative due to the different locations of the radiation window and the thermocouple. An attempt was made to obtain an instantaneous radiation heat flux correlation based on the experimental data, but the empirical function produced was based on a curve-fitting exercise with no special physical basis.

In 1988, Yan et al. [23] performed two-colour method experiments on a direct-injection diesel engine, measuring the radiation emissions at three wavelengths. Yan used the extra wavelength to compute the wavelength constant in the Hottel-Broughton emissivity equation as shown in Equation (2.2). In the experiment, the effect of changing engine parameters (engine speed, equivalence ratio, intake temperature and pressure, coolant temperature, injection timing, orientation of injection plumes) and the field of view of probe was investigated. Yan was using a self-cleaning probe which had a cavity in front of the window to produce a suction effect on the window surface. The field of view of the main probe used was 14° although probes with a 27° and hemispherical field of view were used for comparison at one engine operating condition. The hemispherical field of view was obtained using a lucalox window while the other field of view was obtained by adjusting the aperture in the probe. The onset of the radiation signals were the same for each field of view, but the smaller field of view showed a higher rate of signal decay at later crank angles. Time-averaged radiation heat flux was compared with time-averaged total heat flux of McDonald [37] and the ratio amounted to 11% which is lower than that reported by Flynn [22] and [21].

A study in 1998 by Qiong et al. [9] measured both instantaneous radiation heat flux and total heat flux using commercially available probes with the radiation probe having a gas purge jet to eliminate soot deposition. However, no qualitative data was given on the effectiveness of the jet and no information was given on the field of view of the radiation heat flux probe. The results are generally in accord with previous works and the ratio of radiation heat flux to total heat flux ranged

between 11% to 17% and depending on the engine load and speed.

Struwe et al. [24] in 2003, measured hemispherical instantaneous radiation heat flux from a direct-injection diesel engine using the same probe as Yan [23] with lucalox window and an enhanced soot-cleaning cavity, which was achieved by selecting the optimum gap size. The hemispherical instantaneous radiation heat flux was deduced by obtaining a relationship between two configuration factors for the two probe's fields of view and extrapolating it to the hemispherical field of view together with an arbitrary soot gradient function. However, Struwe admitted that no physical principle was applied in producing the soot gradient function. Time-averaged radiation heat flux showed an increasing trend with the fuel flow rate, indicated mean effective pressure and the equivalence ratio. Struwe [24] postulated briefly that the radiation heat flux could be engine size-related but did not substantiate the claim.

2.5 Convective Heat Flux Measurement

The total in-cylinder heat transfer for internal combustion engines is comprised of convective and radiation components. For the analysis of instantaneous radiation heat flux measurements, having additional instantaneous convective heat flux data with a similar probe orientation and using the same engine set-up, would add valuable information regarding the significance of radiation heat losses relative to the overall engine heat transfer. In this section, techniques associated with instantaneous convective heat flux measurements in IC engines will be briefly reviewed.

2.5.1 Instantaneous surface heat flux measurements

For accurate instantaneous flux measurements, the temperature sensor needs to be a very fast response device and it needs to be located at the surface of the probe. Ideally, the thermal properties of the probe and combustion chamber wall need to be almost the same to maintain an undisturbed wall temperature field.

Eichelberg, as reported in [20] was the first to obtain instantaneous surface temperature measurements of an engine combustion chamber in 1939 using a rugged thermocouple, with the hot junction created by edge contact between the thermocouple pair. More recently, researchers have used surface thermocouples created with thin metallic layers vacuum-deposited or chemically plated on a substrate. The thickness of the deposited layers have been in the range of 1 μm to 10 μm. This range of thickness was considered to give the optimum compromise between response time and robustness. The type of the surface thermocouple can be categorized according to its structure: the coaxial type, the pair wire type and the film type.

2.5.1.1 Coaxial Thermocouple

Bendersky [20, 29] was the first to demonstrate the use of a coaxial type of thermocouple in taking measurements of the surface temperature of a gunbore and his design has become a primary reference for researchers using coaxial thermocouples. LeFeuvre et al. [4] used the structure of a coaxial thermocouple as shown in Figure 2.4. Overbye [38] and Ebersole [21] used a plated junction design for their coaxial thermocouple. The first thermocouple element used was an iron tube and the second element was the nickel or constantan wire in the centre, which was insulated from the first thermocouple element. The junction was produced via vacuum-deposition process which forms a thin layer of metal of around 1 μm thick at the end of the thermocouple probe. A second hot junction was made by connecting another wire of the second thermocouple element to the iron tube

surface that is exposed to the coolant side. The second junction is necessary for the calculation of the steady state component of the heat flux.

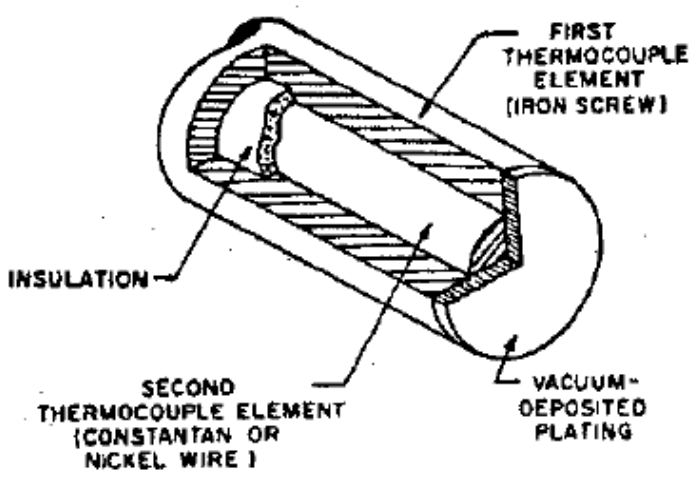

Figure 2.4: Coaxial thermocouple. Figure taken from [4].

2.5.1.2 The Pair Wire Type Thermocouple

The general construction of pair wire type thermocouples includes two insulated wires of thermocouple elements with ends that are connected by thin metallic plating. The other ends of the wires are connected to the amplifier circuit. Most variants of the insulated wire design involve running the wires inside a slot or a groove affixed through swaging inside the probe body. Hara and Oguri [39] used iron and constantan wires which were swaged into a groove on a joint-section of a cone-shaped probe body that can be separated into two. The hot junction consisting of a thin metal film was formed by a vacuum deposition process.

2.5.1.3 The Film Type Thermocouple

Film type thermocouples were used in the experiments performed by Annand [26]. Thermocouple elements used were antimony and the iron of the engine head which was connected to the amplifier circuit by iron wire. The laying down of the

thermocouple circuit was achieved by the vacuum deposition of three consecutive films of total thickness less than 0.005 mm.

2.5.2 Calculation of Heat Flux from Surface Temperature Data

To determine the heat flux between the cylinder gases and the wall, the unsteady heat conduction equation must be solved. Surface temperature measurements obtained from the surface thermocouple are used as a boundary condition in solving the unsteady heat conduction equation. The normal assumption is that the heat flow in the probe body is one-dimensional and the measurement of the hot junction temperature is the surface temperature. As the unsteady portion of the in-wall temperature field occurs over a small length near the surface, the magnitude of the temperature gradient perpendicular to the wall surface is much higher than the temperature gradient parallel to the wall. Due to this phenomena, the assumption of one-dimensional heat transfer is valid [20, 40].

The one-dimensional unsteady heat conduction can be written as

$$\frac{\partial T}{\partial t} = \frac{1}{\rho c}\frac{\partial}{\partial x}\left(k\frac{\partial T}{\partial x}\right) \tag{2.8}$$

where T is the temperature, t is time, ρ is the density, c is the specific heat, k is the thermal conductivity and x is the distance from the wall surface. Three methods are available to solve the unsteady heat conduction equation. Fourier analysis, electrical circuit analogy and time domain numerical methods.

2.5.2.1 Fourier Analysis

Most calculations of transient heat flux from temperature measurements in engines have been based on the assumption of steady periodic temperature variations existing in the solid medium, allowing the application of a Fourier series solution method. Using a Fourier series, a steady periodic temperature of wall temperature, T_w can be defined as

$$T_w = T_m + \sum_{n=1}^{N} [A_n \cos(n\omega t) + B_n \sin(n\omega t)] \tag{2.9}$$

where T_m is time-averaged value of the wall temperature for the whole engine cycle, ω is the angular velocity in rad/sec, A_n and B_n are the Fourier coefficients and n is the harmonic number.

The necessary boundary conditions for the solution of Equation (2.9) are

1. Temperature reading of the thermocouple at the wall surface, $x = 0$:

$$T(0, t) = T_w(t) \tag{2.10}$$

2. Temperature reading of another thermocouple positioned at distance $x = \delta$ from the surface:

$$T(\delta, t) = T_\delta \tag{2.11}$$

The solution to Equation (2.9) can then be expressed as:

$$T(x,t) = T_m - (T_m - T_\delta)\frac{x}{\delta} + \sum_{n=1}^{N} exp(-\phi_n \cdot x)F_n(x,t) \tag{2.12}$$

where

$$F_n(x,t) = A_n \cos(n\omega t - \phi_n x) + B_n \sin(n\omega t - \phi_n x) \tag{2.13}$$

and

$$\phi_n = (n\omega\rho c/2k)^{1/2} \tag{2.14}$$

The instantaneous surface heat flux can be determined from Fourier's Law by differentiating Equation (2.12) with respect to x and multiplying by the conductivity:

$$q_w(t) = \frac{k}{\delta}(T_m - T_\delta) + k\sum_{n=1}^{N} \phi_n[(A_n + B_n)cos(n\omega t) + (B_n - A_n)sin(n\omega t)] \tag{2.15}$$

2.5.3 Electrical Circuit Analogy

The characteristics of one-dimensional heat conduction in a solid can be treated as similar to a current flow in shielded electrical conductor, without any self-inductance. Discrete element approximation for the resistance-capacitance circuit

was applied in this method. Values of resistance and capacitance need to be selected carefully. As with the Fourier method, the disadvantage of this method is that the conductivity has to be assumed constant.

2.5.4 Time Domain Numerical Method

Due to the non-linearity of the unsteady heat conduction problem for the case where material properties change with temperature (Equation (2.9)), a numerical solution method may yield more accurate results. Thermal properties can vary significantly when there are large temperature swings at the wall surface. This may occur for example, if there is a ceramic coated wall surface inside the combustion chamber of a low-heat-rejection (LHR) engine or when soot layers are deposited on the wall. In such cases, numerical solutions such as finite difference or finite element methods can be used to analyse the temperature measurements in the time domain to yield a time-resolved variation of the surface heat flux.

2.6 Conclusion

Diesel engine radiation heat transfer measurement techniques based on the two-colour method and the shielded thermocouple probe were reviewed. Convective heat transfer measurement techniques were also reviewed. A general issue relating to heat flux measurement techniques include the problem of sooting which greatly reduce the magnitude of heat flux readings and introduces lagging in the signal. Approaches taken by previous researchers include gas flushing, injector tripping, recessing the window and cavity, and averaging calibration values between pre- and post-tests. However, all these techniques either lack reliability especially for engines with high loads and longer running times or lack substantive data on the effectiveness of the technique. With different engine configurations and operating conditions, it is difficult to make comparisons and draw reliable conclusions on pa-

rameters affecting radiation heat flux results. The relationship between radiation heat flux and the engine displacement is yet to be explored and is only mentioned briefly by Struwe [24]. Further investigation of radiation heat flux scaling should provide useful data for future modelling efforts and engine downsizing work.

Chapter 3

Radiation Heat Flux Model

3.1 Introduction

This chapter reports a new radiation heat flux model. The objective of the new model is to progress the understanding of radiation heat transfer in diesel engines and to explore the effect of the engine size changes on the radiation heat transfer. The chapter proceeds with some information on current radiation heat transfer correlations and is followed by a description of the new model in the second part of the chapter. The model is implemented with the aid of a thermodynamic simulation of diesel engine combustion in Chapter 7.

3.2 Radiation Heat Transfer Correlation

There are three radiation heat transfer correlations that can be conveniently implemented in the quasi zero-dimensional thermodynamic models. These are correlations by Annand [41], Sitkei and Ramanaiah [5] and Morel and Keribar [14].

3.2.1 Annand Model

The initial attempt to model radiation heat transfer was performed by Annand et al. [41] and in this case, radiation heat flux was represented using Stefan Boltzmann's Law. With this model, at any instant the heat transfer rate is treated as proportional to the fourth power temperature difference between the working fluid and the combustion chamber wall. In common with other models, a uniform distribution of the instantaneous gas temperature in the cylinder is assumed [42]. The model is written as

$$q = C\sigma \left(T_g^4 - T_w^4\right) \tag{3.1}$$

where C is a constant that describes the emissivity of both the gases and the wall. C is taken as equal to zero during the compression stroke and is equal to a constant value of 0.57 for the combustion and expansion stages. T_g is the average temperature of the gases while T_w is the temperature of the wall and σ is the Stefan-Boltzmann constant with the value of $5.6704 \times 10^{-8}\,\mathrm{W \cdot m^{-2} \cdot K^{-4}}$.

3.2.2 Sitkei and Ramanaiah Correlation

Sitkei and Ramanaiah [5] improved the emissivity constant defined in the Annand correlation with the addition of a radiation absorption factor, k in the correlation. The equations that define the Sitkei and Ramanaiah [5] radiation heat flux correlation are as follows.

Measured emissivity

$$\epsilon_i = \frac{T_b^4}{T_f^4} \tag{3.2}$$

Emissivity:

$$\epsilon = \epsilon_i(1 - e^{-kpl}) \tag{3.3}$$

Optical mean path length:

$$l = 3.6\,\frac{V}{A} \tag{3.4}$$

Radiation heat flux:

$$q = \epsilon\sigma(T_g^4 - T_w^4) \tag{3.5}$$

where ϵ_i is the measured emissivity, T_b is the blackbody temperature, T_f is the flame temperature, p is the pressure inside the combustion chamber in units of atmosphere, V is the volume of the combustion chamber, A is the surface area of the combustion chamber.

The radiation absorption factor, k is a value that was obtained from extrapolating the findings of emissivity data measured in engine tests for various operating condition including engine load, pressure and excess air factor [5]. The specific method used to obtain these absorption factor values was not provided in detail by Sitkei and Ramanaiah [5]. The radiation absorption factor, k changes with engine speed and soot particle density, which in turn is influenced by the quality of the mixture, the type of injector and the combustion chamber arrangement. Figure 3.1 shows the radiation absorption factor, k which Sitkei and Ramanaiah [5] claimed is universally applicable to any engine while noting that other parameters such as engine speed and soot particle density varies with different engine conditions and arrangements.

With a knowledge of the $p - V$ diagram of an engine, one can readily obtain instantaneous radiation heat flux through the use of Figure 3.1.

3.2.3 Morel & Keribar Model

Morel and Keribar [14] proposed a radiation heat flux model that describes the instantaneous radiation heat flux as a function of the instantaneous thermophys-

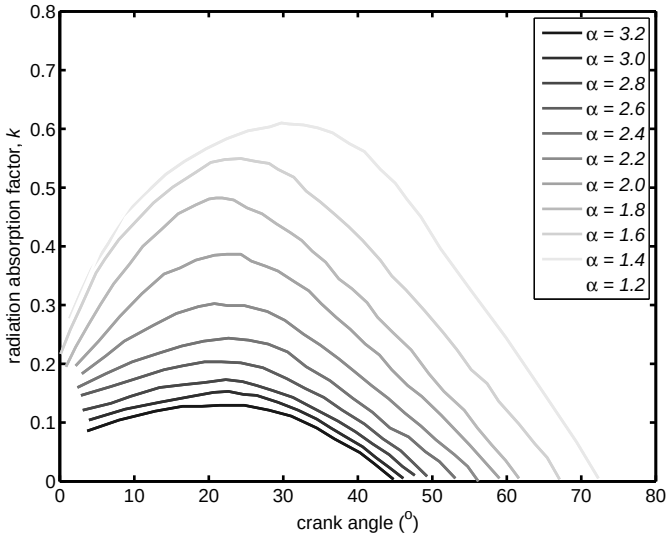

Figure 3.1: Radiation absorption factor, k at different excess air factor, α as used for the Sitkei and Ramanaiah correlation [5].

ical properties of radiation zone: its size, radiation temperature and radiation absorptivity constant of the soot cloud. Simple chemical kinetic equations were used to represent the soot formation and oxidation processes, which in turn determines the soot concentration level. Morel and Keribar implemented the model in IRIS, an IC engine simulation code and achieve considerable accuracy in terms of magnitude and phasing of simulated heat flux.

The Morel and Keribar model can be used to simulate the important phenomena and processes involves in radiation heat transfer inside diesel engines. The proposed kinetic expressions for soot formation and oxidation which determine the soot concentration were validated with reference to literature data. A correlation that relates soot concentration and average emissivity of the burned zone is applied as shown below [43].

$$\epsilon_s = 1 - e^{-al} \tag{3.6}$$

where a is the absorption coefficient and l is the optical mean beam length which

is calculated from the volume of burned zone. Inside the burned zone, soot concentration is assumed to be uniformly dispersed. The absorption coefficient is a parameter that represents the ability for a medium to reduce the intensity of radiation energy which passes through it. The absorption coefficient can be defined based on Mie theory and after some simplifications and substitutions, it can be expressed as [14]:

$$a = 1575 f_v T \tag{3.7}$$

$$f_v = \frac{m_s}{\rho_s V_b} \tag{3.8}$$

where f_v is the volume fraction of soot in the burned zone and T is temperature of the burned zone. The volume fraction, f_v can be identified from the soot concentration, which can be deduced from the soot formation and oxidation model as shown below.

Soot formation:

$$\frac{dm_{s,f}}{dt} = A_1 \dot{m}_d \frac{exp\left(\frac{-A_2}{T_f}\right)}{(1 + 4.76 Y_{O_2})^3} \tag{3.9}$$

Soot oxidation:

$$\frac{dm_{s,o}}{dt} = -\frac{B_1 m_s}{\rho_s d_s} e^{-\frac{B_2}{T_f}} P_{O_2}^{\frac{1}{2}} \tag{3.10}$$

Soot concentration:

$$\frac{dm_s}{dt} = \frac{dm_{s,f}}{dt} - \frac{dm_{s,o}}{dt} \tag{3.11}$$

where $\dot{m}_d$ is the rate of fuel burned, A_1, A_2, B_1 and B_2 are constants with values of 0.38, 5000, 0.015 and 5000 respectively, Y_{O_2} is the mole fraction of available oxygen in the burning zone, r_s is the density of soot particles which is taken as $900\,\mathrm{kg/m^3}$, d_s is the diameter of soot particles taken to be $0.002\,\mathrm{mm}$, T_f is

the adiabatic flame temperature and P_{O_2} is the partial pressure of oxygen in the burned zone.

Qiong et al. [9] demonstrated the use of Morel radiation model in zero-dimensional thermodynamic simulations. Simplifications were made whereby the wall was assumed as gray and wall emission and gas absorption and scattering were neglected. The radiation heat flux of the Morel and Keribar model was therefore simplified to be:

$$q_r = \sigma F_{ij} \epsilon_w \epsilon_s \left(T_r^4 - T_w^4\right) \tag{3.12}$$

where F_{ij} is the view factor of the radiation probe device, ϵ_w is the emissivity of wall, ϵ_s is the emissivity of the soot cloud, as expressed in Equation (3.6), T_r is the radiating temperature of the soot cloud and T_w is the temperature of the combustion chamber wall.

3.3 *KL* Radiation Model

A new radiation heat flux model was formulated using correlations based on experimental data generated in this study and other published experimental works. This section proceeds with a description of the derivation of the correlation from experimental data (KL values data) followed by an explanation of the new radiation heat flux model. Descriptions of KL from previous works indicate that two important parameters influencing KL are the soot concentration and the optical path length. On this basis, a new correlation of KL was made, with the parameters being the equivalence ratio and the indicated power per unit area, together with the use of crank-resolved KL data from this study and from published works [23, 8, 24, 7]. The new radiation heat flux model was formed using this correlation of KL.

3.3.1 Correlation of *KL* Values

The quantity KL is commonly used in sooting flame radiation analysis, following the approach of Hottel and Broughton [32]. The KL value relates directly to the opacity of the soot cloud, where a higher KL value signifies lower transmissivity of the soot cloud. Based on radiation heat flux measurements using the two-colour method in diesel engines [22, 23, 24], the phasing of the maximum radiation heat flux is observed near the maximum KL value, due to relatively constant apparent flame temperatures measured during the combustion process. This means that peak radiation heat flux occurs at a condition where the flame (soot cloud) is at its most opaque, and hence, surface radiation effects are expected to be significant.

The KL value has been shown to be related to the soot concentration by the use of Kirchoff's Law, through which the emissivity of the soot cloud is considered equal to its absorptivity, giving the expression [2]:

$$c_m = \frac{\rho_s \pi d^3 KL}{6\lambda^\alpha C_{ext} L} \tag{3.13}$$

where c_m is soot mass concentration, ρ_s is the density of primary soot particles, d the diameter of soot particles, λ is the wavelength, α is the wavelength constant, C_{ext} is the extinction cross-section and L is the beam length.

Kamimoto and Murayama [1] define KL as:

$$KL = \frac{6\pi E(m) c_m L}{\rho_s} \tag{3.14}$$

where $E(m)$ is a function of the complex refractive index of soot particles, c_m is the soot mass concentration, and L is the soot cloud thickness in the direction of the optical path, and ρ_s is the density of primary soot particles. In this case,

the effect of scattering of the radiation through the soot cloud is included in the physical definition of the KL value. The quantity K is observed to be a nondimensional quantity, and hence KL has the units of length, and normally micrometers are used, although units are not normally attributed to KL in the literature.

Data from authors reporting crank-resolved KL values in conjunction with equivalence ratio and indicated power and/or pressure data were analysed and results are presented in Table 3.1.Values of KL_{max}, which occurs close to the time of the maximum radiation heat flux value, and KL_{ave} which represents the mean KL value when averaged over the entire four stroke diesel cycle are reported in Table 3.1. Note that although Flynn [22] reports the necessary data, the results do not appear in the compilation of Table 3.1 because the probe viewing configuration which was used differs markedly from that adopted by the other workers. In Flynn's work [22], the probe was positioned on the cylinder and a slot was cut into the piston to enable viewing into the piston bowl. This resulted in a very long optical path length relative to that adopted for the other direct injection diesel engines in which probes were positioned on the engine head. The resulting KL data [22] were much higher than reported by other workers, likely reflecting the significantly larger optical path length.

Data from Table 3.1 are plotted in Figure 3.2 and 3.3. Linear correlations of experimental values of KL_{ave} and KL_{max} with the equivalence ratio, ϕ and the indicated power per piston area, IP/A_p which have been constrained to pass through the origin have been deduced and are given by

$$KL_{max} = 1.88 \times 10^{-3}\, \phi\, \frac{\mathrm{IP}}{A_p} \tag{3.15}$$

Table 3.1: Values of KL_{ave} and KL_{max} from different diesel engines and operating conditions.

IP/A_p (kW/m^2)	ϕ	KL_{ave} ($\times 10^{-3} \mu m$)	KL_{max} (μm)	Source
260	0.303	4.4	0.623	
378	0.325	3.7	0.277	USQ
398	0.493	32.0	1.653	
545	0.552	15.7	0.667	
1656	0.287	51.1	2.020	
1950	0.394	54.4	1.726	
2498	0.493	58.2	1.635	
2001	0.307	47.5	1.333	Yan [23, 8]
2577	0.398	60.2	1.356	
2955	0.463	28.9	1.446	
1268	0.482	29.9	1.828	
1265	0.482	28.0	1.851	
1839	0.585	64.6	2.776	
1843	0.585	61.3	2.858	
2401	0.635	88.0	2.542	
2414	0.635	86.8	2.600	Struwe [24, 7]
1380	0.413	17.0	1.180	
1400	0.413	18.1	1.221	
2049	0.526	71.7	2.451	
2076	0.526	61.9	2.608	
2541	0.536	86.0	2.862	
2566	0.536	80.2	2.897	

$$KL_{ave} = 5.21 \times 10^{-5}\, \phi\, \frac{\mathrm{IP}}{A_p} \tag{3.16}$$

where IP/A_p is expressed in kW/m^2, ϕ is the equivalence ratio (nondimensional), and KL is expressed in μm. These correlations are shown as the broken lines in Figure 3.2 and 3.3. The coefficient of determination for KL_{ave} being $R^2 = 0.64$, and for KL_{max}, $R^2 = 0.16$, indicating the linear model is substantially better in the case of the KL_{ave} results. The correlation of the nondimensional soot concentration parameter K with equivalence ratio ϕ is expected since higher soot concentrations will occur at higher equivalence ratios. The parameter IP/A_p reflects the engine scale as discussed in later part of this thesis, Section 7.4. Therefore it is also reasonable that the optical path length within the flame, L should correlate with IP/A_p for flame conditions with high transmissivity. When opaque flame conditions prevail, which is the case for peak KL conditions, the apparent optical length within the flame is expected to become independent of actual flame or engine size, and this may provide an explanation for the linear model being relatively poor in the case of the KL_{max} data.

3.3.2 *KL* Radiation Model

A new radiation model was developed following the correlation of the experimental data on KL values from two-colour experiments of this study and by other researchers [24, 23]. If a universal *shape* for the crank-resolved KL variation is assumed, then the values of KL_{max} and KL_{ave} from the correlations of Section 3.3.1 will be sufficient to define the profile for different engine operating conditions. Based on the available KL data from literature [23, 8, 24, 7] and of from the experimental results of this study, a universal KL profile was deduced. All the

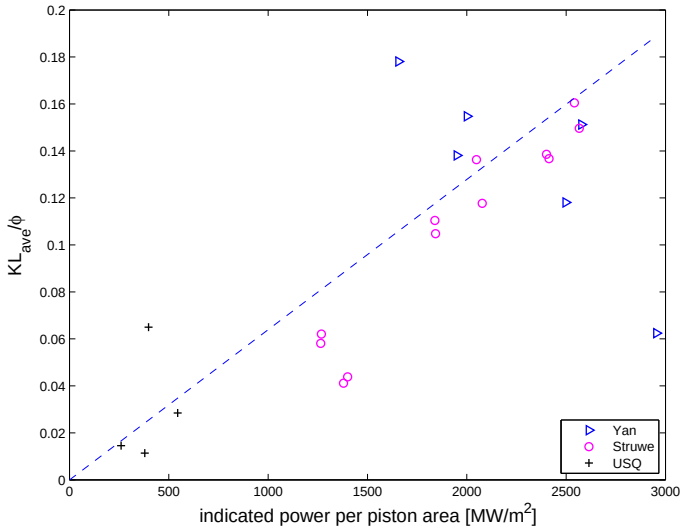

Figure 3.2: Correlation of average KL normalised by equivalence ratio KL_{ave}/ϕ with indicated power per unit piston area IP/A_p. In this case, $R^2 = 0.64$.

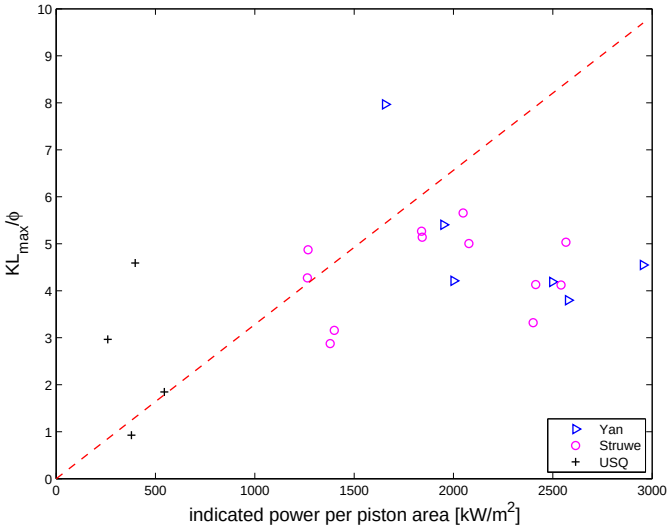

Figure 3.3: Correlation of maximum KL normalised by equivalence ratio KL_{max}/ϕ with indicated power per unit piston area IP/A_p. In this case, $R^2 = 0.16$.

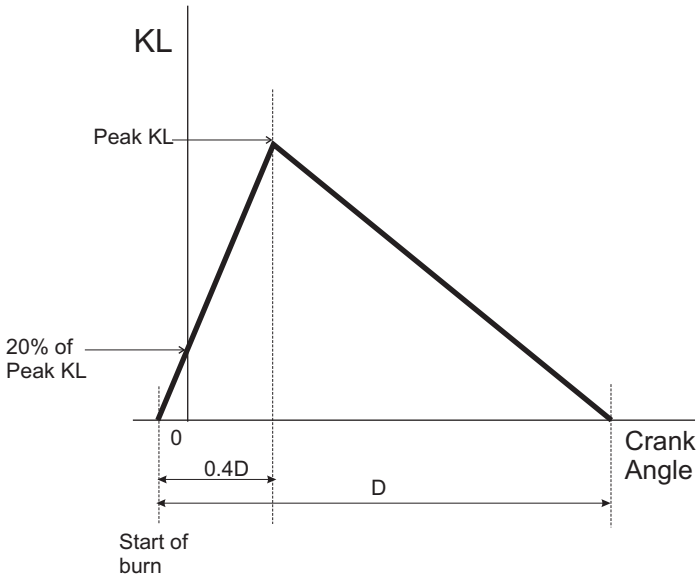

Figure 3.4: Illustration of the assumed crank-resolved *KL* shape distribution adopted in the present work.

KL profiles exhibit the same distinct features: 1) a rapid rise after the start of combustion and 2) a more gradual decrease after reaching the peak. Based on these two features, a bi-linear shape has been assumed as a universal *KL* profile shown in Figure 3.4. More complicated profiles are obviously possible, but the simple bi-linear approach appears satisfactory for the present work. For this distribution, *KL* rises more rapidly than it falls, reflecting the skewed distributions observed in the experimental data [7, 23]. The overall crank angle duration D expressed in degrees for non-zero *KL* values in the presently assumed *KL* shape model is given by

$$D = 2\,\frac{KL_{ave}}{KL_{max}} \times 720^{\circ} \tag{3.17}$$

The radiation model used in the present work calculates the radiation heat flux q_r from the flame (treating it as an incandescent soot cloud) via the Hottel-

Broughton equation of flame emissivity [32] and the spectral distribution of emissive power [30] according to,

$$q_r = \int_0^\infty \left(1 - e^{-\frac{KL}{\lambda^\alpha}}\right) \frac{C_1}{\lambda^5 \left(e^{\frac{C_2}{\lambda T}} - 1\right)} \mathrm{d}\lambda \tag{3.18}$$

where λ is the wavelength expressed in μm, $\alpha = 1.38$, $C_1 = 3.7413 \times 10^8\ \mathrm{W}\mu\mathrm{m}^4/\mathrm{m}^2$, and $C_2 = 1.4388 \times 10^4\ \mu\mathrm{mK}$. The integration was performed numerically with the limits of integration being $0.1\,\mu$m and $10\,\mu$m for computational economy. Results from this model, when implemented in a quasi-dimensional thermodynamic simulation are reported in Chapter 7, where comparisons are made with experimental data produced in the current work, and data produced in other studies.

3.4 Conclusion

Models by Sitkei and Ramanaiah [5] and Morel and Keribar [14] include the influence of the mean beam length and the soot concentration. In the case of Sitkei and Ramanaiah [5], the radiation absorption factor, k is empirically defined and appears engine specific. In the case of Morel and Keribar [14], a theoretical soot formation and soot oxidation model is used to define the soot concentration. A new radiation model based on correlations for KL values has been introduced in this work because the empirical Hottel-Broughton emissivity model has proven a success in radiation heat flux measurements via the two-colour method. The KL distribution is modeled as bi-linear in form and its magnitude has been defined based on results from this study and those of other previous works [23, 7]. Given the KL data has been obtained using significantly different engine sizes it is anticipated that the new model will prove useful in the analysis of radiation heat flux results and correlation of results across different scales.

Chapter 4

Apparatus

4.1 Introduction

This chapter presents details of the hardware that was used to characterize the instantaneous radiation heat transfer and the convective component of heat transfer in a small, commercial, direct-injection diesel engine. All of the equipment used, the design and arrangement of the pressure and heat transfer probes, the optical system and other pertinent information relating to the experimental hardware will be presented. Introducing in-cylinder pressure and heat transfer probes into a small, commercial, direct-injection diesel engine represents some engineering challenges and these will be described.

4.2 Test Engine

The engine used in the program of experiments was a Yanmar L48AE – a small direct-injection diesel engine of 211 cc displacement. Key engine specifications are presented in Table 4.1. The engine can be classed as producing high swirl conditions [19, 44] and the piston bowl is of a shallow toroidal shape which has an

under-cut profile at its edge and an elevated profile in the centre as illustrated in Figure 4.1. The fuel injector used was a 4-hole nozzle device actuated by a cam and push-rod mechanism. The fuel spray from the injector nozzles was directed as illustrated in Figure 4.1.

As the probe axis lies between the axis of two nozzle sprays and with the high swirl ratio condition, there is a strong possibility that the variation in intensity with crank angle is due to the effect of the passage of spray passing the limited field of view of the probe, more than the temporal progress of the combustion process. The fuel used in this work was a low-sulphur diesel fuel with properties shown in Table 4.2.

The in-house modifications that were performed on the cylinder head involved machining an angled 9.5 mm diameter hole for the placement of radiation probe and a vertical hole for the pressure probe as illustrated Figure 4.1. The machining for the pressure probe involve two stages: a 10.5 mm diameter hole through the outer material of the cylinder head and then a locating and sealing shoulder on the inner material of the cylinder head.

Table 4.1: Yanmar L48AE Engine Parameters.

Parameter	Values and Information
Bore	70 mm
Stroke	55 mm
Compression Ratio	19.9
Displacement	0.211 L
Fuel injector	4 nozzle holes
Injector orifice diameter	0.22 mm
Injection angle	150°
Injection timing	13-15° BTDC

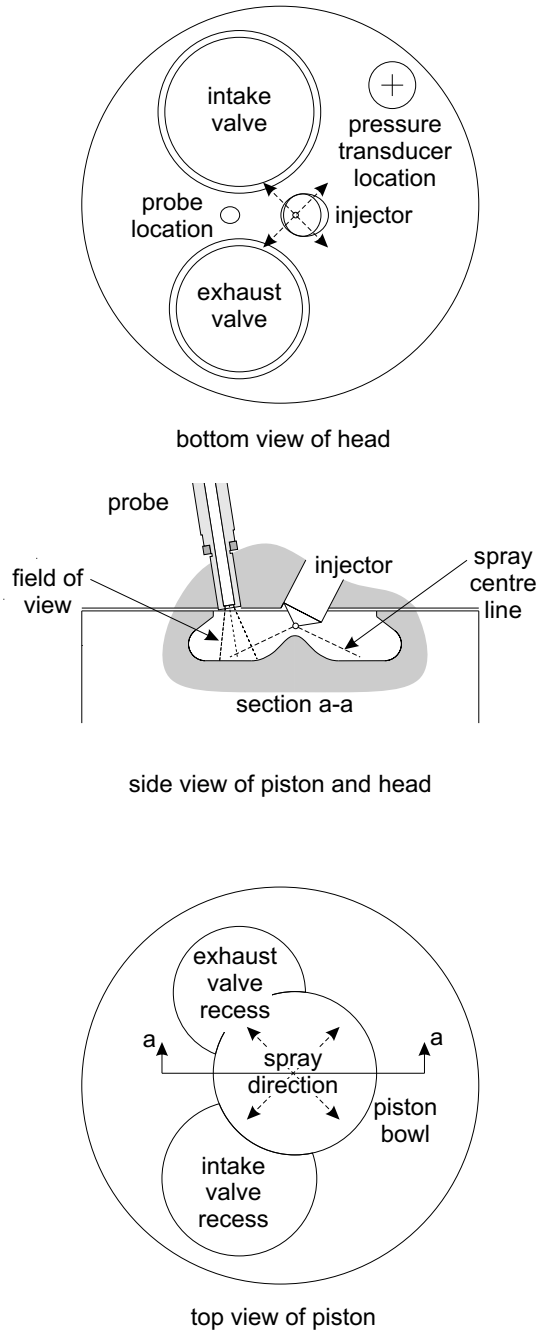

Figure 4.1: Sketch of the Yanmar piston and head arrangement used in the experiments showing the location of the valves, injector, and measurement devices.

Table 4.2: Diesel fuel properties (Donghwa-Saybolt Korea Co. Ltd.).

Parameter	Values and Information
Sulphur Content	Less than 10 ppm
Cetane Index	Min. 46
Density (at 15 °)	820-850 kg/m^3
Oxidation Stability	Max 20 mg/l
Flash Point	64 °C

4.3 Dynamometer and Associated Instrumentation

Details of the dynamometer and associated instrumentation are presented in Table 4.3. The Yanmar engine was connected to a hydraulic dynamometer for testing under loaded conditions as illustrated in Figure 4.2. The arrangement used an electric motor for starting the diesel engine and for experiments under motored conditions. An hydraulic oil pump and an associated pressurization and relief circuit was used to develop a load on the diesel engine. Under normal operation the diesel engine was started with the hydraulic oil control valve open, and the load and speed of the engine was then set by manual adjustment of both the control valve on the hydraulic oil circuit and the fuel flow rate to the engine. During the establishment of the loaded engine operating conditions, the engine load was assessed with reference to the pressure gauge on the hydraulic circuit, and the engine speed was assessed using a reflection-based optical tachometer by Lutron Electronic Enterprise.

The crank angle detection device consisted of an aluminium disk with 12 slots machined around its perimeter. This disk was machined in-house in the Mechanical Engineering Workshop at USQ. The disk was fastened to the engine shaft. The slots were 3 mm in width, except for one slot which was 6 mm in width.

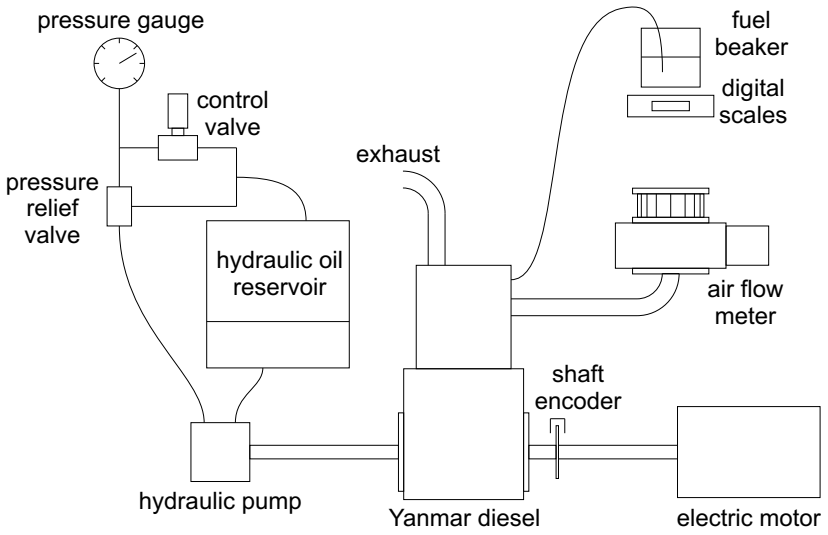

Figure 4.2: Engine dynamometer and associated instrumentation.

The radial length for all the slots was 8 mm. The larger slot was positioned at the location of TDC. A transmissive optoschmitt sensor viewed the slot-passing events and the signal was recorded on the data acquisition system for subsequent analysis of engine speed and crank angle.

The air volume flow rate was measured by a positive displacement rotary gas meter by Romet Ltd which was connected to a modified engine intake air compartment through a flexible hose. Fuel flow rate was recorded manually by monitoring the mass decrease on a digital scale over specific time intervals.

The fuel injector tube was modified in-house to include a mounting lug and pressure tap for a piezoelectric pressure transducer from Kistler Ltd (type 6125C). The lug was brazed to the middle section of the injector tube and the injection pressure signal from the fuel injector tube was used to identify the start of injection and the injection duration. The magnitude of the pressure signal was not used in subsequent analysis. The fuel injection timing data is important in the thermodynamic simulation work which uses the injection profile of the diesel fuel as an input for the calculations.

Table 4.3: Dynamometer hardware details

Parameter	Values and Information
Electric motor	3-phase electric motor by CMG Electric Motors, rated power 0.56 kW, rated voltage 415 V, frequency 50 Hz.
Crank angle detection device	Transmissive Optoschmitt optical sensor by Honeywell, model HOA2001, voltage supply 5V, rise time 60 ns.
RPM measuring device	Optical tachometer by Lutron Electronics Enterprise, 5 to 100 000 RPM.
Hydraulic pump	Salami Hydraulics, model KV 1P-D, 3.8 cm^3/rev.
Pressure relief valve	T-type, 1/2 inch.
Pressure gauge	Stauff Corporation, Model no. SPG 100, 0-315 bar (0-4000 psi).
Control valve	Needle valve, 1/2 inch.
Air flow meter	Rotary air meter from Romet Ltd, model no. RM30, max capacity 30 m^3/hr, min capacity 1.5 m^3/hr.
Digital scales	Digital scale from Wedderburn Ltd, model Vibra SJ, max weight 6200 g, min weight 1 g.

4.4 Combustion Pressure and Data Acquisition

The head of the engine was machined to accept two instruments: a pressure transducer and a radiation or convection heat flux probe. An illustration of the relative locations of these devices is shown in Figure 4.1. The pressure sensor was a Kistler pressure transducer with model number 6125C coupled to the charge amplifier and signal conditioner model number SCP slim type 2852A11.

Signals from the pressure sensor and heat flux probe were delivered to a data acquisition system (DAQ) by National Instrument. The crank angle detection device signal and the signals from the radiation probe were coupled to a NI-9234 module of the DAQ system while the pressure signal was coupled to a NI-9205 module of the DAQ system. The voltage range of these two modules is different: the NI-9234 caters for $\pm 10\,\mathrm{V}$; the NI-9205 caters for $\pm 5\,\mathrm{V}$ – well suited to the output ranges of the respective sensors.

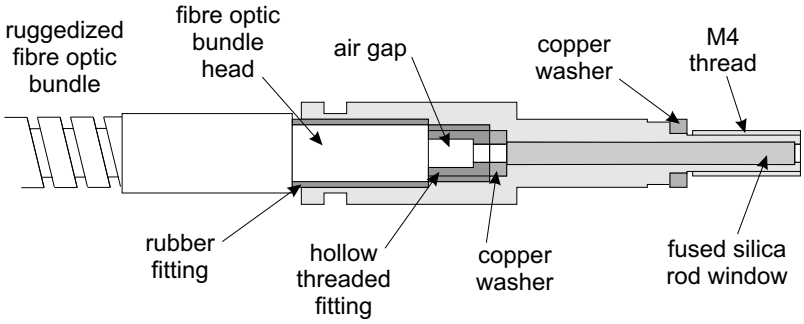

Figure 4.3: Cross sectional view of the radiation probe which is screwed into the engine head.

Integration of the two modules in the overall DAQ introduces a repeatable delay time between the data recorded via the two modules and this delay varies with sampling rate. For the sampling rate of 51200 Hz, which was used in the experiments, the delay identified through the National Instruments documentation [45] was 753.2 μs and this delay was verified by experiments performed with a signal generator in the present work. The delay was accommodated in the subsequent data analysis.

4.5 Radiation Probe

The radiation probe was designed and fabricated in-house in the Mechanical Engineering Workshops at the University Southern Queensland. The radiation probe which is illustrated in Figure 4.3 was screwed into the engine head and received radiation from the combustion chamber. Through an arrangement of two bifurcated fibre optic bundles, Figure 4.4, radiation was delivered to three separate photodetectors, Figure 4.5, each using a filter at a different wavelength.

The radiation heat flux probe was designed with the objective of creating a reliable in-cylinder radiation receiver with minimal interference to the normal combustion gas flow condition inside the engine. Hence, the probe was installed approximately

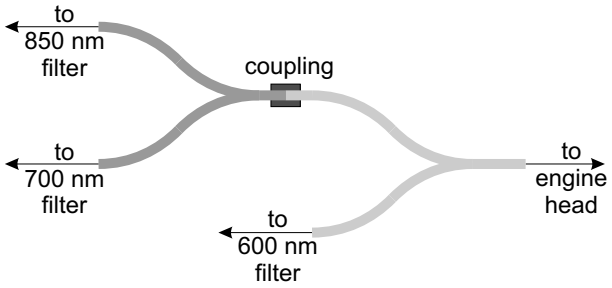

Figure 4.4: General arrangement of the optical detection apparatus used in conjunction with the radiation probe.

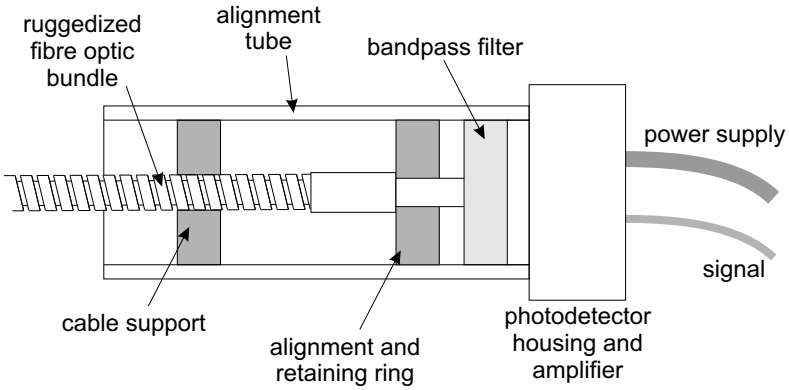

Figure 4.5: General arrangement of each of the photodetectors.

flush to the engine head surface. Due to the slight angle of the threaded hole for the radiation probe relative to the head surface, a recess about 1 mm occured on the side of the hole nearest the centreline of the cylinder. The body of the probe was fabricated in steel.

A 2.0 mm diameter, 24.5 mm long fused silica rod window was fitted in the radiation probe. The probe aperture nearest the combustion chamber was 1.7 mm in diameter. A copper washer was located at the other end of the rod window using an hollowed M3 grub screw with a clear aperture of 1.5 mm. The copper washer together with the grub screw proved adequate for sealing the high pressure combustion gases – during the experiment, no gas leakage was detected.

Prior to using the fibre optic bundles, an attempt was made to use a trifurcated fiber optic based on plastic fiber with an input aperture size of 1 mm but insufficient transmission was registered at the three outputs (aperture size of 0.5 mm each). Based on preliminary testing with a candle flame and on the Planck curve for representative combustion temperatures in the diesel flame, it was anticipated that the radiation intensity at 600 nm would be substantially lower than at 700 and 850 nm and hence the light delivered to the 600 nm filter and detector combination was received from the engine after only one fibre bifurcation, whereas the light received at both 700 and 850 nm was subjected to two fibre bifurcations. The problem of low transmission was eliminated with the use of two bifurcated glass fiber optic devices with an overall aperture size of 3.175 mm diameter.

In comparison with previous radiation research work, the single cylinder engine used in the present study appears to be the smallest – it has about one-third of the volume of the smallest engine reported in other literature. (Cylinder sizes used by other researchers vary in the range of 0.86 L to 2.33 L.) This posed a challenge for the radiation probe design because of the reduced area within which it had to be located, yet the requirement to gather enough radiation for the signal-to-noise ratio to be sufficiently high, plus the requirement for the probe to be sturdy enough to withstand the high gas pressures during compression

and combustion. In terms of size and structure, constraints were posed by the diameter of available quartz rod and the diameter of the selected fiber optic bundle. A good arrangement may have been with the fiber optic bundle installed very close to combustion chamber surface, but there was not enough solid volume in the engine head for the size of the fiber optic bundle. The difficulties were compounded by the fact that the Yanmar diesel engine head structure has a hollow section which allows the engine head to be cooled by the flow of air. The quartz rod which was 2.0 mm in diameter was therefore included in the design in an effort to optimize the amount of radiation gathered from the engine, yet with the tip of the probe being small enough to fit in the available solid volume. The quartz rod length of 24.5 mm was selected as being sufficiently long to enable the fiber optic bundle diameter to fit within the available space within the probe and engine head at this location, somewhat further from the combustion chamber surface. The spacing between the quartz rod and the fiber optic bundle was necessary as the hollowed M3 grub screw and copper washer was fitted in-between to hold the quartz rod and stop any gas leakage from the circumference of the quartz rod, as shown in Figure 4.3.

The ends of the fibre optic bundles were mounted in a phototube allowing the delivery of light directly onto three separate filters each of an arrangement illustrated in Figure 4.5. The three optical filters had centre wavelengths of 600, 700, and 850 nm and each filter had a bandpass width of 40 nm. The three optical filters were supplied by Thorlabs Inc and the model numbers were B600-40, B700-40 and B850-40 respectively. The three photodetectors used in the present work also were Thorlabs devices with adjustable amplification. The model number used for the 600 nm and 700 nm wavelengths was PDA55 (two items) with amplification setting of 40 dB and for the 850 nm wavelength the PDA36A was used with amplification setting of 60 dB.

In theory, only two measurements with filters of different wavelengths are needed for the two-colour technique, but an extra measurement at another wavelength

can serve as a check on the deduction of the two-colour mechanism parameters [24, 7]. In the present work, all three measurements were used and a least-squares error minimisation was applied to deduce the model parameters.

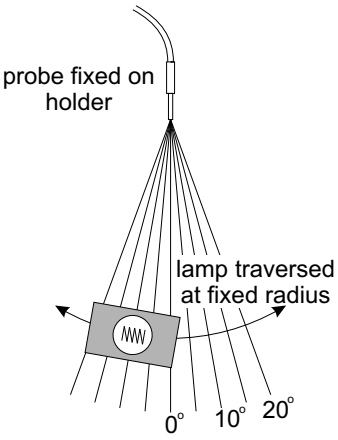

Figure 4.6: Arrangement of the field of view experiment.

The field of view of the radiation probe was measured using the arrangement shown in Figure 4.6. The radiation probe was placed on a holder with the line of sight leveled to the centre of the filament of a 100 W halogen lamp. Voltage signals were taken from each detector at the different wavelengths (600 nm, 700 nm and 850 nm). The measurements were repeated with the halogen lamp rotated and re-positioned at increments of 1° on an arc at a constant distance from the probe as illustrated in Figure 4.6. The result from these measurements is displayed in normalized form in Figure 4.7. The full-width at half the maximum field of view from the results presented in Figure 4.7 is around 6° (the half angle value illustrated in Figure 4.7 is 3°), and if a field of view is defined based on angles where the signal strength is more than 20 % of the peak value, then the field of view is 14° (the half angle value illustrated in Figure 4.7 is 7°).

Although the probe had a fairly narrow field of view, the line of sight was directed towards the piston bowl through a region of strongly radiating flame and hence the arrangements is sufficient to capture the radiation signals due to combustion

processes. From the radiation data published in previous works [24, 23, 9, 3], the radiation signals do not generally continue past about 40° after TDC. This means that most of the radiation is emitted from a small cylinder volume close to that at TDC and this ensures the volume covered by the field of view of the probe is sufficient.

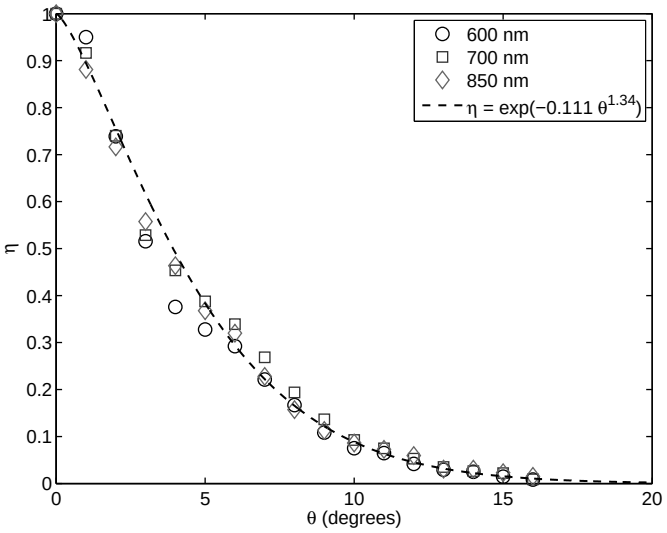

Figure 4.7: Results from the field of view experiment.

4.6 Convection Probe

A fast-response E-type coaxial thermocouple was fabricated at the University of Southern Queensland for the purpose of instantaneous wall temperature measurement for the purpose of deducing the heat transfer from the small diesel engine.

The objective of the design was to have a small-scale, effective and low-cost temperature sensor. The main components involved in this fabrication were a 2.5 mm outside diameter chromel tube of length 12.8 mm with a 0.82 mm inside diameter drilled hole, a 0.8 mm diameter constantan wire of length in the range of 45-55 mm and two copper wires of length around 400 mm.

The fabrication process for the thermocouple was as follows:

- An insulation layer was made on the constantan wire by heating it in an oven for about 30 minutes at 850°C.
- The chromel tube was inserted over the constantan wire.
- The assembly was heated for about 1 hour at 850°C to form an insulation bond between the two thermocouple elements. Near infinite resistance between the two thermocouple elements was confirmed.
- Extra length of the constantan wire near to the front surface the thermocouple was removed.
- Two copper wires were soldered at the rear of the constantan wire and the chromel tube, respectively.
- The front surface of the thermocouple was sanded using P180 grit paper to form the hot junction. The resistivity of the thermocouple circuit was tested with a voltmeter, with a target resistance of the thermocouple circuit being less than $5\,\Omega$.

The thermocouple assembly was wrapped with a thin layer (around 0.1 mm) of paper to maintain an electrically insulating gap between the thermocouple assembly and the threaded probe housing. The thermocouple assembly was bonded into the threaded probe housing using Loctite super strength retaining compound material (Loctite 620).

The sanding technique used for making the hot-junction of the thermocouple has produced a reliable junction that can withstand the severe conditions inside the combustion chamber. On occasions when the hot-junction failed, it was reactivated again through another sanding of the front surface.

A cross sectional view of the convective heat flux probe is shown in Figure 4.8 while Figure 4.9 shows a detail view of the thermocouple; a soot layer at the

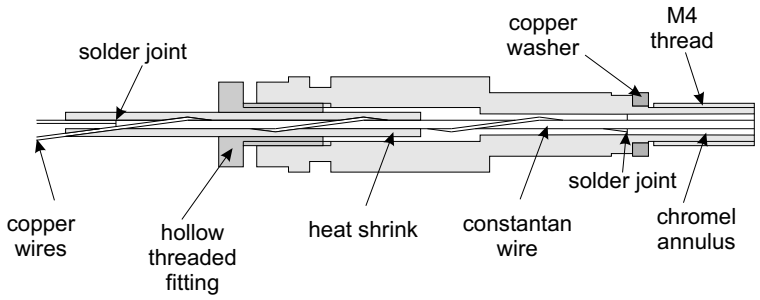

Figure 4.8: Cross sectional view of the radiation probe which is screwed into the engine head.

surface of the probe developed as a natural feature used in the diesel engine testing. The convective heat flux probe was mounted at the same location as the radiation heat flux probe and hence, the outer-features of the thermocouple probe are similar - the fitting thread, the copper sealing washer, and the outer diameter. The sealing of the probe is the same as in the radiation probe in which a copper washer that was attached to the probe by gasket sealing material (Loctite 620) was compressed against the machined seating surface in the engine head. The probe was installed approximately flush to the engine head surface. As in the case of the radiation probe, a recess about 1 mm occured on the side of the hole nearest the centreline of the cylinder due to the slight angle of the threaded hole for the radiation probe relative to the head surface. The body of the probe was fabricated in steel, as was the case with radiation probe. The connection of the thermocouple element to the amplifier circuit was achieved through copper wires attached at the end of the exposed constantan rod and at the back surface of the chromel tube. The heat flux probe was screwed into the engine head at the same location as the radiation heat flux probe, as shown in Figure 4.1.

To determine the fluctuations in heat flux from the transient surface thermocouple measurements, the thermal product $\sqrt{\rho c\, k}$ was identified based on the mean of the literature values for the two materials and an emf calibration of the thermocouple probes was performed. The thermal product is used in the calculation of the heat transfer registered by the thermocouple gauges. The conversion process can be

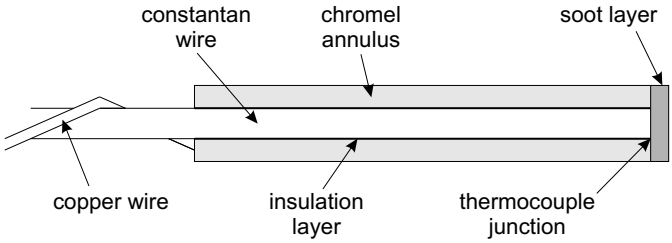

Figure 4.9: Details of the thermocouple with soot layer.

expressed as:

$$q(t) = \frac{\sqrt{\rho c k}}{\sqrt{\pi}} \int_0^t \frac{\frac{\mathrm{d}T}{\mathrm{d}\tau}}{\sqrt{t-\tau}} \mathrm{d}\tau \tag{4.1}$$

where q is the heat flux through the thermocouple gauges, ρ, c and k are the density, specific heat and the thermal conductivity for the thermocouple material respectively, T is the surface temperature, t is the time of interest and τ is the integration variable (time). The thermal properties of the two thermocouple materials are given in the Table 4.4. Because the output of the thermocouple probe is in microvolts, the signals were amplified (using an in-house constructed amplifier based on the INA110 chip) and then read in by the data acquisition system (described in section 4.24). In the present work, the conversion from surface temperature data to heat flux as expressed in Equation (4.1) was actually achieved using an impulse response filtering technique similar to that described by Oldfield [46]. Further details of this method are presented in Chapter 6.

Table 4.4: Thermal properties of chromel and constantan.

Thermal property	Chromel	Constantan	Mean
Density (kg/m^3)	8730	8913	8822
Thermal conductivity (W/m.K)	19.2	21.2	20.2
Specific heat (J/kg.K)	450	390	420

Calibration of the E-type thermocouple used for convection heat flux measure-

ments in this study was performed using a hot water bath technique. The thermocouple was connected to a multimeter and was submerged into the hot water bath at a temperature initially set to 55°C, as displayed by a mercury-based thermometer, attached in close proximity to the hot junction. Readings of the voltage output from the multimeter and temperature from the thermometer were taken during the cool-down process. Results are shown in Table 4.5. The sensitivity of the E-type thermocouples used in this experiment was found to be 62.5 μV/°C.

Table 4.5: Thermocouple emf calibration.

Change in water temperature (°C)	Voltage output (mV)
52	1.9
41	1.16
35	0.803
31.5	0.59
29	0.423
26	0.25

4.7 Operating and Methods

4.7.1 Engine Operating Conditions

Four different engine operating conditions designated as Condition 1 to 4, were investigated. These were obtained at two different pressure settings for the hydraulic pump P_{hyd} (effectively two different torque values) – 40 bar and 80 bar, and two different engine speeds – 1800 RPM and 2500 RPM. Engine operating conditions are shown in Table 4.6 and values for the mass flow rate of fuel and air ($\dot{m}_f$, and $\dot{m}_a$) were deduced using instruments described in Section 4.3 and the

Table 4.6: Engine operating conditions

Condition	P_{hyd} (bar)	Speed (RPM)	$\dot{m}_f$ (grams/s)	$\dot{m}_a$ (grams/s)	IMEP (bar)	IP (kW)
1	40	1800	0.08	3.69	3.15	1.00
2	40	2500	0.11	4.80	3.31	1.46
3	80	1800	0.12	3.54	4.82	1.53
4	80	2500	0.14	4.16	4.75	2.10

indicated mean effective pressure value (IMEP) was deduced from the pressure transducer described in Section 4.4. Indicated power (IP) values are deduced from the IMEP values, the engine speed and swept volume.

4.7.2 Radiation Heat Flux Measurements

The radiation measurements were obtained at the four different engine operating conditions by following a standard procedure. The testing method outlined below makes reference to pre- and post-run calibrations of the radiation probe which are described in Chapter 5, Section 5.3.

- All connections and the settings of the instrumentation system and mechanical set-up are checked.
- The pre-run calibration process is performed. With the probe window completely clean, the radiation probe is set in the calibration rig and the bulb is powered with 12.00 V. The voltage outputs from the three detectors are recorded (with illumination and in the dark arrangement).
- The engine is arranged for an initial warm-up period with a plug installed in the engine head location where the radiation probe will later be installed so as to avoid unnecessary sooting of the radiation probe.

- A motoring period is initially used to confirm option of the data acquisition system and all sensors are confirmed as operational by checking the output displayed through the data acquisition system software.

- Fuel is introduced to the engine (the electric motor is immediately switched off) and the engine is run for a warm-up period of approximately 5 minutes and during this time, the desired engine load and speed conditions are set.

- The engine is switched off and the radiation probe is installed in the engine head. This process takes approximately 3 minutes.

- The engine is then fired and data is acquired over 10 different periods each of 10 s duration with intervals between the data acquisition periods of 60 s. The start time (in seconds) for the data recording for period n relative to the start of engine firing with the radiation probe installed is given by $t_{start,n} = (n-1)70$.

- At a time of 640 s, immediately following the conclusion of 'Period 10', the engine is stopped.

- The radiation probe is removed from the engine head without disturbing the soot layer, and the post-run calibration process is performed with the radiation probe installed in the calibration rig.

4.7.3 Convective Heat Flux Measurements

The convective heat flux measurements were obtained at the four different engine operating conditions by following a standard procedure outlined below.

- The thermocouple hot junction is refurbished and checked. The resistance of the thermocouple circuit was tested, with the target resistance being less than 5 Ω.

- All connections of the heat flux probe and the other instrumentation are checked.

- The engine is arranged for an initial warm-up period during which the required load and speed is set. During this time a plug is used in the engine head location where the thermocouple probe will later be installed so as to avoid unnecessary sooting of the thermocouple probe.

- The plug on the cylinder head is removed and the seating area above the threaded hole on the cylinder head is cleaned, before installing the thermocouple probe on the cylinder head.

- A brief motoring period is initially performed to confirm the correct option of the data acquisition system and that all sensors are operational by checking the output displayed through the data acquisition system software. Motored data is then acquired.

- The engine is then fired and data is acquired over 5 different periods each of 10 s duration with intervals between the data acquisition periods of 40 s. In this case, the start time (in seconds) for the data recording for period n relative to the start of engine firing with the convective heat flux probe installed is given by $t_{start,n} = 50n - 10$.

- The condition of the thermocouple is monitored through the observation of the output displayed from the data acquisition system software. If irregular heat flux readings occur due to either the failure of the adhesive material or the surface junction, the test is aborted and the thermocouple checked and refurbished as necessary.

- At a time of 250 s, immediately following the conclusion of period 5, the engine is stopped.

- A further period of motoring is performed and recorded to confirm the integrity of the thermocouple during the entire test.

4.8 Conclusion

Two different heat flux gauges have been successfully designed, fabricated and tested in a direct injection diesel engine for measurement of radiative heat flux and related quantities, and for the measurement of convective heat flux. The radiation heat flux probe and associated detectors were configured to obtain data through a variant of the two-colour method. The initial problem of inadequate transmission registered on the photo-detectors was solved through the use of a combination of two bifurcated glass fiber optic bundles. The convective heat flux probe relied on a surface junction thermocouple for measurements of transient surface temperature. The convective heat flux probe was used to complement the results derived from the radiation heat flux probe and thereby provide a more complete understanding of the heat losses to the wall of the small diesel engine. In both cases, experimental measurements were taken periodically – for 10 s with an interval of either 60 or 40 s in-between – in an effort to acquire sufficient data to analyse the effect of sooting and infer radiation and convective heat flux values.

Chapter 5

Results and Discussion: Radiation Heat Flux

5.1 Introduction

This chapter presents the results and discussion of the new in-cylinder radiation heat flux measurements obtained in this study. The chapter progresses with an analysis of the pressure data and a discussion of the radiation calibration results. It then proceeds with the presentation and discussion of the primary experimental results: apparent temperature data, KL values and the radiation heat flux data.

5.2 Pressure

In-cylinder pressure measurements for the engine tests performed at the four conditions as described in Section 4.7 are presented in Figure 5.1. In each case, ensemble-averaged results for the 10th data acquisition period are presented as this is the last period of measurement during the engine test and during this period, the net soot accumulation rate is minimal. However, there is very little

difference in the pressure histories recorded for all periods between 2 and 10. The standard deviations in the ensemble-averaged peak pressures across these 9 cycles are: 10.3% (7.6% for periods 3 to 10), 6.4%, 4.3%, 6.1% for the conditions 1 to 4 respectively.

In each of the four operating conditions, fuel injection starts at approximately 14°±1 BTDC, as described in the engine manual [44] and as recorded using the fuel injection pressure transducer located in about middle of the fuel injector tube. From the injection pressure measurements, fuel injection actually starts at: 14.5° BTDC for condition 1, 13.6° BTDC for condition 2, 15.9° BTDC for condition 3 and 14.7° BTDC for condition 4.

Combustion-induced pressure rise (CIPR) data, Figure 5.2, was obtained by taking the difference between the experimental pressure data and a deduced motored result obtained by fitting a polytropic curve to the pressure measurements over the range from 20° to 15° BTDC. The initial decrease in the pressure difference observed for times after 15° is attributed primarily to variations in the polytropic index with crank angle. Two values which are indicative of the start of the CIPR are identified in the present work. The first is the crank angle location where the pressure difference results in Figure 5.2 reach a minimum, and the second is the crank angle location where the pressure difference passes back through zero in the positive-going direction. The following crank angles corresponding to the pressure minima are obtained. Condition 1: 9° BTDC; condition 2: 4.5° BTDC; condition 3: 6° BTDC; and condition 4: 4.5° BTDC. The following crank angles corresponding to positive-going the zero pressure values are obtained. Condition 1: 5.5° BTDC; condition 2: 1° BTDC; condition 3: 4° BTDC; and condition 4: 1.5° BTDC.

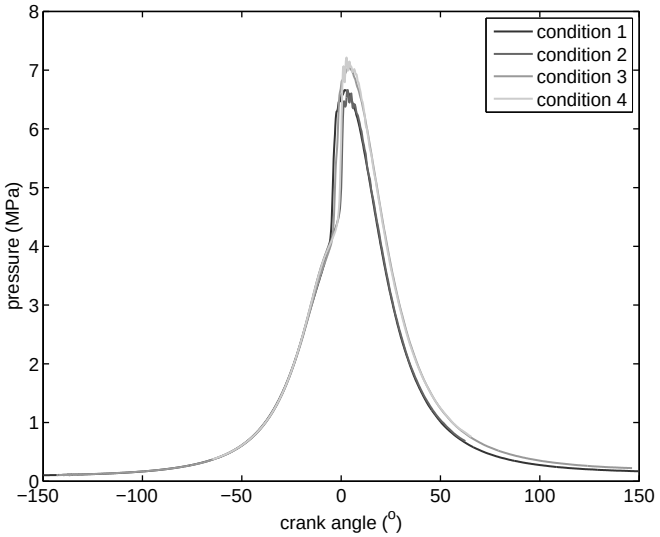

Figure 5.1: Pressure results for all four operating conditions during the 10th data acquisition period.

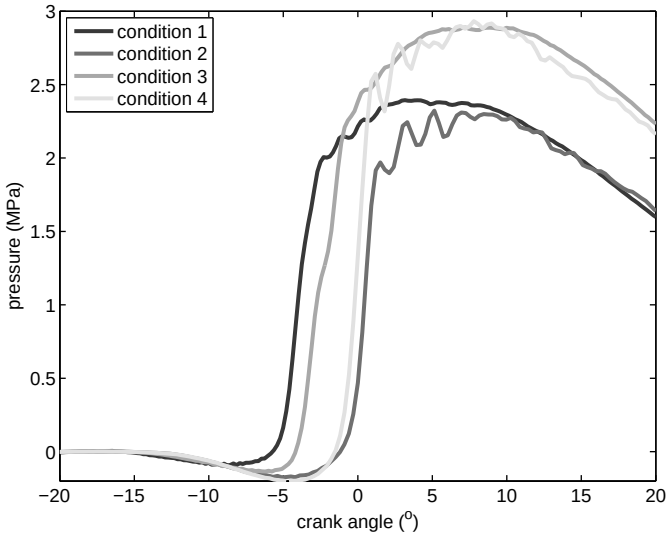

Figure 5.2: Combustion induced pressure rise results for all four operating conditions during the 10th data acquisition period.

5.3 Radiation Probe Calibration

5.3.1 Absolute Calibration

Calibration of the radiation probe is required in order to relate the voltage output signal from each of the three detectors to the radiation received at the aperture of the probe within the head of the engine. The objective of the calibration process is to identify the value of the calibration constant which is defined as the ratio of the radiation heat flux value received at the probe aperture (for the particular wavelength λ and spectral bandwidth $\Delta\lambda$ of the optical system) to voltage output of the detector. Three calibration constants corresponding to the three different optical path/wavelength/detector combinations need to be obtained. The voltage output of the photodetectors used in this experiment is linearly related to the received radiation [47, 48] and it is assumed that there are no nonlinear effects associated with any of the optical paths from the probe aperture to the detectors. Therefore, the strategy adopted here involves a two-point calibration for each of the three systems: voltage outputs are recorded for no optical input signal, and voltage outputs are recorded for the irradiance received at the probe aperture from a stable source with known irradiance.

For radiation probe calibration, previous researchers have used a disappearing filament optical pyrometer to deduce an apparent temperature for the radiation source such as a black body furnace or a tungsten filament calibration source and radiation intensity that is applied from the source to the probe is calculated indirectly [49, 23, 37]. Struwe et al. [24] used a radiant power meter to characterise the calibration source input into the probe system.

In the present work, probe calibration was achieved using a United States' National Institute of Standards and Technology (NIST)-calibrated 1000 W lamp from Optronic Laboratories Inc. The lamp was supplied with spectral irradiance results ($\mathrm{W/m^2{\cdot}nm}$) as a function of wavelength, $I(\lambda)$ specified at a distance of

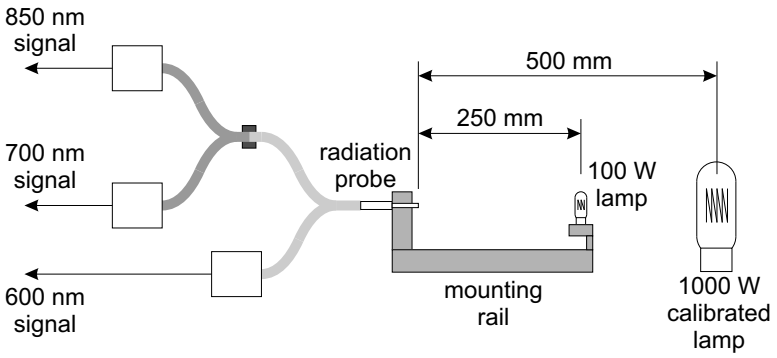

Figure 5.3: Illustration showing probe calibration arrangments. The 100 W lamp was used the relative calibration work, and the 1000 W lamp was used for the absolute calibration.

500 mm from the lamp. The quartz window at the aperture of the radiation probe was cleaned and the probe was attached to a fixed bracket on an aluminium base and was positioned 500 mm from the calibrated 1000 W lamp as shown in Figure 5.3. For each of the three detectors, the voltage signals produced in a dark environment were subtracted from the voltage readings with the illumination from the calibration lamp ΔV_i. Calibration constants C_i ((W/m^2·nm)/V) for each optical path/filter/photodetector case $i = 1$, 2, or 3 were then determined according to

$$C_i = \frac{I(\lambda_i)}{\Delta V_i} \tag{5.1}$$

5.3.2 Relative Calibration

The absolute calibration of the radiation probe (Section 5.3.1) was performed only once because of the limited space available in the engine test laboratory which made it difficult to conveniently position the power supply for the standard lamp, and the limited availability of the standard lamp (which was borrowed from another research group). However, sooting of the fused quartz window surface of the probe during engine operation made it necessary to calibrate the probe

at regular intervals. This was achieved using a smaller bulb (100 W) which did not have a particular irradiance calibration, but was operated in the manner of a standard reference source, Figure 5.3.

Prior to any particular engine experiment, the probe window surface would be cleaned thoroughly with a glass cleaning liquid and degreaser and positioned at the standard location in the calibration rig, Figure 5.3. The voltage values from the three photodetectors were then recorded. Removal of the radiation probe from the head of the engine and insertion into the calibration rig location required disassembly and reassembly of the fibre optic bundle and the probe. There was some sensitivity of the photodetector output to the orientation of the fibre optic bundle in the probe so alignment marks were used to aid correct assembly. Repeatability of the calibration method was assessed using the 100 W bulb arrangement. The probe was disconnected and reconnected ten times in a similar manner to that which occurred during the engine test program. Voltages from the photodetectors were recorded and were found to be consistent to within a $\pm 0.5\,\%$ span of the mean readings.

Immediately following any particular engine experiment, the probe was removed from the engine head, and *without* cleaning the window, the probe was assembled into the calibration rig. Measurements of voltage output from the three detectors were recorded using the 100 W lamp under these sooted-probe conditions. By comparing the ratios of voltages obtained from the clean- and sooted-probe cases, it is possible to deduce the impact of the soot accumulation during the experiment on the attenuation of radiation signals in an absolute sense because the clean-window results with the 100 W bulb correspond to the calibration configuration with the calibrated lamp described in Section 5.3.1. Thus, the absolute calibration constant ($(W/m^2.nm)/V$) for each detector at the end of the experiments can be

deduced using

$$C_{i,final} = C_i \frac{\Delta V_{i,initial}}{\Delta V_{i,final}} \tag{5.2}$$

where $\Delta V_{i,initial}$ and $\Delta V_{i,final}$ are the voltage differences between the 100 W bulb calibration constant and the dark calibration value for detector i taken before and after a set of engine experiments, and C_i is the absolute calibration constant from the standard lamp, the NIST-calibrated light source.

5.3.3 Compensation for Sooting During Experiments

During engine operation, accumulation of a soot layer caused attenuation of the radiation received by the photodetectors. Thus, the calibration constant that would apply in the case of a clean window (as obtained from the absolute calibration, Section 5.3.1) would not apply during the engine operation. Similarly, the calibration constant deduced from the relative calibrations performed before and after the engine experiments (Section 5.3.2) would also not apply, except at the very end of the engine test period since there is a more or less *gradual* accumulation of soot during engine operation.

Figure 5.4 illustrates how the instantaneous (crank-resolved) voltage outputs from one of the detectors varied over time for one particular engine operating condition. It can be observed that the voltage signals not only decrease in magnitude with the progression of time from the start of the engine testing (period 1 to period 10), but that results from the different periods also differ in shape. At this condition, the magnitude of the peak value (at around 10° ATDC) is reduced in a more or less regular manner and at period 10, the value is reduced relative to that of period 2 by a factor of around 5. Data for period 1 were obtained for times between 0 and 10 s after initially firing the engine, so are expected to be influenced by engine warm-up effects. The shape of the voltage output around

period 7 is characterised by two peaks: the first at about 2° ATDC, and the second at about 10° ATDC. Changes in the shape of the crank-resolved signal are attributable to: (1) an uneven accumulation of soot on the window of the probe; (2) non-uniform radiating soot cloud development within the field of view; and (3) coupling efficiency variations for the radiation entering the probe from different angles. Non-uniform radiating soot cloud development may result from the swirl type motion of the diffusion flame plumes. The movement of a radiating plume or flame away from the field of view while another plume travels into the field of view would result in the presence of second peak or hump in the crank resolved radiation signal.

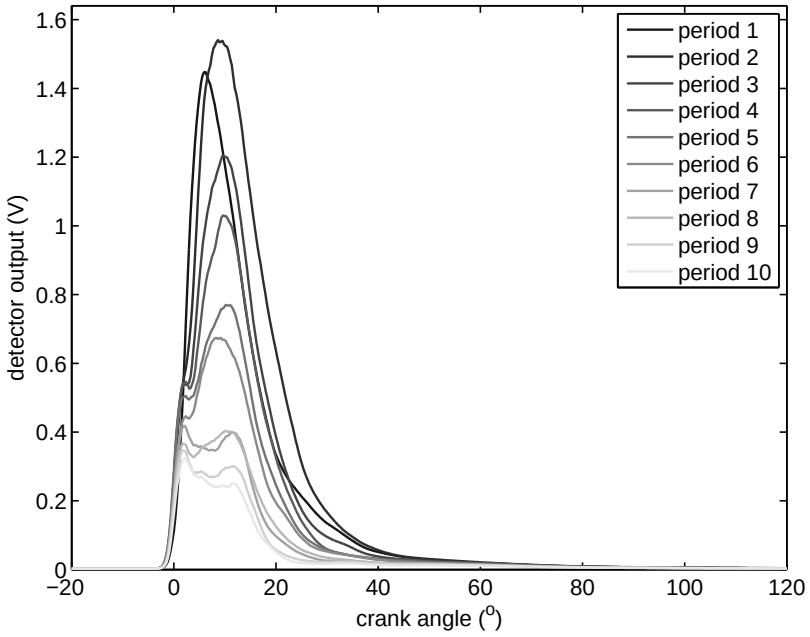

Figure 5.4: Detector voltage output (700 nm case) as a function of crank angle for condition 4. Period 1 corresponds to data obtained from 0 to 10 s after the start of the engine testing, and period 10 corresponds to data obtained from 630 to 640 s, with the other periods evenly distributed between them.

In an effort to accommodate the gradual sooting effect and yet consider the radiation data from the majority of the engine test periods, the condition of the soot layer during the final period of operation (period 10) was assumed to be the same as that which was present when the post-run calibrations were performed

(Section 5.3.2). This appears to be a reasonable assumption because: (1) the relative changes due to soot accumulation are diminishing with time as evidenced by the modest changes in signal profile between period 9 and period 10 (Fig. 5.4); (2) the fuel delivery was terminated immediately at the conclusion of the period 10; and (3) the calibration of the probe was performed immediately following engine shut-down. Thus the post-run calibration factors for the three wavelengths $C_{i,final}$ are taken as applicable during period 10, $C_{i,10} = C_{i,final}$. Calibration constants for any particular period are then defined based on a particular signal indicator recorded for the ensemble-averaged result for that period $V_{ind,n}$ relative to that obtained for period 10 $V_{ind,10}$ as shown below.

$$C_{i,n} = C_{i,final} \frac{V_{i,ind,10}}{V_{i,ind,n}} \tag{5.3}$$

where n is an index referring to the period number between 1 and 10. This signal indicator (subscript 'ind') is the quantity that represents the strength of the ensemble-average voltage of the particular period. Three signal indicators have been trialled: (1) an integrated value, (2) a peak value and (3) a peak value at constant CA. The differences and the advantages of each indicator are discussed in the following section. With this approach, it is effectively assumed that the ensemble-averaged radiation heat flux emissions from the combustion chamber remain constant with time (after the engine operating condition is stablised which appears to occur shortly after the conclusion of period 1).

5.3.3.1 Integrated Value Calibration Constant Approach

Integrated value calibration constants are produced by integrating voltage signals for the last interval (period 10, just before engine shut-off) and normalizing that value with the corresponding integrated value for each period and multiplying the result by the calibration constant that is produced during the post-test calibration as shown in Equation (5.3). The integrated value for each period is useful data

that accommodates the shape and the magnitude of the signals to some degree. Voltage output signals from about 200-300 cycles were integrated across the time taken for the signals to rise from 10% of the maximum signals until drop to 10% of maximum signal. Figure 5.5 shows the spectral emissive power for condition 4 at 700 nm using the integrated value calibration constant. The spectral emissive power results are relatively close to each other with the difference between the highest peak and lowest peak being 25% of the highest peak. In contrast for the raw voltage data output of the same condition (as shown in Figure 5.4), the difference was 85% of the highest peak value. The result shows that the attenuation of the signals due to soot deposition can be compensated by applying the ratios of integrated values (as outlined above) and this ratio reflects the loss of signal due to soot accumulation. However, the shape of the emissive power profiles for each period remains different.

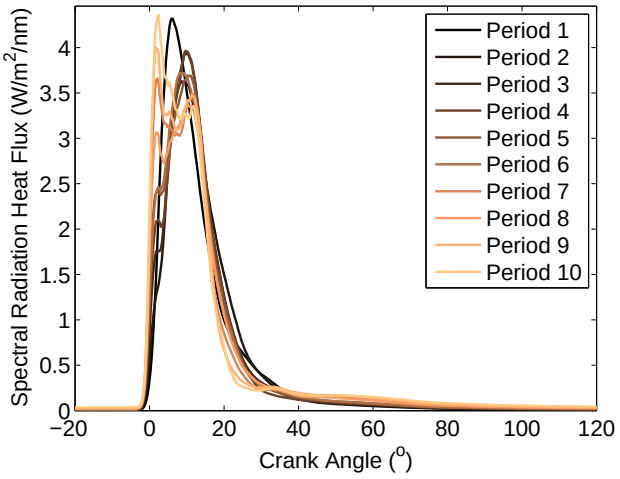

Figure 5.5: Spectral emissive power based on an integrated value calibration as a function of crank angle at the filter wavelength of 700 nm for condition 4.

Figures 5.6 to 5.9 show the calibration constant obtained from the integrated value calibration factor approach for each period from period 2 to period 10 for each the engine operating conditions for all three wavelengths. In general, the calibration constants increase with time, which shows the effect of radiation signal attenuation due to soot deposition.

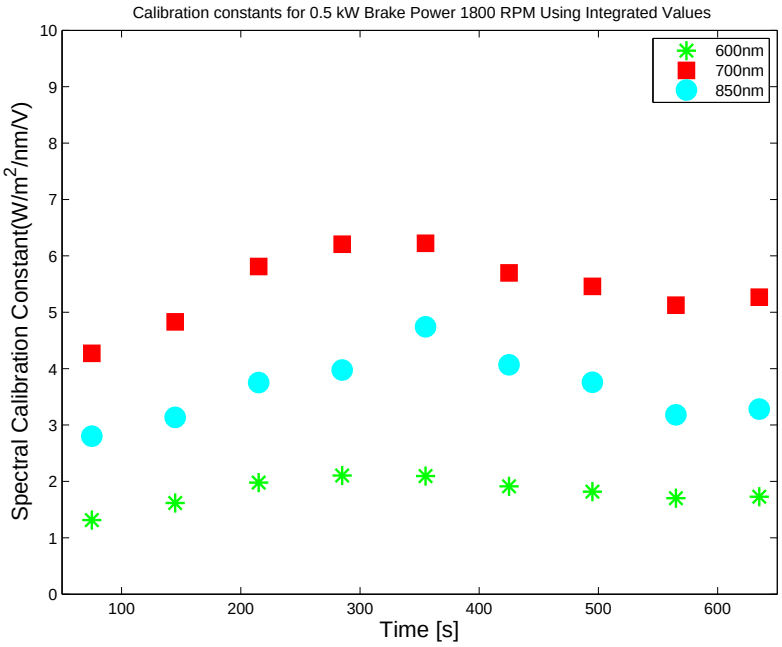

Figure 5.6: Calibration constants using integrated voltage values as a function of time for condition 1.

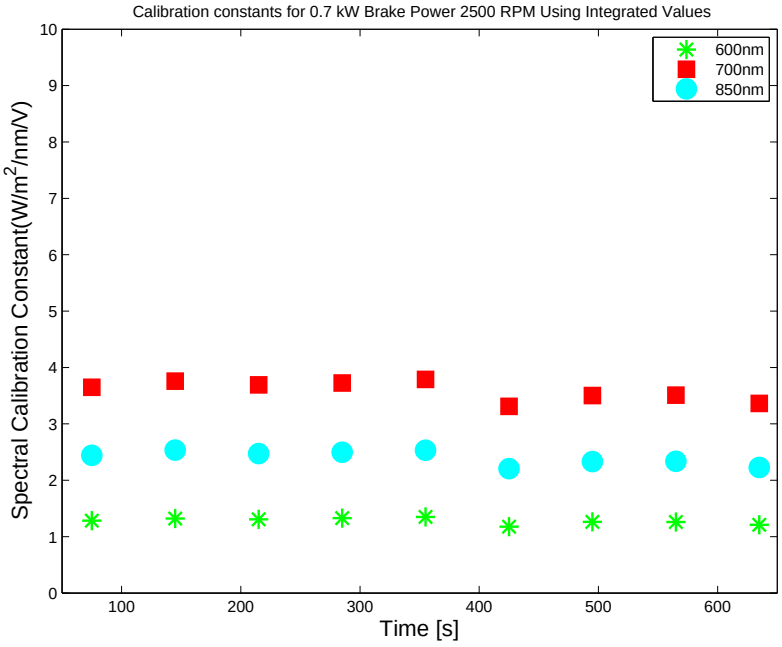

Figure 5.7: Calibration constants using integrated voltage values as a function of time for condition 2.

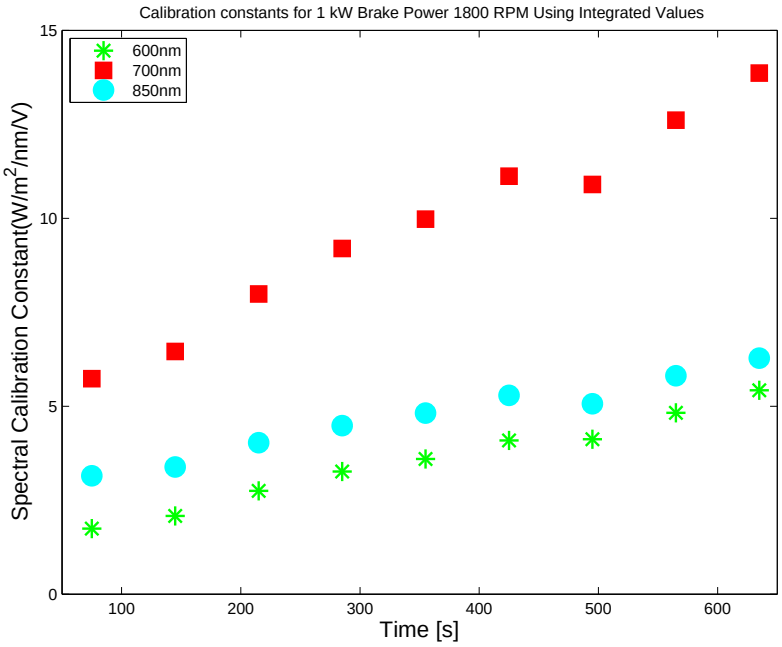

Figure 5.8: Calibration constants using integrated voltage values as a function of time for condition 3.

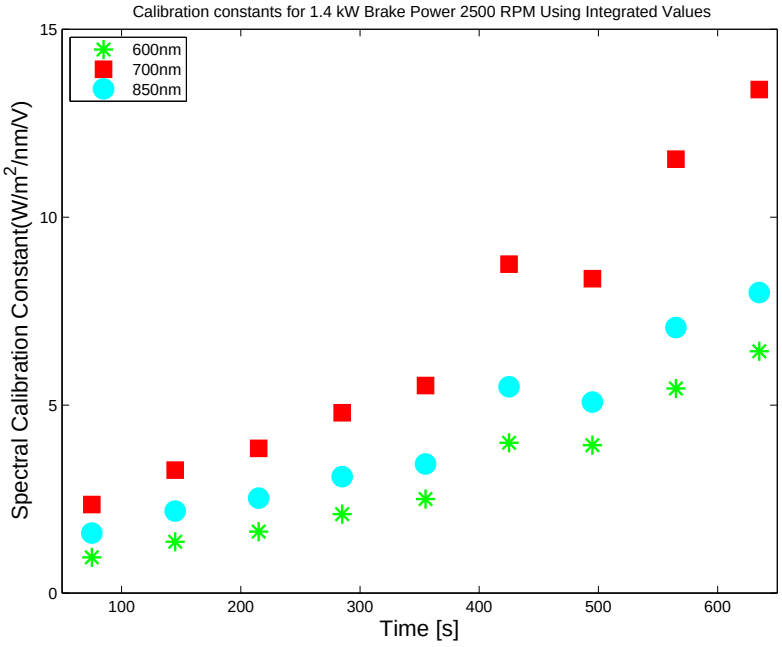

Figure 5.9: Calibration constants using integrated voltage values as a function of time for condition 4.

5.3.3.2 Peak Value Calibration Constant Approach

Peak value calibration constants are produced by identifying the peak value of the ensemble-averaged spectral voltage signals for the last period just before engine shut-off and normalizing that value with the corresponding peak value for each period and multiplying the result by the calibration factor of the post-test calibration, as described in Equation (5.3). Peak value data of the interval describes the maximum intensity of the radiation heat flux during the period and it is a useful indicator data of the signal strength that can be used to compensate attenuation of the signals.

Figure 5.10 shows a result of spectral emissive power for the 700 nm wavelength channel produced using the peak value calibration constant approach. The calibration constant using the peak value as signal strength indicator will obviously produce a constant peak radiation heat flux for all the periods. The peak values of the spectral emissive power for all the periods are the same magnitude, which is at 4.36 $W/m^2 \cdot nm$ in this case.

In comparison with the result from the integrated value calibration constant, the magnitude of spectral emissive power produced by the peak value calibration constant is generally slightly higher. However, the overall shape of the emissive power produced using the peak calibration constant appears to be similar to the integrated value result.

Figures 5.11 to 5.14 display the calibration constants produced by using the peak value approach for period 2 to period 10 for all four engine operating conditions for the three wavelengths. In general, the calibration constants produced using peak values show the same pattern observed in the integrated calibration constant approach: values generally increase with the engine running time reflecting the soot deposition process.

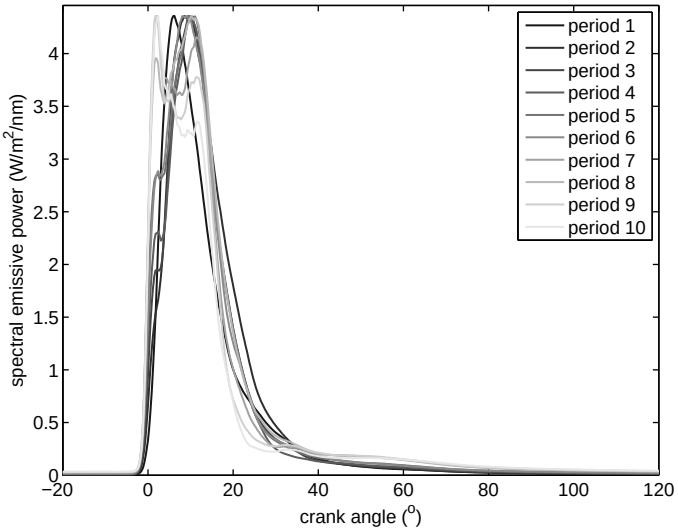

Figure 5.10: Spectral emissive power based on a peak value calibration as a function of crank angle at the filter wavelength of 700 nm for condition 4.

5.3.3.3 Peak at Constant CA Value Calibration Constant Approach

Peak value calibration constants at a constant CA are produced by considering the voltage signal values for each wavelength a particular constant CA, which is identified as the CA at which the maximum voltage signal occurs for all periods, between 2 and 9. The voltage values at this CA for the last period (just before engine shut-off) are normalized using the corresponding voltage values for each period and results are multiplied by the calibration constant produced by the post-test calibration, as shown by the Equation (5.3).

Figure 5.15 shows the result of spectral emissive power for the 700 nm wavelength signal using peak values at constant CA calibration constants for condition 4. The peak values of the spectral emissive power are not constant as in the case of the peak calibration constant approach. In terms of the shape, the result produced is similar to other calibration approaches with a more rapid rise and fall occurring for the spectral emissive power results for the later periods.

Plots of calibration constants as a function of time for the peak voltage at con-

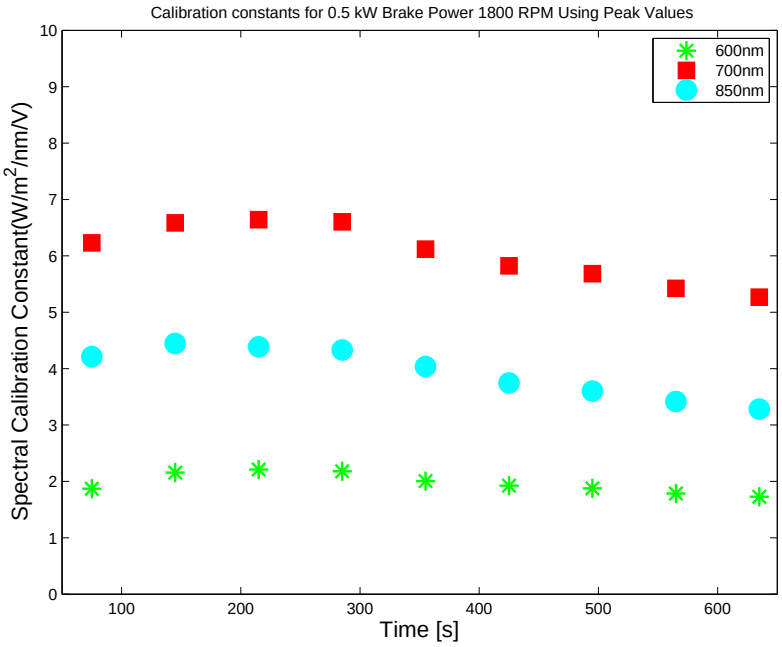

Figure 5.11: Calibration constants using peak voltage values as a function of time for condition 1.

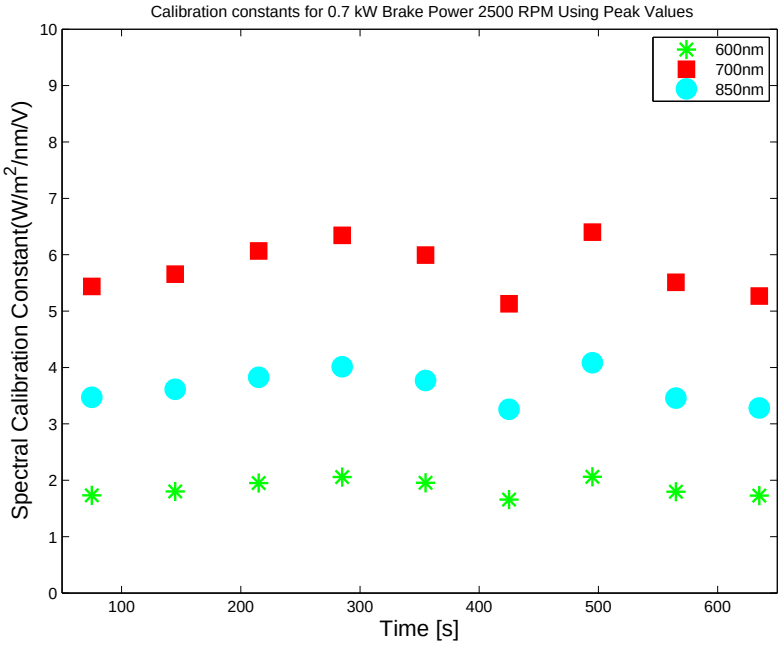

Figure 5.12: Calibration constants using peak voltage values as a function of time for condition 2.

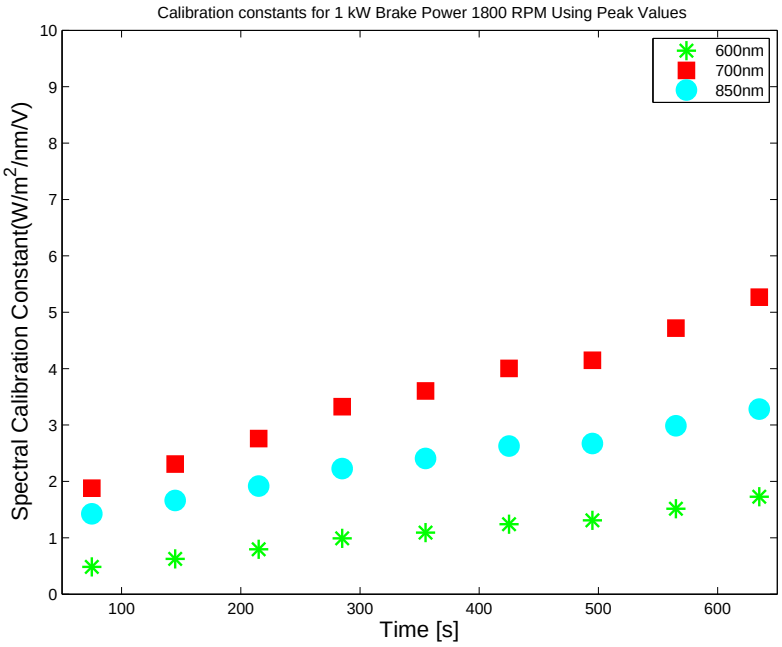

Figure 5.13: Calibration constants using peak voltage values as a function of time for condition 3.

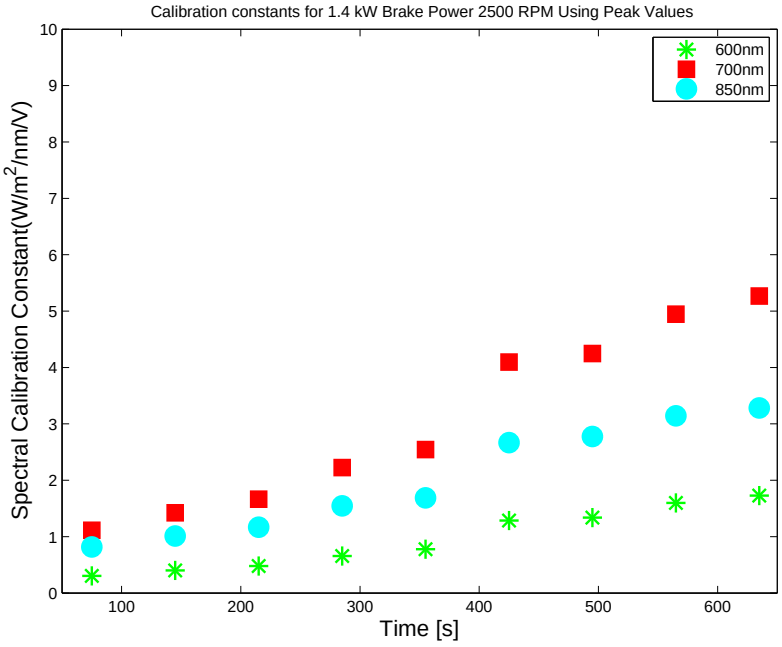

Figure 5.14: Calibration constants using peak voltage values as a function of time for condition 4.

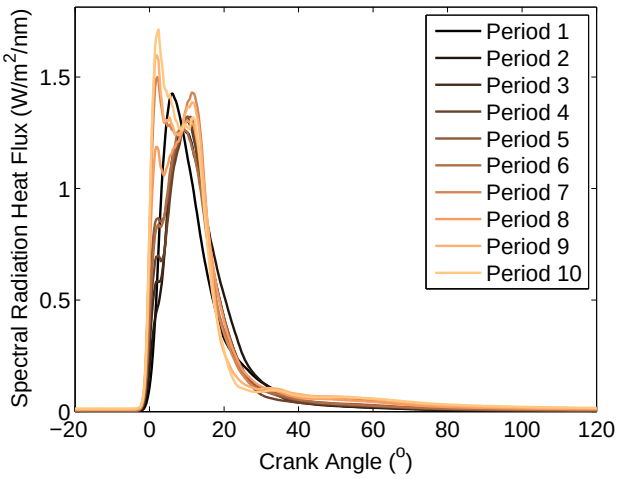

Figure 5.15: Spectral emissive power based on a peak value at constant CA calibration as a function of crank angle at the filter wavelength of 700 nm for condition 4.

stant CA approach are shown in Figure 5.16 to 5.19 for all four engine operating conditions. The calibration constants obtained are in the range of values as in peak voltage calibration constant approach.

5.3.3.4 The Choice of Calibration Constant Approach

For subsequent work, the peak calibration constants approach has been adopted. Using the peak signal (voltage) values for the scaling of the calibration constant obviously ensures the peak emissive power values for all of the periods are the same magnitude, but clearly the detailed distribution of the apparent emissive power as a function of crank angle is not maintained the same for each period and this effect is attributable to non-uniformities in the source (soot cloud) and detection system as discussed previously in Section 5.3.3.

An indication of the significance of the unresolved variability with the current approach can be obtained by considering the variation in the cycle-averaged results when the calibration constant is based on the peak signal results. Over the 10 data acquisition periods for the results presented in Figure 5.10, the cycle-

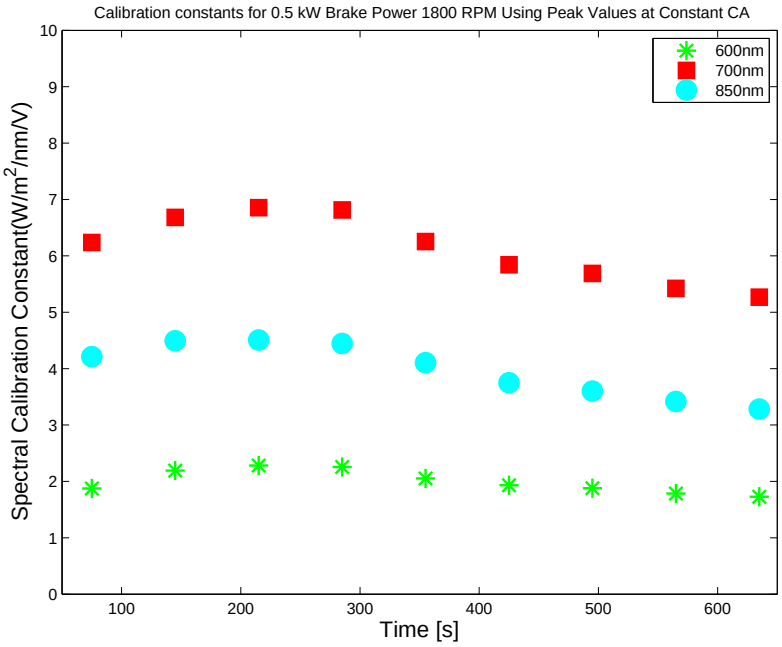

Figure 5.16: Calibration constants using peak voltage values at constant CA as a function of time for condition 1.

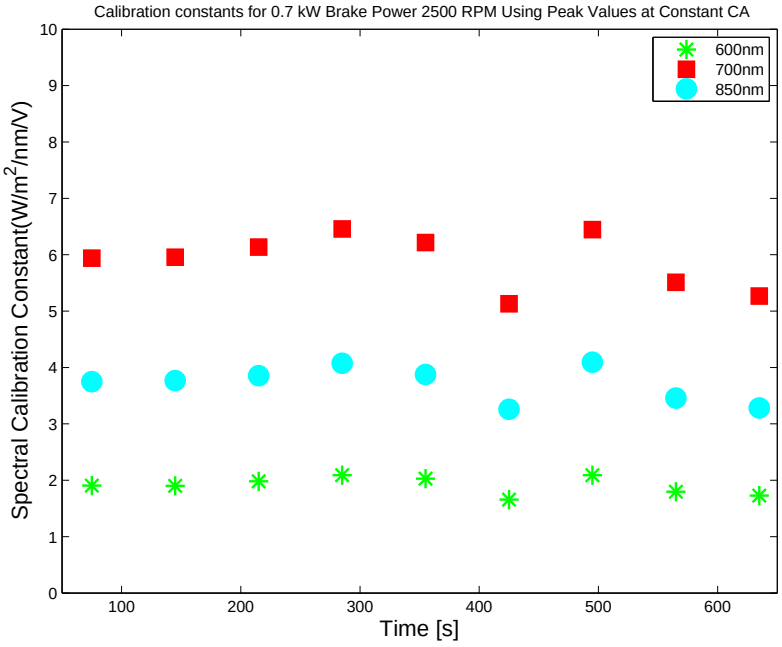

Figure 5.17: Calibration constants using peak voltage values at constant CA as a function of time for condition 2.

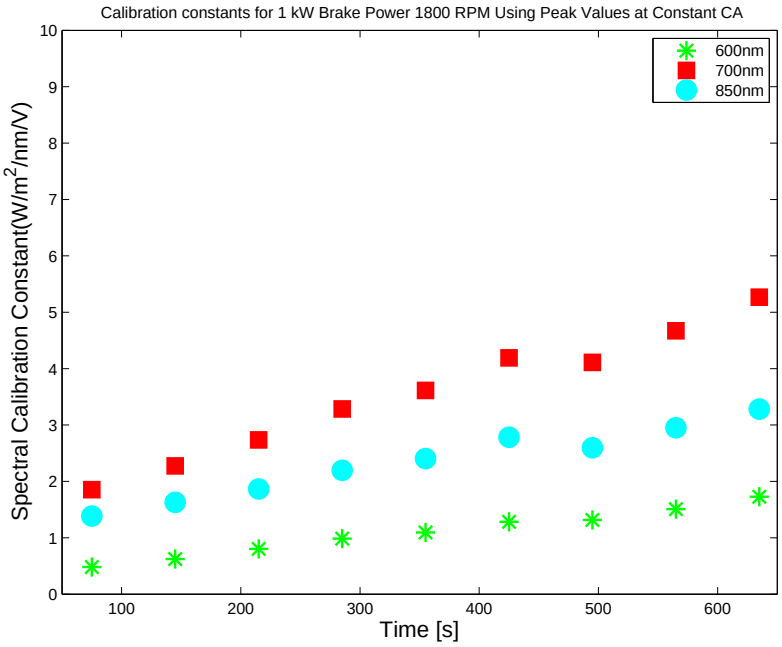

Figure 5.18: Calibration constants using peak voltage values at constant CA as a function of time for condition 3.

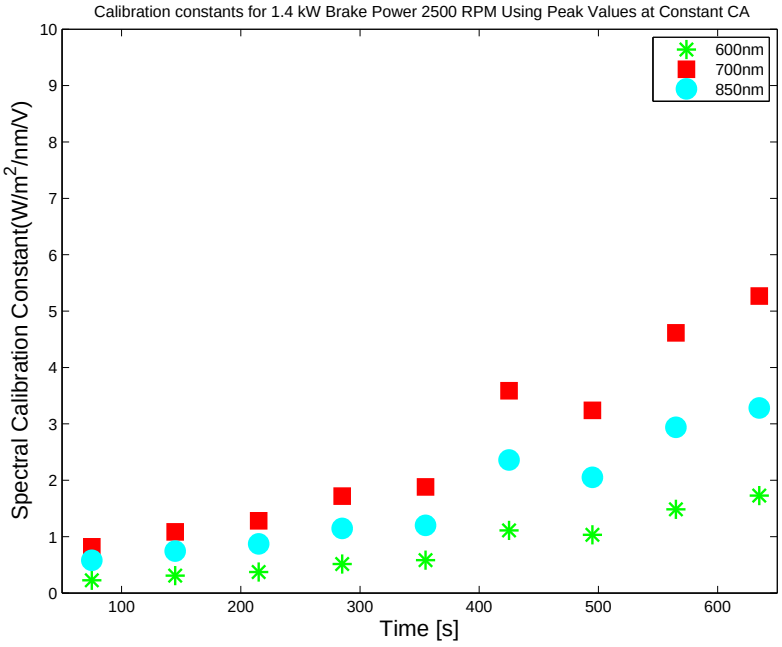

Figure 5.19: Calibration constants using peak voltage values at constant CA as a function of time for condition 4.

averaged spectral emissive power at 700 nm was: 0.0968, 0.1971, 0.1966, 0.1977, 0.1964, 0.1969, 0.1966, 0.1964, 0.1969 and 0.1975 W/(m^2.nm), giving an average value of 0.1869 W/(m^2.nm), with a two times the standard deviation value (2σ) value of 0.063 W/(m^2.nm). If the first period is neglected on the grounds that it is influenced by warm-up effects, then the corresponding value for the mean cycle-averaged spectral emissive power is 0.1969 W/(m^2.nm), with a two times the standard deviation value of 0.00093 W/(m^2.nm) corresponding to an uncertainty of $\pm$0.5%.

5.4 Apparent Temperatures

Figure 5.20 to 5.23 present the apparent temperature of the soot cloud as deduced from the present implementation of the two-colour method. In condition 1, the apparent flame temperature rises rapidly from around 7.6° BTDC, in condition 2: 3.6° BTDC, condition 3: 6.3° BTDC, and condition 4: 3.3° BTDC. These results are consistent with the first registration of the combustion-induced pressure rise (Section 5.2).

Conditions 1 and 2 have yielded temperatures around 2100 K which are slightly higher than the temperatures identified from conditions 3 and 4 which were around 1950 K (Figure 5.20 to 5.23). In all cases, the apparent flame temperature remains relatively constant to about 20° ATDC, by which time the emissivity of the soot cloud drops to very low values and hence the signal registered on each of the wavelength channels becomes very small. Apparent soot cloud temperature values identified in the present work are consistent with those obtained by other workers for diesel engine combustion diagnosed using the two-colour method [22, 23, 7, 25]. For example, the range of flame temperature values reported by Struwe [7] using a 2.3 L engine was 1800 to 2500 K for load conditions of 50, 75 and 100 % with the peak apparent flame temperature values decreasing with the increase of load. In the present work, for condition 1 and 2, the peak apparent

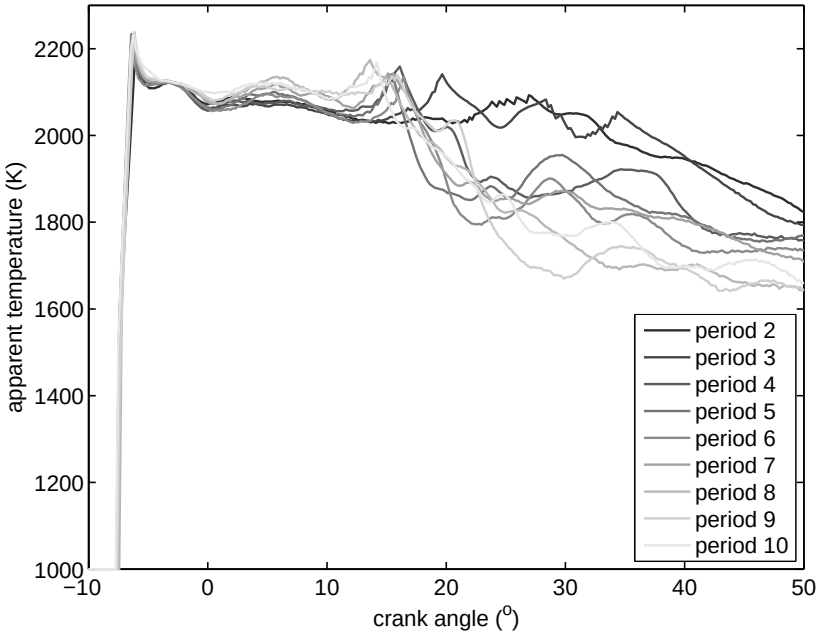

Figure 5.20: Apparent flame temperature results as a function of crank angle for condition 1.

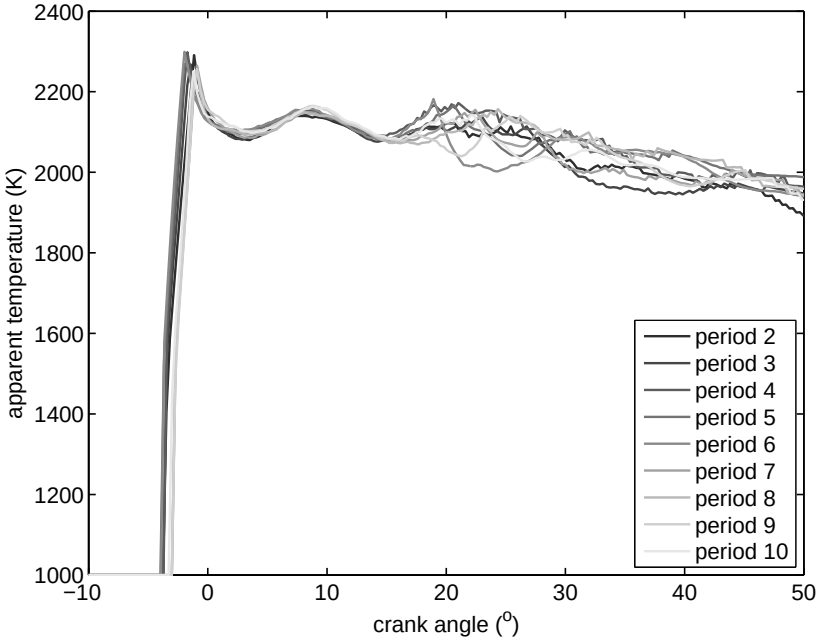

Figure 5.21: Apparent flame temperature results as a function of crank angle for condition 2.

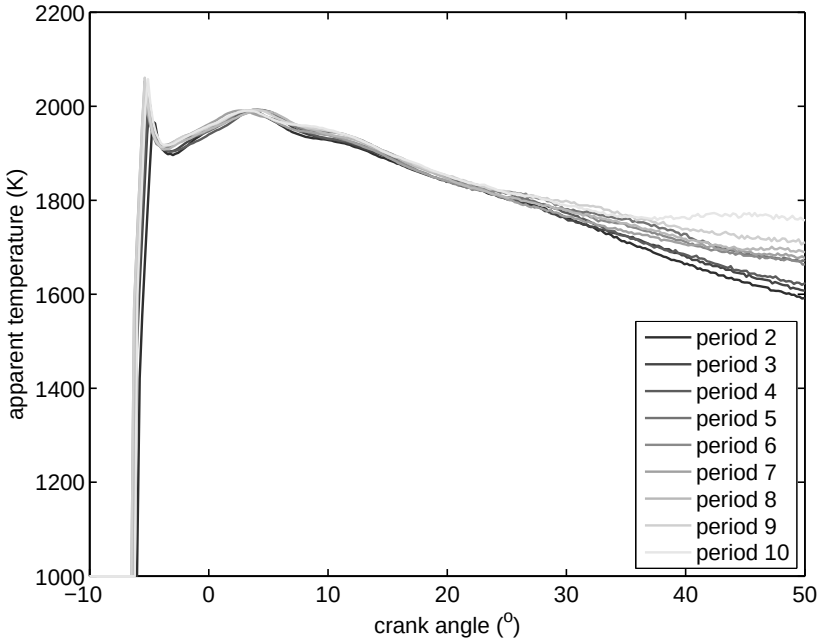

Figure 5.22: Apparent flame temperature results as a function of crank angle for condition 3.

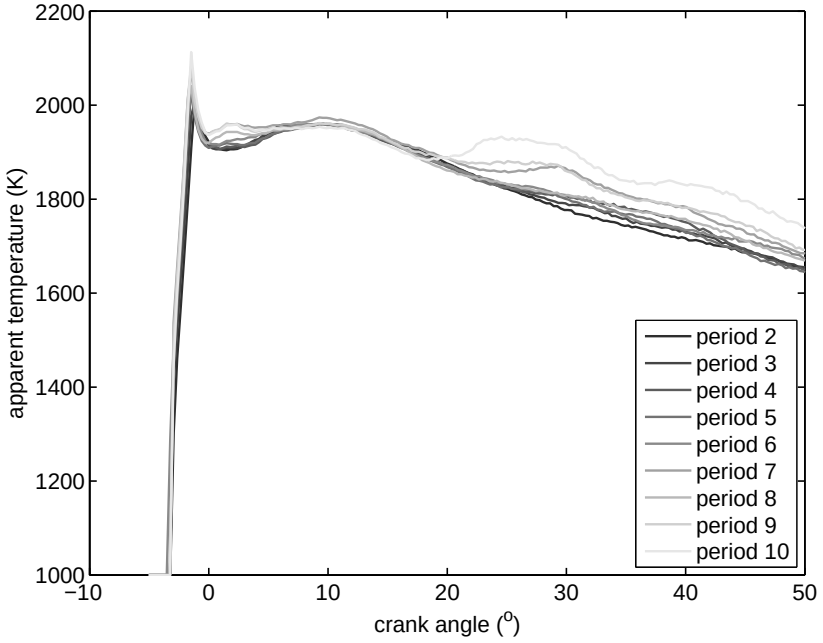

Figure 5.23: Apparent flame temperature results as a function of crank angle for condition 4.

flame temperatures are around 2239 K and 2299 K respectively whereas for condition 3 and 4, the peak apparent flame temperatures are lower at 2061 K and 2113 K for respectively. This effect of decreasing peak apparent flame temperature with increasing engine load is consistent with findings elsewhere [23, 25, 50]. As load increases, the higher soot concentration increases the amount of radiation loss from the flame, which can result in a reduction of the apparent flame temperature.

It is recognised that the temperature of the radiating soot particles will be lower than the temperature at which combustion is actually taking place. Matsui et al. [25] has demonstrated that the temperature of the soot particles will always be lower than the temperature of the surrounding gas by solving an energy equation involving a soot particle and surrounding gas. Schubert et al. [51] introduce a model in which the temperature of the radiation from the soot particles, T_{rad} is related to the enveloping burned gas temperature and the adiabatic flame temperature according to

$$T_{rad} = 0.9 \left[\left(1 - \frac{m_{burn}}{m_{cyc}} \right) T_{f,ad} + \frac{m_{burn}}{m_{cyc}} T_{burn} \right] \tag{5.4}$$

where m_{burn} is the mass of fuel burned, m_{cyc} is the total fuel and air mass in the cylinder, T_{burn} is burned gas temperature and $T_{f,ad}$ is the adiabatic flame temperature. Here, the ratio of $\frac{m_{burn}}{m_{cyc}}$ which is always less than unity, resulting in T_{rad} always being lower than $T_{f,ad}$.

5.5 KL Values

The timing of the rise of the KL values (Figures 5.24 to 5.27) appears to lag the temperature results. The apparent temperature results tend to rise more quickly because these values are not dependent on cloud thickness or field of view coverage by the cloud. Obviously some emissions need to be coupled into the quartz

rod window, but provided even a small signal is registered on all three wavelength channels, a high temperature can be deduced since it is the *relative* magnitude of the signals which dictates the temperature. In contrast, the KL value is the product of a nondimensional soot concentration parameter K, and the optical path length within the soot cloud L and both of these parameters will be affected by the development and movement of the soot cloud relative to the field of view within the combustion chamber.

The non-dimensional soot concentration parameter K is expected to scale with the equivalence ratio ϕ and is also expected to be dependent on configuration parameters such as the compression ratio, combustion chamber shape, and the injection arrangement. If equivalence ratio and configuration similarity could be maintained between engines of different scales, then the optical path length within the soot cloud L should scale with engine size. Values for the peak KL values obtained in the present work with the an engine displacement of 0.21 L range between about 0.3 and 1.6 μm, Table 5.1 (see also Figures 5.24 to 5.27). Peak values obtained by other workers [23, 24] vary between 1.3 and 2.9 μm for a similar range of equivalence ratios, but for a significantly larger engine displacement of 2.33 L. Thus, the present results are on average, smaller in magnitude than those obtained by other workers, but this is reasonable given the smaller size of the present engine.

Table 5.1: Summary of KL and radiation heat flux results.

Condition	ϕ	KL_{max} (μm)	KL_{mean} (μm)	q_{max} (MW/m^2)	q_{mean} (MW/m^2)
1	0.303	0.623	0.035	0.271	0.0151
2	0.325	0.2783	0.032	0.138	0.0141
3	0.493	1.628	0.203	0.381	0.0479
4	0.552	0.671	0.071	0.192	0.0170

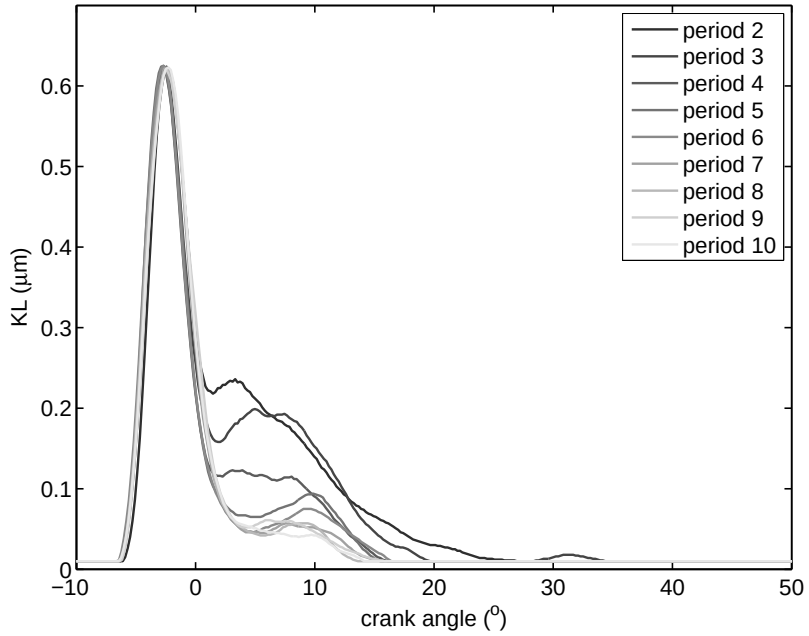

Figure 5.24: KL results as a function of crank angle for condition 1.

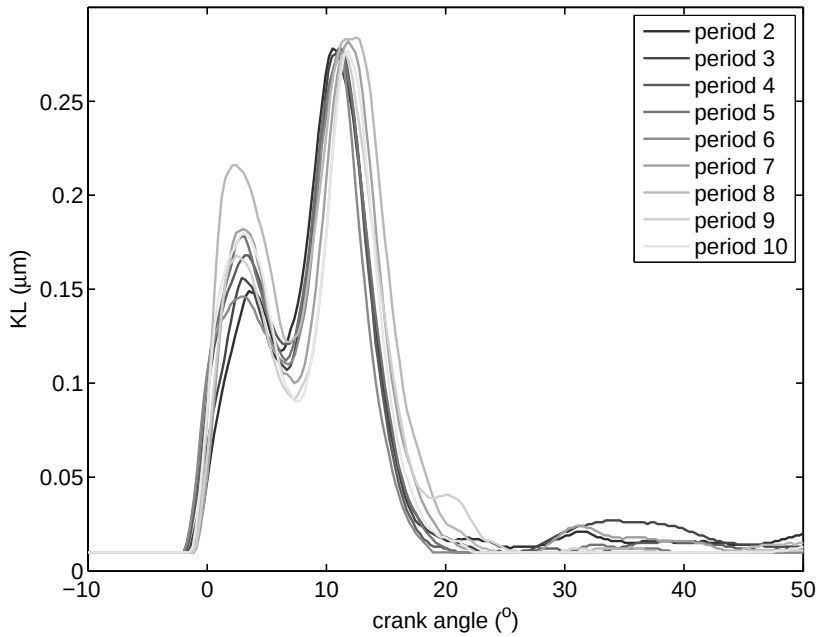

Figure 5.25: KL results as a function of crank angle for condition 2.

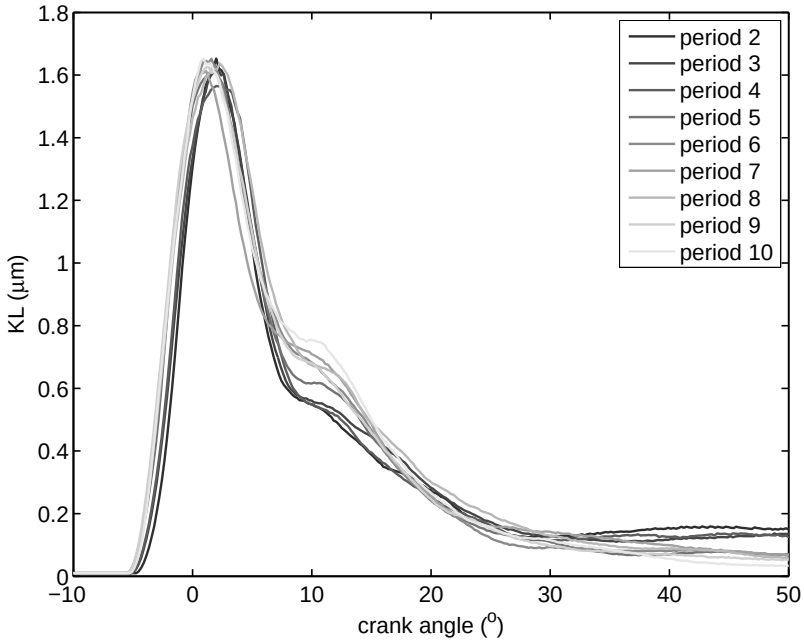

Figure 5.26: KL results as a function of crank angle for condition 3.

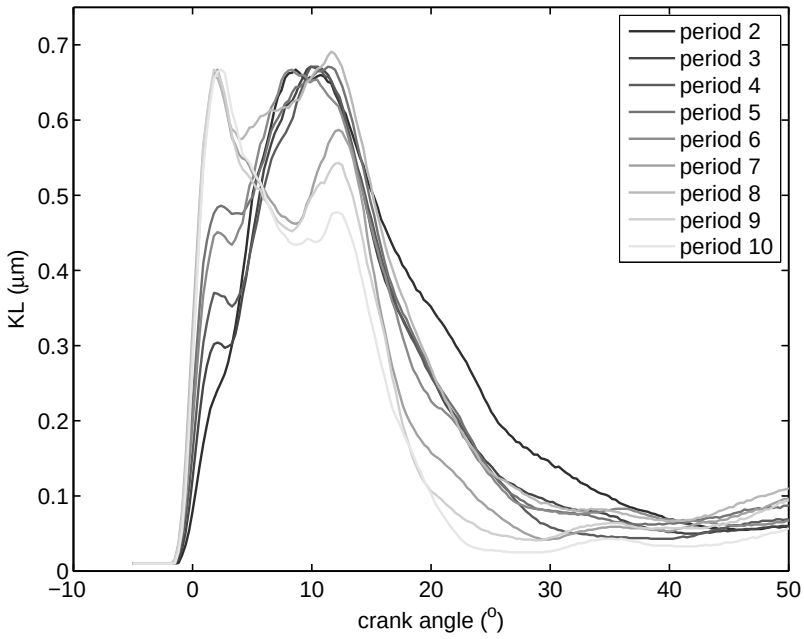

Figure 5.27: KL results as a function of crank angle for condition 4.

5.6 Radiation Heat Flux

Results of instantaneous radiation heat flux which have been produced by numerical integration of Equation (2.7) using the instantaneous values of apparent temperature and KL, are illustrated in Figure 5.28 to 5.31. It is evident that the results are reflective of KL values as the apparent temperature remains largely constant CA in all the conditions. This means that soot cloud density relative to the field of view is the main influence on the form of the radiation heat flux, during diesel engine combustion and expansion process.

Table 5.1 presents a summary of the two-colour method results in terms of the equivalence ratio, maximum KL value, mean KL value (per cycle), maximum radiation heat flux and mean radiation heat flux (per cycle). The maximum radiation heat flux, q_{max} values are in the range of 0.14 to 0.38 MW/m^2. This range is relatively low compared to previous researchers who employed larger displacement engines than used in the present study. The peak radiation heat flux values from other works with their respective engine displacements include:

- Qiong et al. [9]: around 0.7 MW/m^2 for a 0.86 L engine;
- Flynn [22]: between 0.7 and 1.5 MW/m^2 for a 1.18 L engine;
- Jackson [3]: around 1.4 MW/m^2 for a 2.0 L engine;
- Yan [23]: between 1.3 and 1.4 MW/m^2 for a 2.33 L engine; and
- Struwe [24] between 0.8 and 1.9 MW/m^2 for a 2.33 L engine.

The fact that the heat flux results from the present work are at the lower end of the range while using the smallest engine size (0.21 L) indicates that there is strong influence of engine size on the radiation heat flux values. The range of equivalence ratios employed in this experiment is consistent with the range of values used by other workers in the area of radiation heat transfer measurements. The values of

q_{mean} of this study when compared to other previous works also show the same trend of engine size effect as observed with the q_{max} values. These trends indicate that the volume of the soot cloud produced during combustion and expansion process is a significant contributor to the radiation heat flux. If radiation heat flux was only a soot cloud surface radiation effect, the peak radiation heat flux would be expected to remain largely constant irrespective of the engine size.

Previous radiation studies have focused on larger engines possibly due to easier design and installation of the probe in the limited space of the engine head. Smaller engine heads pose restrictions on size and flexibility in probe design and positioning. It also appears that engine size was not previously viewed as a factor of influence in radiation heat transfer measurements.

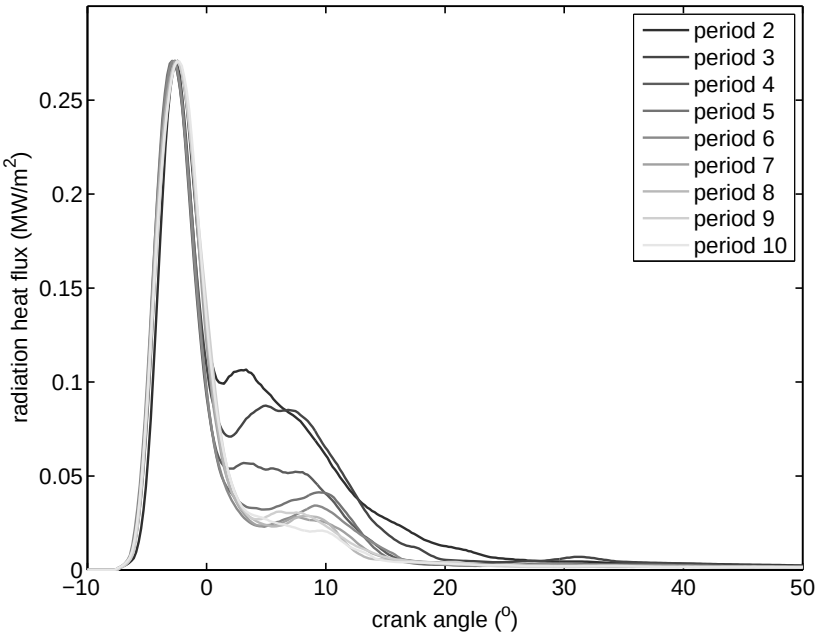

Figure 5.28: Radiation heat flux as a function of crank angle for condition 1.

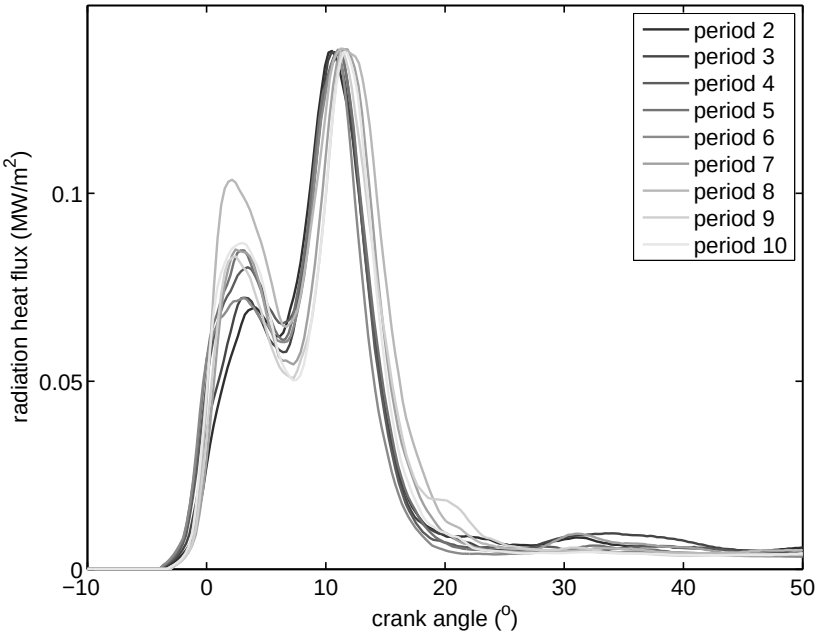

Figure 5.29: Radiation heat flux as a function of crank angle for condition 2.

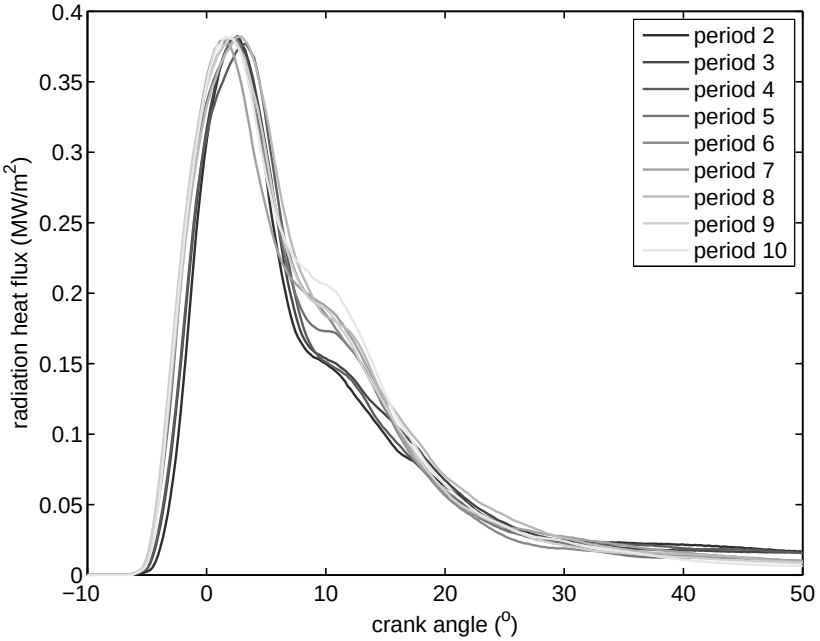

Figure 5.30: Radiation heat flux as a function of crank angle for condition 3.

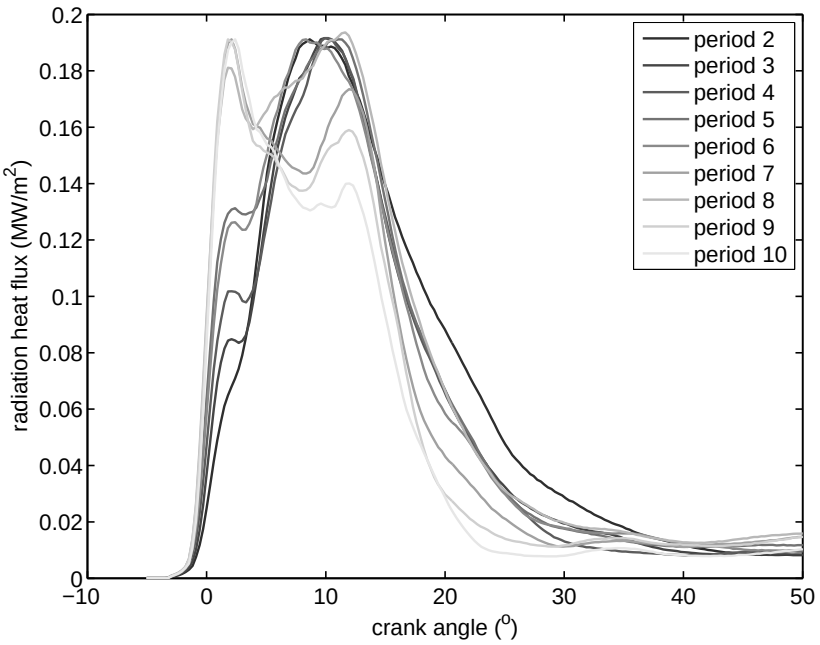

Figure 5.31: Radiation heat flux as a function of crank angle for condition 4.

5.7 Conclusion

In this study, new radiation heat flux measurements have been obtained from a small diesel engine using the two-colour method. The problem of signal attenuation by probe sooting was successfully compensated by adopting an approach based on post-run calibration of the probe in its sooted state. The engine used in the current work is substantially smaller than other engines from which radiation heat flux data has been reported in the open literature. The next smallest engine used for radiation heat flux measurements in the available literature was 0.86 L which is 3 times the size of the engine used in this study. It is expected that the current results provide valuable information about the effect of combustion chamber size in radiation heat flux scaling. Apparent temperatures deduced from the two-colour method, in this study are consistent with the results from other published works [23, 7, 22, 25] in terms of magnitude and the trend of decreasing peak values with increasing load. KL values obtained in this study are in the range between 0.3 and 1.6 μm, which is lower in comparison to other researchers

[23, 7] who registered values between 1.3 and 2.9 μm but with substantially larger engines (2.33 L). The radiation heat flux data obtained in the present work are at the lower end in comparison with other works [23, 24, 22, 3, 9]. The peak radiation values for this work are in the range of 0.14 to 0.38 MW/m^2 which is about two times lower than results obtained with the nearest engine size in available literature review. These results point to the significance of soot cloud volume in the radiation heat flux losses in comparison to the flame temperature, which appears to be similar for the range of engines for which data is available.

Chapter 6

Results and Discussion: Convective Heat Flux

6.1 Introduction

Convective heat flux measurements were taken in order to obtain a quantitative relationship between radiation heat flux and total engine heat transfer. Having additional instantaneous convective heat flux data to complement radiation heat transfer data with similar probe orientation and engine set-up contributes valuable information on the significance of radiation heat transfer to the overall engine heat transfer losses. In the case of small engines where the surface area to volume ratio is high, a quantitative relationship between radiation heat flux and the total heat transfer data is valuable especially in engine scaling efforts.

This chapter presents the results of the convective heat flux measurements on the engine arrangement as described in Chapter 4. Convective heat flux results have been produced from the measured temperature history using an analysis based on an impulse response processing technique. The background information on the impulse response processing technique is described together with an approach to

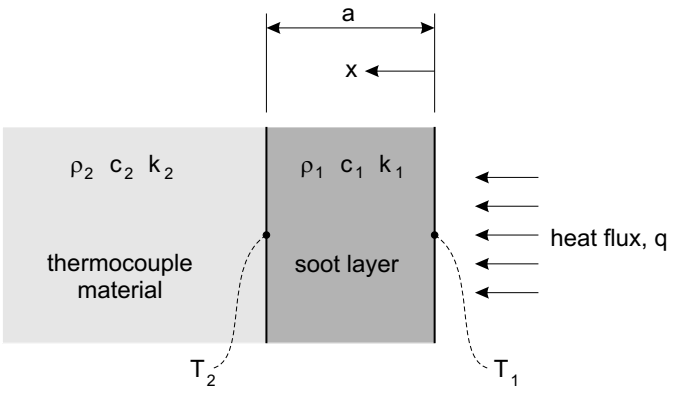

Figure 6.1: Heat flux gauge with soot layer arrangement considered for the present analysis.

deduce soot thickness to obtain the instantaneous heat flux at the edge of soot layer, which is the interface with the hot gases in the cylinder. Comparison with selected published works is made to confirm the consistency of the data.

6.2 Impulse Response Processing Technique

The analysis of transient heat flux in the presence of a soot layer proceeds via the multi-layer heat flux gauge analysis presented by [52] and the impulse response processing techniques introduced by [46].

Consider the situation where a thermocouple substrate has a soot layer of thickness a deposited at its surface as depicted in Figure 6.1. The relevant thermal properties are the density ρ, specific heat c, and conductivity k for the soot (denoted with subscript 1) and thermocouple material (denoted with subscript 2). Convenient groupings of these parameters which are used in the subsequent analysis are the thermal product or thermal effusivity $\sqrt{\rho ck}$ and the thermal diffusivity $\alpha = k/(\rho c)$. Assumed values for the soot and thermocouple materials are listed in Table 6.1.

Table 6.1: Thermal properties of the soot and thermocouple materials

Material	ρ (kg/m^3)	c (J/kgK)	k (W/m.K)
thermocouple	8822	420	20.2
soot	1000	700	0.2

For a step input of heat flux at the surface of the soot layer, the temperature at the surface of the soot will be given by [52]

$$T_1(t) = \frac{2}{\sqrt{\rho_1 c_1 k_1}} \left[\sqrt{\frac{t}{\pi}} + \sum_{n=1}^{\infty} 2A^n \left[\sqrt{\frac{t}{\pi}} \exp\left(-\frac{k_s^2}{4t}\right) - \frac{k_s}{2} \operatorname{erfc}\left(\frac{k_s}{2\sqrt{t}}\right) \right] \right] \tag{6.1}$$

where

$$A = \frac{\sqrt{\rho_1 c_1 k_1} - \sqrt{\rho_2 c_2 k_2}}{\sqrt{\rho_1 c_1 k_1} + \sqrt{\rho_2 c_2 k_2}} \tag{6.2}$$

and

$$k_s = \frac{2na}{\sqrt{\alpha_1}} \tag{6.3}$$

The temperature at the interface between the soot layer and the thermocouple gauge $x = a$ will be given by

$$T_2(t) = \frac{2(1+A)}{\sqrt{\rho_1 c_1 k_1}} \left[\sum_{n=1}^{\infty} A^n \left[\sqrt{\frac{t}{\pi}} \exp\left(-\frac{k_a^2}{4t}\right) - \frac{k_a}{2} \operatorname{erfc}\left(\frac{k_a}{2\sqrt{t}}\right) \right] \right] \tag{6.4}$$

where

$$k_a = \frac{(2n+1)a}{\sqrt{\alpha_1}} \tag{6.5}$$

Results from Equation (6.1) and (6.4) are presented in Figure 6.2 for the case of a soot layer which is 50 μm thick. The temperature at the surface of the soot layer rises immediately the step in heat flux is applied at the surface (at time $t = 0$ on the scale in Figure 6.2), whereas the temperature at the interface between the soot and the thermocouple *appears* to rise after a short delay denoted as t_{shift} in Figure 6.2. The temperature rise at the interface certainly occurs more slowly than at the surface of the soot layer, but a definitive value for the delay between the temperature rise at the soot surface and thermocouple interface cannot be precisely identified from the governing equations. For the present work, different values of t_{shift} are investigated according to the definition

$$t_{shift} = C\frac{a^2}{\alpha_1} \tag{6.6}$$

where C is defined as the time shift scaling factor.

Using the approach outlined by Oldfield [46], the modelled temperature rise at the interface between the soot and the thermocouple T_2 (Equation (6.4)) and the driving heat flux step at the surface of the soot are used as the basis functions for designing an impulse response filter to transfer from the measured thermocouple temperature history to the heat flux at the soot surface with a time shift according to Equation (6.6)).

Testing of the impulse response filtering method proceeded by examining the capacity to recover an input step in the heat flux. Illustrative results are presented in Figure 6.3 for a soot layer thickness of 50 μm and a time shift scaling factor of $C = 0.1$. A delay in the rise of the apparent heat flux, a finite rise time and

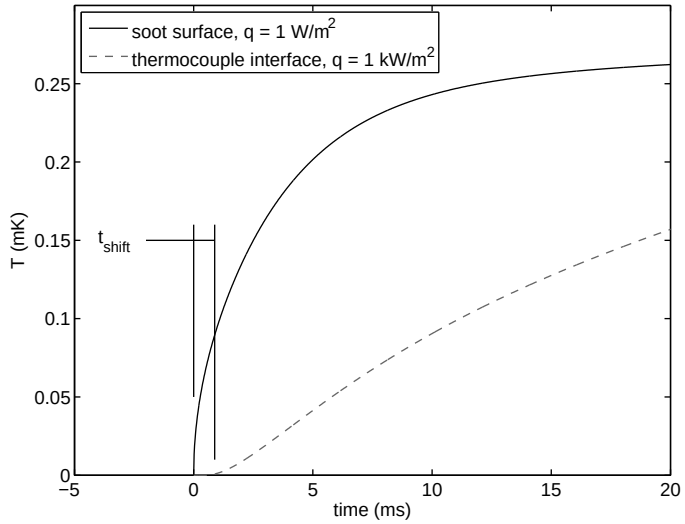

Figure 6.2: Illustration of temperature variations at the soot surface and the soot interface with thermocouple for heat flux steps imposed at the soot surface. Soot layer thickness $a = 50\,\mu$m. Note the different magnitudes for applied heat flux step at the surface that have been used to more clearly display the two temperature histories on the same graph.

an overshoot in the inferred heat flux are all clearly apparent features for these conditions. The delay in the rise of the apparent signal is reduced by the virtue of the time shift, and in the present case the shifted result is approximately centred on the correct time, $t = 0$.

Rise time results for the period between 10 % and 90 % of the true heat flux step and overshoot errors are presented in Figures 6.4 and 6.5 as a function of the time shift scaling factor for soot layer thicknesses between 20 and 200 μm. The rise time increases and the overshoot error decreases with increases in the time shift for any particular thickness of the soot layer. The overshoot error is a weak function of the soot layer thickness within the tested range. Overshoots of less than 10 % (a value of 0.1 on the scale in Figure 6.5) will be registered for time shift scaling factors larger than 0.06. For a 50 μm soot layer, rise times of less than 0.5 ms will be registered using the present impulse response filtering technique provided the time shift scaling factor is smaller than 0.06. In the present work, it appears that

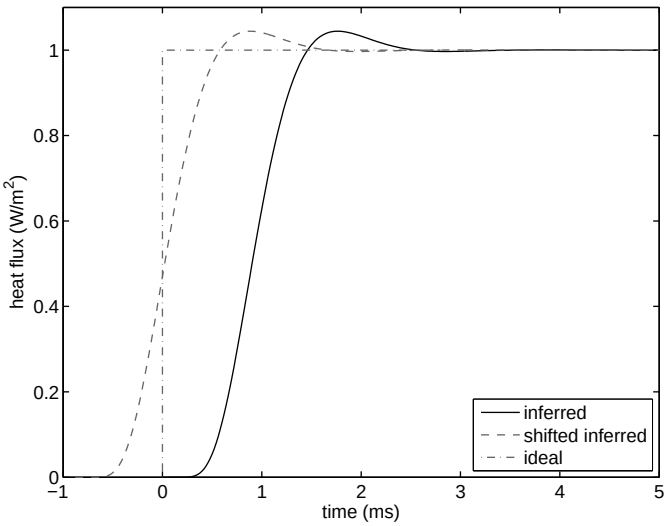

Figure 6.3: Illustration of the inferred heat flux for the case of $a = 50\,\mu$m thick soot layer and a time shift scaling factor of $C = 0.1$.

the effective soot layer thicknesses are substantially smaller than $50\,\mu$m – values closer to $20\,\mu$m are indicated (see Section 6.3. For such thicknesses, rise times of less than 0.1 ms can be achieved for time shift scaling factors of around 0.1 or less.

Additional investigations into the performance of the impulse response filtering technique were performed for cases of periodic heat flux signals. For this work, an additional impulse response filter was used to convert from a periodic heat flux at the surface of the soot to a temperature result at the interface of the soot and thermocouple layers. The temperature deduced in this manner was then used as the input to the impulse response filter as applied in the heat flux step work outlined previously. The difference between the inferred heat flux and the true periodic heat flux was used to define an RMS error – results from which are plotted in Figure 6.6 as a function of the time shift scaling factor for a range of different soot layer thicknesses. Results demonstrate that RMS errors smaller than 0.5 % (a value of 0.005 on the scale in Figure 6.6 can be achieved for soot layer thicknesses less than $50\,\mu$m for time shift scaling factors $C \leq 0.1$).

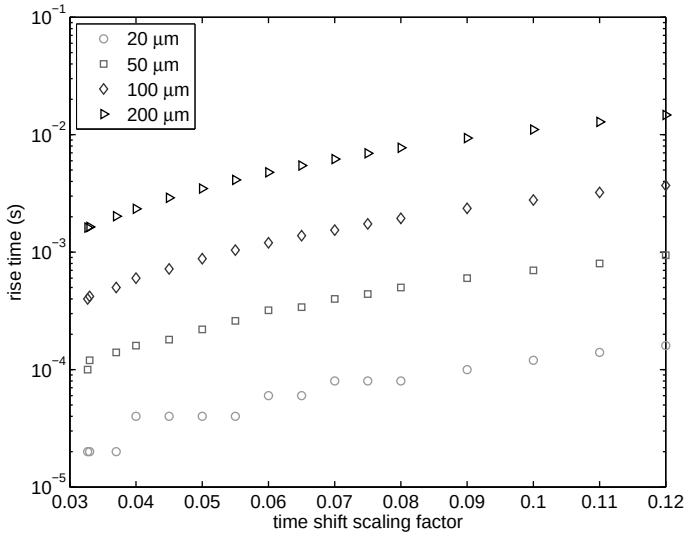

Figure 6.4: Rise times for the inferred heat flux results for a step in surface heat flux for a range of soot layer thicknesses between 20 and 200 μm as a function of the time shift scaling factor (as defined in Equation (6.6)).

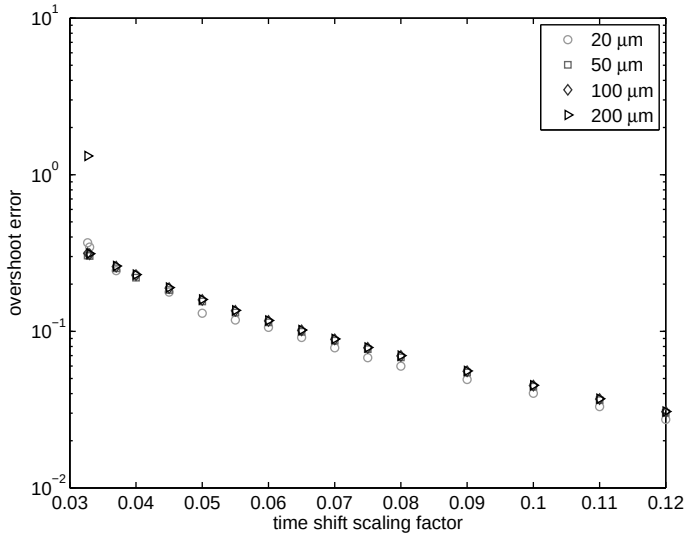

Figure 6.5: Overshoot error for the inferred heat flux results for a step in surface heat flux and for a range of soot layer thicknesses between 20 and 200 μm as a function of the time shift scaling factor (as defined in Equation (6.6)).

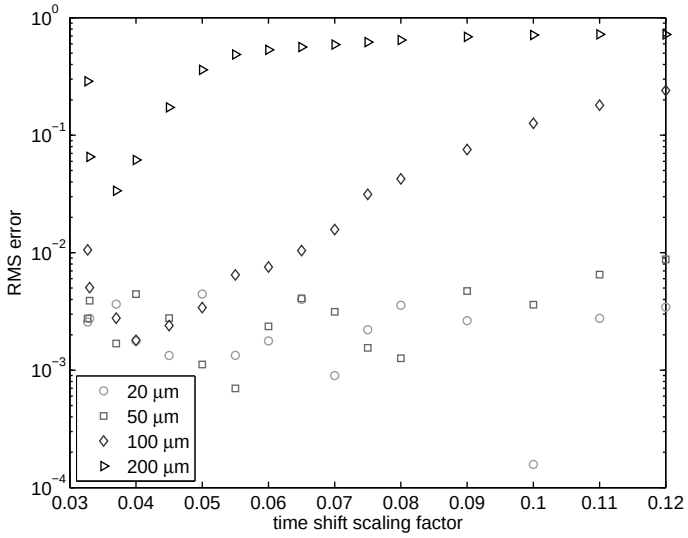

Figure 6.6: RMS error in the inferred heat flux for a periodic surface heat flux at 100 Hz and for a range of soot layer thicknesses between 20 and 200 μm as a function of the time shift scaling factor (as defined in Equation (6.6)).

6.3 Deduction of Soot Layer Thickness

As described in Section 6.2, impulse response processing techniques can be applied to infer the heat flux at the surface of the soot layer based on the measured thermocouple temperature history with a time shift according to Equation (6.6). However, the soot layer thickness a has to be determined. For this work, trial values for thickness a have been used and the inferred heat flux values have been compared with heat flux results obtained under motored conditions in the absence of any soot layer. An illustration of the approach is shown in Figure 6.7. Here, the soot layer thickness used in the impulse response processing technique was tuned until the inferred heat flux of the fired case closely resembles the heat flux in the motored case for CA values before the start of injection which was around 14° BTDC. A soot layer thickness of 17 μm was deduced in this case. In applying this approach, it is assumed that no detectable soot deposits occur during the injection and combustion phases, the process is one of a gradual build-up of soot over many cycles.

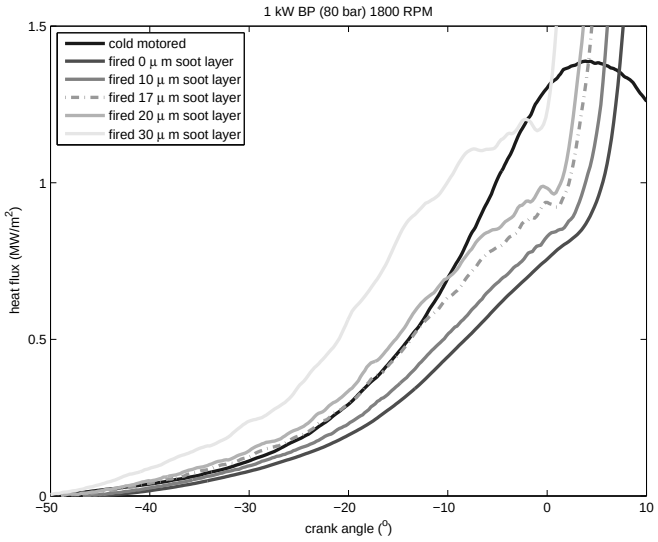

Figure 6.7: Illustration of method used to deduce effective soot layer thickness for period 1, condition 3. Heat flux produced with 17 μm soot layer thickness matches the heat flux during cold motored at compression process before the start of injection.

6.4 Convective Heat Flux Results

Results presented here consist of ensemble-averaged data of the pressure and convective heat flux taken from 30 consecutive cycles for condition 1, 3 and 4 for period 1, period 2 and period 3. Results from condition 2 have been excluded in view of unreliable data due to failure in adhesive materials used in thermocouple probe.

Figures 6.8 to 6.10 display the heat flux results from period 1 to period 3 for condition 1, 3 and 4. Heat flux values for different periods are shown to be relatively constant for all conditions, although in condition 1, the peak values at period 3 is lower than in period 1 and period 2. For condition 1, the average peak value for all three periods is 6.72 $\mathrm{MW/m^2}$ with a standard deviation, σ = 0.70 $\mathrm{MW/m^2}$. The averaged peak values for all three periods for condition 3 is 5.62 $\mathrm{MW/m^2}$ with a standard deviation, $\sigma = 0.34\,\mathrm{MW/m^2}$. For Condition 4, the average peak value for all three periods is 8.98 $\mathrm{MW/m^2}$ with a standard deviation,

$\sigma = 0.11\,\mathrm{MW/m^2}$.

In terms of the shape and the overall timing of the heat flux, all ensemble-average convective heat flux data displayed excellent agreement across the different acquisition periods. The fact that the peak values obtained are relatively consistent and the shapes are maintained for the 3 periods, shows that the technique for deducing soot layer thickness has successfully compensated the effect of sooting on the thermocouple probe, that is otherwise known to cause lagging and reduce the inferred heat flux magnitude relative to the true values.

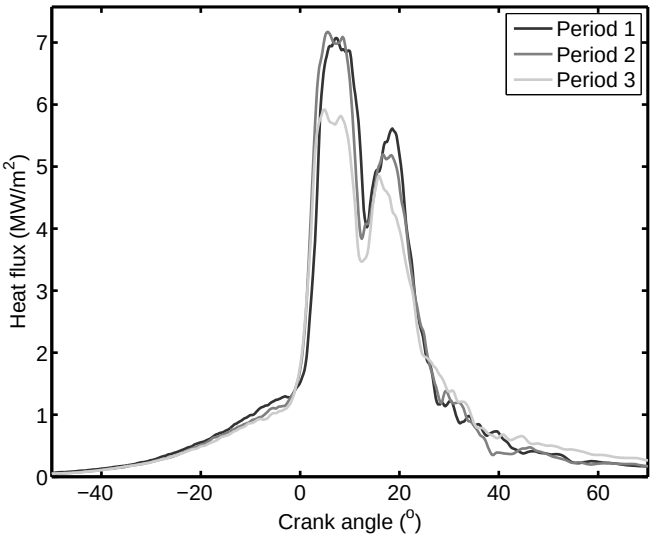

Figure 6.8: Ensemble-averaged heat flux results for condition 1.

6.5 Pressure and Convective Heat Flux

There is very little difference in the pressure histories recorded for all periods between 1 and 5 for all conditions. The standard deviations in the ensemble-averaged peak pressures across these cycles are: 0.0761, 0.0639, 0.0611 MPa for the conditions 1, 3 and 4 respectively.

The results of the ensemble-averaged convective heat flux measurements plotted

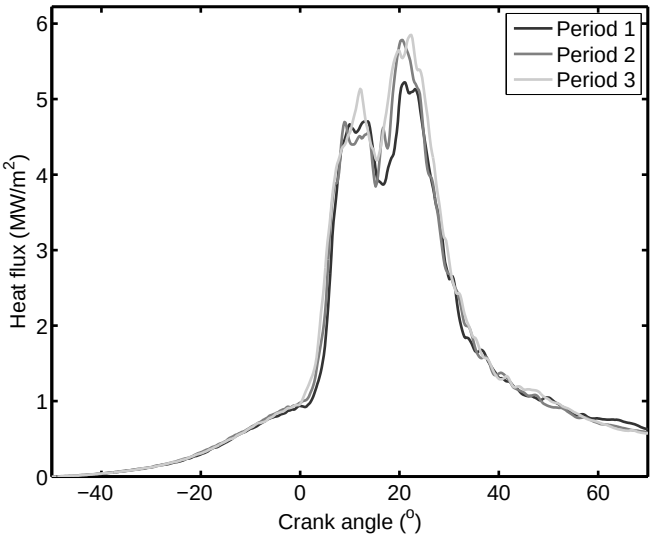

Figure 6.9: Ensemble-averaged heat flux results for condition 3.

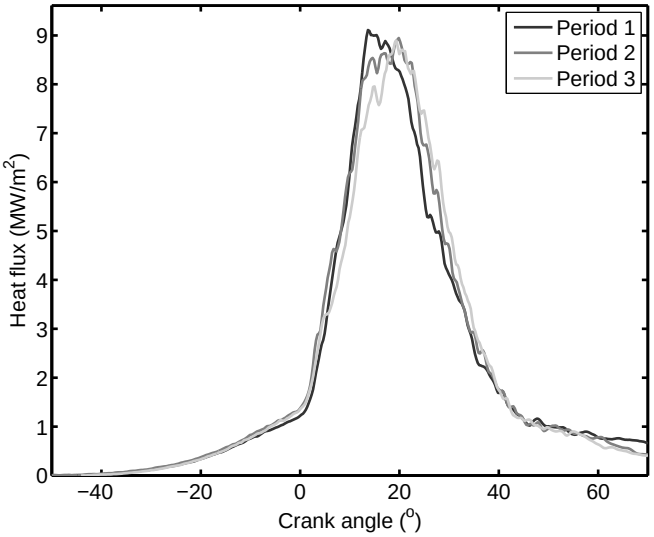

Figure 6.10: Ensemble-averaged heat flux results for condition 4.

with the pressure data during period 2 for condition 1, 3 and 4 are displayed in Figure 6.11, 6.12 and 6.13. It is observed that the ensemble-averaged convective heat flux results show a rapid rise after the start of the combustion induced pressure rise with a CA lag of approximately 3° for condition 1 and 3 and 4° for condition 4. Peak convective heat flux values occur after the peak pressure. For condition 1, there is a relatively small lag but for conditions 3 and 4, the lag is in excess of 10°.

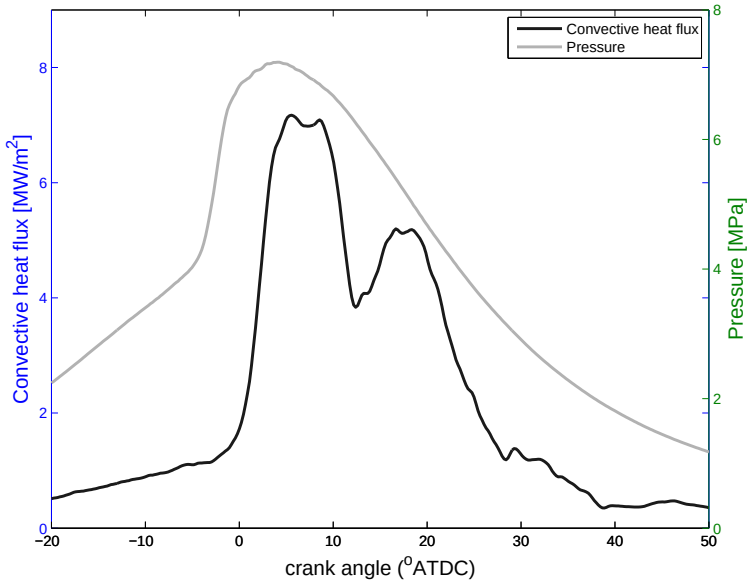

Figure 6.11: Convective heat flux and pressure for condition 1 at period 2.

Table 6.2 presents the result of the deduced soot layer thickness using the approach as described in Section 6.3. There seems to be a relationship between the engine load and the apparent soot layer thickess: the thickness seems to be decreasing with the engine load (which was lowest for condition 1 and highest for condition 4).

Across the acquisition periods, the soot layer thickness seems to be constant for the lower load cases (condition 1 and condition 3) while for the high load case of condition 4, the deduced thickness results exhibit gradual decrease from 16 μm to 12 μm for period 1 to 3.

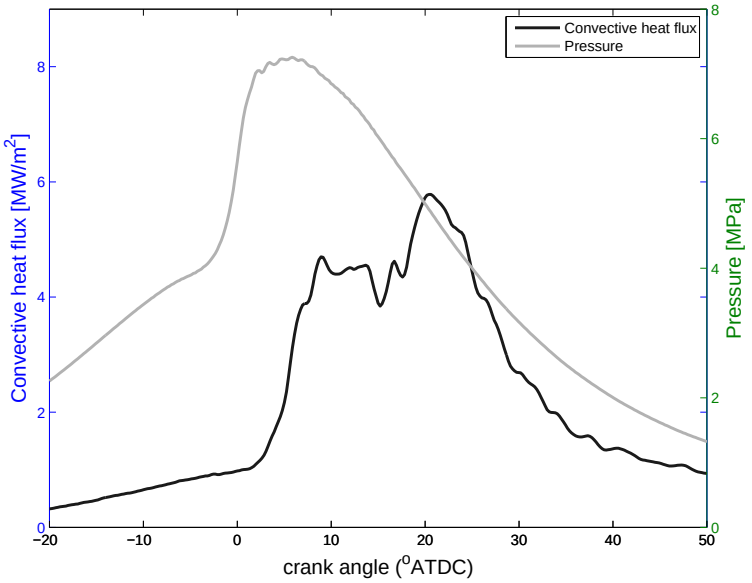

Figure 6.12: Convective heat flux and pressure for condition 3 at period 2.

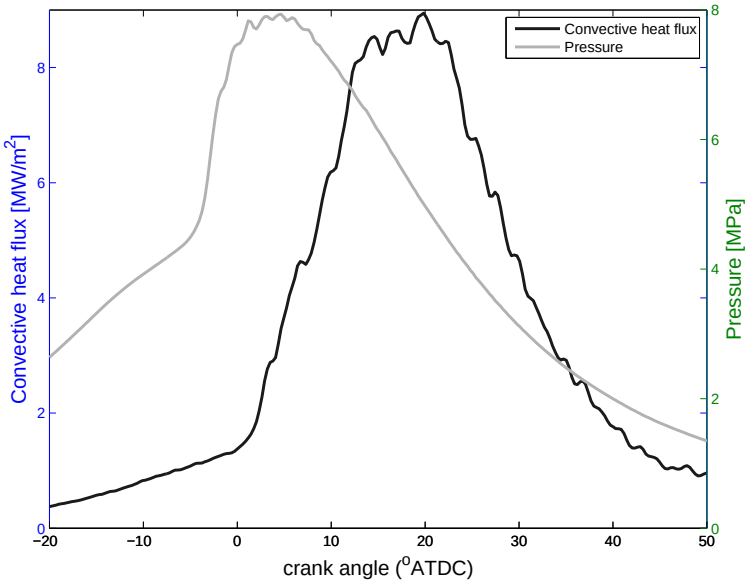

Figure 6.13: Convective heat flux and pressure for condition 4 at period 2.

Table 6.2: Results of soot layer thickness deduction

Condition	Soot thickness Period 1 (μm)	Soot thickness Period 2 (μm)	Soot thickness Period 3 (μm)
1	20	20	20
3	17	17	17
4	16	14	12

Table 6.3 compares a range of peak convective heat values and information related to different engines and operating conditions of this study and other published works. The range of peak values of 6.7 - 8.95 MW/m^2 obtained in this study, although on the higher side of the overall range, is in the same range as that of Jackson [3] (6.5 - 9 MW/m^2). The high peak convection values obtained in the present work may be connected with the high engine compression ratio used which is 19.9 as this is the highest value within the works shown in Table 6.3. Higher intensity turbulent fluctuations are expected at higher compression ratio and hence higher convective heat flux may result. Another factor that may contribute to the difference of heat flux values is the different location of the probe. High nonuniformity of temperature inside diesel engine combustion chamber can occur and strong variations in the spatial distribution of in-cylinder heat flux have also been previously observed.

6.6 Comparison with Radiation

Radiation heat flux measurements were obtained using the same experimental configurations and operating conditions as reported in Chapter 5 and the results are used to compare with the convective data. Ratios of the maximum values and integrated (cycle-averaged) values for the radiation and convective heat flux

Table 6.3: Selected information on previous experiments reporting peak convective heat flux values.

Researcher	Engine Description	Operating condition	Peak Convective Heat Flux Value (MW/m^2)
Present work, 2012	0.211 L air-cooled DI engine, compression ratio = 19.9, bore size = 0.07 m	1800 RPM, 2500 RPM 1 kW - 2.1 kW IP	6.7 - 8.95
Annand & Ma, 1970 [26]	0.553 L, air-cooled DI engine single cyl., compression ratio = 14.2, bore size = 0.08 m	1200 RPM, 1500 RPM, 1800 RPM FA ratio = 0.026 -0.042	1.6
Dent & Suliaman, 1977 [27]	0.86 L per cylinder, air-cooled, 3 cyl. DI engine, compression ratio = 15.1, bore size = 0.102 m	600 RPM -2000 RPM No load, 50% full load and 80 % full load	2.2 - 4.3
Jackson, 1990 [3]	2.0 L engine, water-cooled DI engine compression ratio = 13.5, bore size = 0.13 m	1000 RPM, 1300 RPM, 2050 RPM 25%, 100% of full load	6.5 - 9
Rakoupolous, 1999 [28]	0.477 L air-cooled DI engine single cyl. compression ratio = 18, bore size = 0.086 m	1500 RPM,1800 RPM,2000 RPM,2500 RPM 40% of full load	2.8

Table 6.4: Ratios of radiation heat flux to convective heat flux.

Condition	Ratio of Maximum Values	Ratio of Integrated Values
1	0.038	0.013
3	0.066	0.027
4	0.021	0.013

results are presented in Table 6.4. The results for condition 2 are not available since the convective results at this condition were deemed unreliable due to failure of adhesive material used on the probe. The range of integrated radiation to convective ratios registered of 1.3 - 2.7 % is somewhat lower than other previous researchers: Flynn [22] for 1.17 L engine (bore = 0.114 m), 13-25 %; Yan [23] for a 2.33 L engine (bore = 0.139 m), 11 %; Qiong [9] for a 0.86 L engine (bore = 0.1 m), 11-17 %. The lower ratio range obtained in this work arises primarily because of the relatively low values of radiation heat flux (Chapter 5) but the relatively high values of convective heat flux also make a contribution.

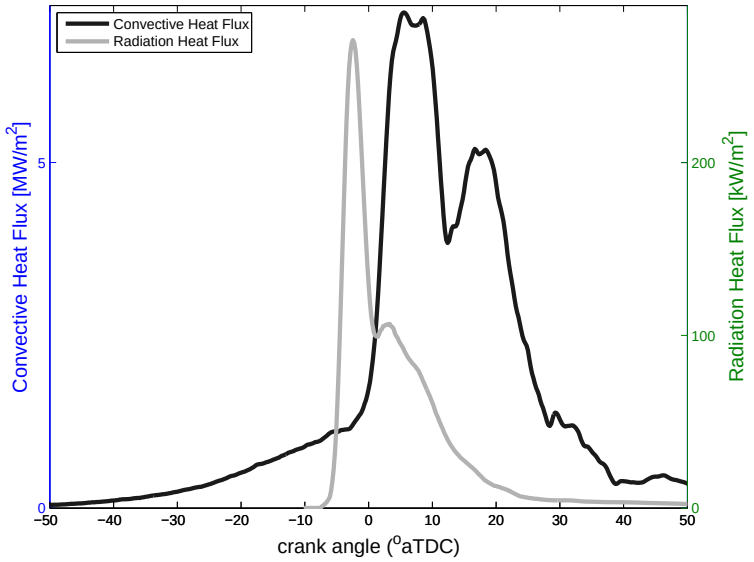

Figure 6.14: Convective and radiation heat flux for condition 1.

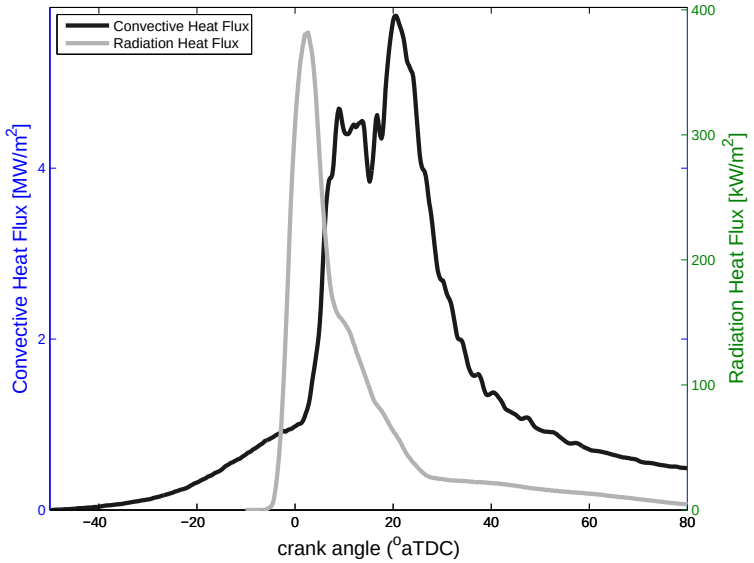

Figure 6.15: Convective and radiation heat flux for condition 3.

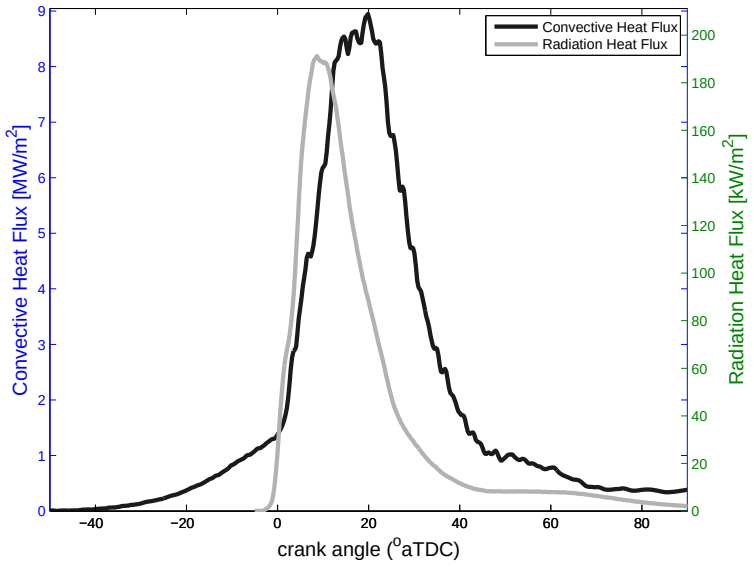

Figure 6.16: Convective and radiation heat flux for condition 4.

Figure 6.14 to 6.16 illustrate the results of ensemble-averaged instantaneous convective heat flux and the corresponding radiation heat flux obtained from period 2 for both sets of data. Period 2 corresponds to 70-80 s after the start of engine firing in the radiation work, but 90-100 s in the convective work. Although the actual time of data gathering for the convective heat flux test was different from that of the radiation test, the comparison is reasonable as both the radiation and the convective heat flux results obtained for different periods have been determined to be fairly constant.

From Figures 6.14 to 6.16 it is evident that the peak radiation values occur before the peak of the convective heat flux. Obviously there are different mechanisms driving the heat transfer in each case. For high convective heat flux, high gas temperature and/or strong turbulence in the immediate vicinity of the probe is required whereas for high radiation heat flux, high soot concentration (and high temperatures) within the probe field of view is required.

The radiation heat flux only rises after the injection of fuel and falls earlier than convective heat flux and this points to the narrow CA phase of soot formation

and soot oxidation in the diesel engine cycle.

6.7 Conclusion

The approach of deducing the soot layer thickness based on tuning of results during compression to match motoring results with a soot-free probe appears to have been effective. The peak convective heat flux values obtained from the 0.21 L engine for condition 1, 3 and 4 are in the same range of peak values as published by Jackson [3]. The present work has produced the smallest values for the ratio of radiation heat flux to convective heat flux in comparison with other works [21, 29, 22, 27, 23, 3, 9] in terms of both peak and time-averaged values. It is suggested that this result reflects the significant influence of engine size on radiation heat flux.

Chapter 7

Results and Discussion: Radiation Heat Transfer Scaling

7.1 Introduction

This chapter provides details of a radiation heat flux scaling analysis performed using data from this study and from other works, providing data from a range of engine sizes. The chapter proceeds with the introduction of some radiation heat loss scaling theory, details on the data sources, a description of the zero-dimensional thermodynamic scaling simulation and some discussion on the results.

7.2 Radiation Heat Loss Scaling Theory

The relative significance of convective and radiative components of in-cylinder heat transfer can be expected to change with engine scale. Consider first the convective component of the in-cylinder heat transfer. For the purpose of this

discussion, the in-cylinder Nusselt number is defined as

$$\mathrm{Nu} = \frac{h\,b}{k} \tag{7.1}$$

where h is an in-cylinder convective heat transfer coefficient, b is the engine bore, and k is some effective thermal conductivity.

Likewise, the in-cylinder Reynolds number is defined as

$$\mathrm{Re} = \frac{\rho \overline{U}_p b}{\mu} \tag{7.2}$$

where ρ is some average density of the gases, $\overline{U}_p$ is the average piston speed, and μ is some effective dynamic viscosity.

Most correlations for the convective heat transfer coefficient in the cylinder give the variation of Nusselt number in the form, as shown below [20]:

$$\mathrm{Nu} \sim \mathrm{Re}^n \tag{7.3}$$

where n is an index, generally taken as close to 0.8 [20], reflecting the turbulent characteristics of engine flows. The heat transfer coefficient therefore varies according to

$$h \sim \frac{k\,\rho^n}{\mu^n}\,\overline{U}_p^{\,n}\,b^{n-1} \tag{7.4}$$

If engine charging and the compression ratio remain the same for different engine scales, then the unburned gas density and effective transport properties will largely remain the same at the different engine scales. For this statement to hold, heat transfer effects must be of secondary significance. If the combustion pro-

cess also remains similar for the different scales, then the gas-to-wall temperature differences which drive the convective heat transfer will also be similar at the different scales. Under these conditions, the convective heat flux (W/m^2) scales as

$$q_c \sim h \sim \overline{U}_p^n \, b^{n-1} \tag{7.5}$$

To achieve combustion similarity at different engine scales in either premixed or diffusive combustion modes, the turbulent mixing characteristics within the cylinder will need to be similar. Thus, Reynolds number similarity needs to be maintained and hence, $\overline{U}_p$ will need to be constant across the different scales. The mean piston speed varies as

$$\overline{U}_p \sim b\,\omega \tag{7.6}$$

and hence the angular velocity of the engine ω should increase in direct proportion to the decrease of the engine scale b and through such scaling, the dynamic stresses on geometrically similar engines will remain essentially constant across the different scales. Under such conditions, the convective heat flux to the cylinder should vary with engine size according to

$$q_c \sim b^{n-1} \tag{7.7}$$

which indicates that for $n \approx 0.8$, the convective heat flux is not a strong function of engine scale, but it does become increasingly significant for smaller sized engines.

Now consider radiation heat transfer in geometrically similar engines at different scales. Charging and fueling of the engines is assumed to be similar at the different

scales, and the combustion process is likewise assumed to be similar. At some engine conditions, the radiation heat transfer to the cylinder wall is expected to be dominated by radiation from the surface of the flame, but significant contributions to the total radiation heat transfer can also be made from within the flame volume. Therefore, the radiative heat flux (W/m^2) received at the internal walls of the cylinder can be considered as scaling according to

$$q_r \sim b^m \tag{7.8}$$

where m is an index which reflects the flame radiation characteristics: $m \approx 1$ indicates a condition in which radiation to the cylinder walls is dominated by the flame volume (transmissivity of the flame volume is high); $m \approx 0$ indicates a condition in which radiation is received primarily from the surface of the flame (flame transmissivity is low).

Therefore, the relative significance of radiation and convection heat flux should scale according to

$$\frac{q_r}{q_c} \sim b^{1+m-n} \tag{7.9}$$

which indicates that for values $0 \leq m \leq 1$ radiation is expected to make a less significant contribution to the in-cylinder heat flux as the engine size decreases. For moderately large diesel engines, radiation heat transfer represents somewhere between 5 and 40 % of the total in-cylinder heat transfer, depending on the engine load [29, 19, 22, 23, 24]. Supposing the ratio of radiation to total heat flux $q_r/q_t = 0.4$ for an engine bore $b = 140\,\text{mm}$, the relationship given by Equation (7.9) was expressed in terms of the total heat flux ($q_t = q_r + q_c$) as

$$\frac{q_r}{q_t} = \frac{\frac{q_r}{q_c}}{1 + \frac{q_r}{q_c}} \tag{7.10}$$

with results plotted in Figure 7.1. The relative significance of the radiation heat

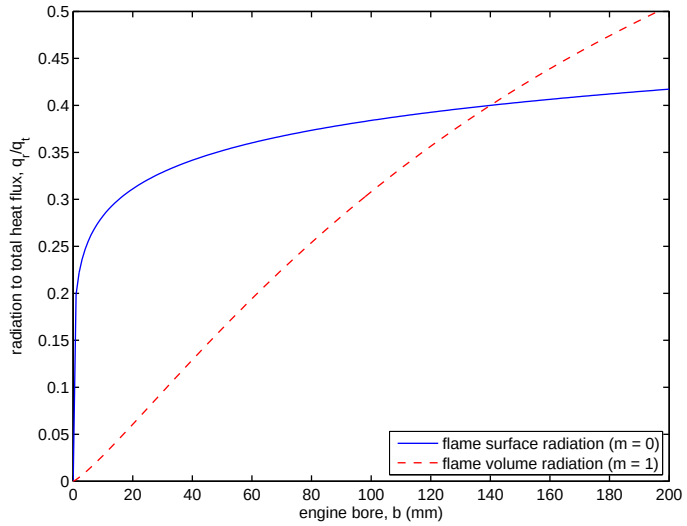

Figure 7.1: Ratio of radiation heat flux to total heat flux as a function of diesel engine size when the radiation is received from the surface of the flame ($m = 0$) and when radiation is received from the flame volume ($m = 1$) for $n = 0.8$.

flux is seen to be strongly dependent on whether the flame radiation is dominated by surface or volume radiation effects. When radiation is received primarily from the surface of the flame (the solid line in figure 7.1), the radiation fraction of the total heat flux decreases by about 8 % in moving from an engine with a bore of 140 mm to an engine with a bore of 70 mm, whereas for radiation received from the flame volume, the corresponding decrease is about 44 %.

7.3 Data Sources

If a fundamental study of radiation heat flux scaling within diesel engines were to be performed, radiation heat flux measurements would be obtained on a range of geometrically similar engines operated under similar charging, fuelling and combustion conditions. However, it is arguably more useful to try and correlate the existing data from a range of different sources.

To determine the relative importance of radiation from the surface and volume

of the diesel flame across different engine scales, data presented by Flynn [22], Yan [23, 8], Jackson [3], Qiong [9] and Struwe [24, 7] have been examined. These works were selected because they provide data from a variety of engine sizes and conditions, and most importantly, they provide other pertinent data such as pressure data or indicated mean effective pressure results. Some of these works also provide crank-resolved KL values which are used in subsequent analysis. Some important engine parameters and experimental conditions of these works are presented in Table 7.1.

Results obtained by these other workers have been supplemented by the new results obtained in the present work. The two-colour method was applied to four different engine operating conditions for two different engine speeds: 1800 RPM and 2500 RPM. The description of the experiments has been explained in Chapter 4, but a summary of operating conditions for these experiments is also presented in Table 7.1.

7.4 Radiation Heat Flux Scaling Correlation

Cycle average radiation heat flux values and instantaneous peak heat flux values for the available engine data have been plotted in Figure 7.2 and 7.3. Cycle average radiation heat flux is defined as

$$\overline{q} = \frac{1}{\tau} \int_0^\tau q(t) dt \tag{7.11}$$

where τ is the time taken for one engine cycle (four strokes) and $q(t)$ is the instantaneous radiation heat flux. In practice, $q(t)$ is an ensemble average taken over several tens of cycles, and in this study about 200 cycles have been used.

In this study, the scaling and correlating parameter is the indicated power per unit piston area, IP/A_p. It is appropriate to adopt this parameter because its

Table 7.1: Experimental parameters for selected instantaneous radiation heat transfer works.

	USQ	Qiong	Flynn	Jackson	Yan	Struwe
Combustion chamber	Swirl	Swirl	Swirl	Swirl	quiescent	quiescent
Bore (mm)	70	100	114.3	130.2	139.7	139.7
Stroke (mm)	55	110	114.3	150	152.4	152.4
Compression Ratio	19.9	18.4	16.7	13.5	13.23	13.1
Displacement (L)	0.211	0.864	1.1728	2.0	2.33	2.33
Field of view (deg)	14	NA	NA	Theoretical hemispherical based on calculated window factor of 0.455.	14	Theoretical hemispherical via extrapolation of Probe 1 and 2 Probe 1 : 57.7% hemispherical Probe 2 : 84.25% hemispherical
Method	Two-colour	Shielded thermocouple	Two-colour	Shielded thermocouple	Two-colour	Two-colour
Rod Window	Quartz, 1.8mm diameter	Sapphire window	2x 0.25 inch diam Quartz	Sapphire, 4mm diameter	sapphire, 6.35mm diameter	lucalox, 6.35mm diameter
Position	On the cylinder head Facing piston bowl	On the cylinder head Facing piston bowl	On the side of cylinder head Facing piston bowl	On the cylinder head Facing piston bowl	On the cylinder head Facing piston bowl	On the cylinder head Facing piston bowl
Special feature	Interpolated Calibration Constant based on post-calibration	Jet purging soot cleaning	Windows can be changed while engine operating where tranmission are maintained above 0.7 .	Calculation of window factor taking account of reflection, refraction and shadowing effect. Radiation Heat Flux measured on few cycles after IMEP established to obtain 'soot free' result	Soot cleaning mechanism - cavity	Soot cleaning mechanism - cavity
Mean Speed (RPM)	1800, 2500	2300	2000	1300	1500, 1900	1200, 1500
Info on Load	IP: 1.0 kW, 1.46 kW, 1.53 kW, 2.10 kW IMEP: 2.98 bar, 4.46 bar, 5.06 bar, 5.95 bar		Fuel Equivalence ratio : 0.230-0.749	100% load	Fuel Equivalence ratio: 0.3-0.5	50%, 75% and 100% load
Other Parameters			Injection timing: 30-10 BTDC 2 Different Nozzle 3 Type of Fuel: No. 2D, 50/50 SRF and N-Heptane			Injection timing: 30 deg BTDC, 24 deg BTDC, 21 deg BTDC, 18 deg BTDC, 15 deg BTDC

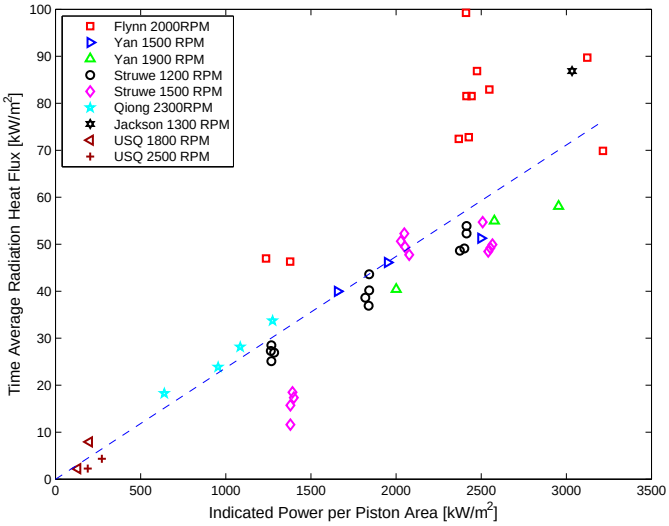

Figure 7.2: Cycle average radiation heat flux as a function of indicated power per unit piston area. The least-squares straight line fitted to the data and forced to pass through the origin has a slope of 0.0229 and $R^2 = 0.70$.

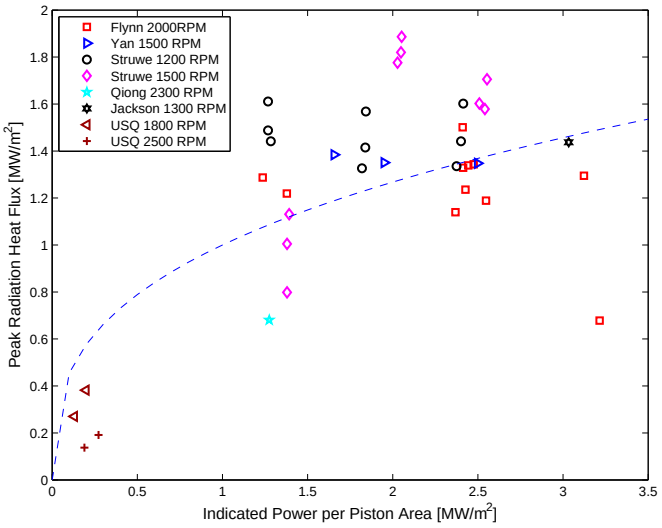

Figure 7.3: Peak radiation heat flux as a function of indicated power per unit piston area. The least-squares straight line fitted to the data and forced to pass through the origin has a slope of 0.698 with $R^2 = -0.06$ whereas the power-law curve has a coefficient $C = 0.717$ and an index $m = 0.828$ with $R^2 = 0.27$.

dimensions are the same as the heat flux, and it is also closely related to the engine scale. The indicated power per unit piston area can be written as

$$\frac{\mathrm{IP}}{A_p} = \frac{\overline{p}\, V_s N}{2} \frac{1}{A_p} \tag{7.12}$$

where $\overline{p}$ is the indicated mean effective pressure, V_s is the swept volume, N is the number of revolutions per second, the factor of 2 on the denominator arises because 4 stroke engines are being considered, and A_p is the piston area, and therefore,

$$\frac{\mathrm{IP}}{A_p} = \frac{\overline{p} N}{2} S \tag{7.13}$$

where S is the engine stroke. Thus, for geometrically similar engines of different scales which produce similar mean effective pressures and are operated at similar speeds, this power flux parameter is an indicator of engine size.

If in the process of scaling down to a smaller engine size, the rotational speed is increased in proportion to the decrease in the geometric scale so as to maintain Reynolds number similarity as discussed in Section 7.2, the parameter IP/A_p will not be a particularly useful indicator of engine size. However, for the data considered in the present work (Table 7.1), the data has been obtained over a range of speeds and there is no particular correlation of engine size with engine speed within the data set, hence the parameter IP/A_p stands as practical indicator of engine size within the context of the present data set.

Figure 7.2 presents the cycle averaged radiation heat flux values plotted against IP/A_p. A straight line passing through the origin has been fitted to the data in a least-squares sense and has resulted in a coefficient of determination of $R^2 = 0.70$, suggesting the proportional relationship between the cycle average radiation heat flux and the indicated power per unit piston area is a reasonable model. The

constant of proportionality is 0.0229.

Peak radiation heat flux data is also plotted against IP/A_p, and is presented Figure 7.3. In this case, a linear least-squares fit to the data which passes through the origin results in a coefficient of determination of $R^2 = -0.06$ and hence this does not represent a good model for the data. Instead, a power-law curve fit of the form

$$q_{r,peak} = C \left[\frac{\mathrm{IP}}{A_p}\right]^m \tag{7.14}$$

was trialled. In this expression C and m are the model parameters obtained by fitting the curve to the data in a least-squares sense. The curve fit in this case resulted in $R^2 = 0.27$, suggesting a substantially better model than the straight line. The fitted value of the index in this case is $m = 0.83$ which suggests that at the time of the peak radiation heat flux, radiation from the surface of the flame makes a significant contribution to the peak radiation heat flux value.

7.5 Thermodynamic Simulation

A quasi-one dimensional thermodynamic model was developed to study the effect of varying engine size on the radiation heat flux. This thermodynamic simulation was an extension of the spark ignition engine modeling programme developed by Buttsworth [53] with modifications to include a multi-zone capability, fuel injection, and localized combustion as necessary for simulation of direct injection diesel engines. The original thermodynamic simulation program was based on the FORTRAN code by Ferguson [54] where reactants are processed into products according to a pre-specified rate. The products of combustion are treated as being in chemical equilibrium using the approach of Olikara and Borman [55].

The thermodynamic simulation program solves the governing differential equations that represent the rates of change of the temperature, pressure and cylinder mass (due to blow-by). Radiation heat flux constitutes a component in the rates equation – specifically as a component of the heat transfer from the working gas to the wall – and is solved simultaneously during the integration process.

Engine scaling simulations were performed using the thermodynamic engine simulation tool with the KL radiation model presented in Chapter 3 for 8 different engine sizes. For these simulations, geometric scaling factors of 0.5, 1, 2.5, 4, 5.5, 7, 8.5 and 10 were applied to a baseline engine with a bore, $b = 0.070$ m. All of the engine parameters including the compression ratio, burn law, initial conditions, engine speed and heat transfer models remained the same for the different engine scales. The radiation model developed for the present work (Chapter 3) relies on the KL values which are correlated with the indicated power per unit piston area IP/A_p. However, because the indicated power is actually an output from the engine simulation, an iterative approach was necessary. An initial estimate for IP/A_p was used to define the necessary parameters for the radiation modelling and successive runs of the engine simulation were performed using the values of IP/A_p calculated from the previous simulation until there was less than a 1 % change between the previous and new values. Time-averaged radiation heat flux and peak radiation heat flux values from the simulations are presented in Figure 7.4 and 7.5.

The base engine configuration used in the simulations is based on the experiments performed in this research in which the engine bore, $b = 0.070$ m, engine stroke, $S = 0.055$ m and compression ratio, $r = 19.9$, and this is the smallest engine size of all the data sets considered, as displayed in Table A.1. The engine speed selected for the simulations was 1674 RPM, and this is the mean of all the engine speeds for which the experimental data is available. Fuel equivalence ratio was varied between 0.3 to 0.6 in all of the simulations as this is a reasonable range for most of the the 50 engine operating conditions considered. (The actual range

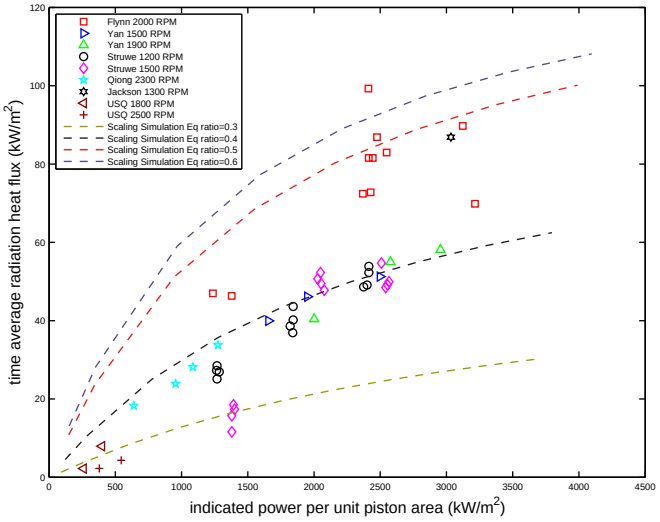

Figure 7.4: Simulation results for the time-averaged radiation heat flux as a function of indicated power per unit piston area with comparison to experimental results.

of equivalence ratios in the experimental data varied from 0.23 to 0.749.)

The initial conditions for the trapped mass in the cylinder at bottom dead centre were 353 K and 80 kPa, and a residual fraction of 0.1 was assumed. A Wiebe function burn law was selected to dictate the rate of conversion of reactants to products and the start of burn was specified as 15° before top dead centre, and the burn duration was set to be 55°. The start of the rise of KL was specified to coincide with the start of the burn.

Two sets of scaling simulations were performed: one with no convective heat flux losses, and the other with the convective heat flux calculated according to the Woschni model. In comparing results from the time-averaged radiation heat flux, and the peak radiation heat flux simulations from the two heat flux simulation cases, minimal differences were observed. Therefore, only the simulations with the convective model are presented as shown in Figure 7.4 and 7.5.

In Figure 7.4, simulation of the time-averaged radiation heat flux with an equivalence ratio of 0.4 which is approximately the mean value, produced the closest

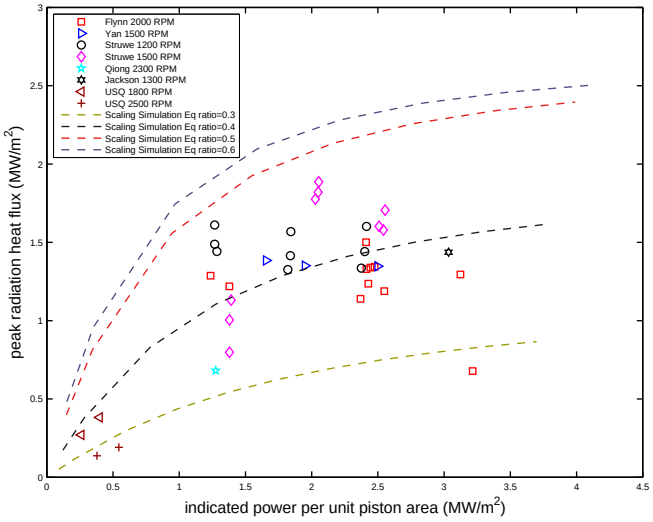

Figure 7.5: Simulation results for the peak radiation heat flux as a function of indicated power per unit piston area with comparison to experimental results.

match to most of the data points. From the form of the plotted simulation lines (which connect the simulation data points) it is appears that surface radiation effects become more significant with increasing equivalence ratio. This is evident when a powerlaw line is fitted to the simulation data points in a least-squares sense. When this is done, the values of index, m defined in Section 7.2 for each simulation case are 0.85, 0.76, 0.67, 0.64 for equivalence ratios of 0.3, 0.4, 0.5 and 0.6 respectively. The coefficient of determination being $R^2 = 0.97$, 0.95, 0.95, 0.94 for equivalence ratios of 0.3, 0.4, 0.5 and 0.6 respectively.

For the peak radiation heat flux results as shown in Figure 7.5, simulations with an equivalence ratio of 0.4 again shows a good match to the experimental data. Fitting powerlaw lines to the simulation data resulted in the values of index m of 0.76, 0.64, 0.54 and 0.49 for equivalence ratios of 0.3, 0.4, 0.5 and 0.6 respectively with the coefficient of determination being $R^2 = 0.94$, 0.92, 0.91 and 0.89, respectively. Again, the trend of decreasing values of m with increasing equivalence ratio indicates an increase in the significance of surface radiation effects.

7.6 Discussion

There is a direct relationship between the time-averaged radiation heat flux data and the indicated power per unit piston area which is used in the present work as a surrogate parameter reflecting the engine size, Figure 7.2. Results from the two smallest engines for which comprehensive radiation data is available conform to the indicated trend: the smallest time-averaged radiation heat flux data set has been recorded using the smallest engine bore (this study), and the second-smallest time-averaged radiation heat flux values have been reported from the second smallest engine bore [9].

It is noted that the experiments from Flynn [22] and Jackson [3] produce the highest time-averaged radiation heat flux values even though both engine bores are smaller than the one of Yan [23] and Struwe [24]. In the work of Jackson [3], a theoretical window factor was used to scale all of the instantaneous radiation heat flux values obtained by the thermocouple method [3]. It is possible that this window factor value could be overestimated and may be contributing to the apparently high value of the time-averaged radiation heat flux. As for data from Flynn [22], the probe location on the cylinder wall and the piston slot which enabled a side-view into the piston bowl [22] might contribute to the high values of time-averaged radiation heat flux because: (1) the duration of the radiation heat flux signals could be longer in comparison to the other data which were obtained with probes facing the piston bowl from the engine head; and (2) the relatively large optical path length associated with the view across the piston. The combustion chamber swirl condition might also play a part in the radiation heat transfer heat losses to the wall. The fact that the Struwe and Yan engine had low swirl ratios [24, 7, 23] compared to the other engines might offer some explanation of the observed results.

7.7 Conclusion

The time-averaged radiation heat flux data obtained from different engine sizes, configurations and operating condition of this study and those of other researchers [23, 7, 9, 3, 22] appear to be linearly related to a surrogate parameter reflecting the engine size, IP/A_p. This linearity implies the time-averaged radiation heat flux is strongly influenced by volume effects. In contrast, the peak radiation heat flux data appears to scale via a power law relationship with an index of 0.83, indicating that in this case, it is a weaker function of engine size with surface radiation effects from the soot cloud being more significant. As the soot cloud density is at a maximum value during peak radiation heat flux, the flame will appear more opaque at this time, and the surface radiation heat transfer effects will be more significant. However, during times other than at peak heat flux values, radiation heat flux is more strongly influenced by volume effects.

Results from the quasi zero-dimensional thermodynamic scaling simulation employed using the newly KL radiation model reported in Chapter 3 complement the experimental data although the differences between the time-averaged and peak heat flux results are not as striking. Values of the powerlaw index m of 0.76 and 0.64 were obtained from least squares fits to the simulation data in the case of time-averaged, and peak results respectively. Although stronger surface radiation effects are indicated in the simulation results for the case of the peak values (the value of m is smaller in this case), volume radiation effects play an important role in both time-averaged and peak radiation conditions.

Chapter 8

Conclusions

8.1 Summary

Through the work described in this dissertation a number of achievements have been possible.

- A radiation heat flux and associated measurement hardware has been developed for a small diesel engine at the University of Southern Queensland.
- A version of the two-colour method has been developed.
- Methods to compensate for the radiation heat flux probe sooting effects have been developed.
- A convective heat flux probe has been developed for the small diesel engine.
- Methods to compensate for the convective heat flux probe sooting effects have been developed.
- Radiation heat flux measurements have been obtained on a direct injection diesel engine that is substantially smaller than any other engine for which such radiation data is available in the open literature.

- Complementary convective heat flux data has been obtained on the same engine for the purpose of benchmarking the radiation results.

- A new empirical radiation model based on available KL data from various sources including the present work has been developed and implemented in a thermodynamic engine simulation tool.

- A scaling analysis has been developed in an attempt to correlate the radiation results from different authors.

8.2 Conclusions

A number of conclusions can be drawn from the observations of this study.

- The new radiation heat flux and convective heat flux measurements in the small DI diesel engine have yielded smaller ratios of peak and time-averaged radiation heat flux than previous studies [22, 23, 9]. The present experiments were performed on an engine that is substantially smaller than other engines for which such data are available. In the case of experiments that focused on radiation heat transfer measurements, the engine size used in this study is the smallest and hence the new data represent valuable radiation heat transfer results. These results reflect the significant influence of engine size on the radiation heat flux values. For example, the range for the ratio of time-averaged radiation to convective heat flux obtained in this study is 1.3-2.7 % using a 0.21 L engine while the range of 11-25 % was obtained in other works [22, 23, 9] which used engine sizes of 0.86-2.33 L.

- A compilation of time-averaged radiation heat flux data from various sources including those obtained those obtained in the present work demonstrates a linear correlation with engine scale ($m \approx 1$). In contrast, the corresponding peak radiation heat flux data correlates better with engine scale when

a power law function of engine scale is used. In this case, the power law index is $m = 0.83$. These results indicate that in both the time-averaged and the peak radiation heat flux cases, the flame size plays a significant role since the correlation indices are significantly larger than zero. However, for the peak radiation heat flux, the flame surface radiation effects are also relevant because the power law index in this case is significantly less than unity. The flame tends to be more opaque at conditions of peak radiation due to the high density of soot particles as reflected in the high KL values at peak radiation conditions.

- The results from the quasi zero-dimensional thermodynamic engine scaling simulations which employed the new KL radiation model support the notion that both the time-averaged radiation heat flux and the peak radiation heat flux are influenced by flame scale. Power law indices of 0.76 and 0.64 were obtained for the time-averaged and peak radiation heat flux simulation data respectively. The lower value of power law index for peak radiation heat flux reflects the contribution of flame surface radiation effects near the time of peak radiation heat flux.

- The effect of sooting on the radiation heat flux measurement was compensated by scaling the post-run calibration with the ratio of signal strength indicators for the particular period under consideration and the last period prior to calibration. Using the peak values as the signal strength indicator, the resulting spectral emissions appear relatively constant throughout all the periods in terms of the peak values and overall variation with crank angle.

- For the convective heat flux measurements, the effect of sooting of the probe surface was compensated by deducing the soot thickness through the heat flux analysis with reference to a motoring case in which the probe surface was clean. The method appears to be successful because the results show the range of peak values is maintained relatively constant across different periods and the results appear to have the correct phase.

8.3 Recommendations

Based on the findings of this study, there are some areas requiring further investigation in the field of radiation heat transfer loss from diesel engines.

- To assist the scaling analysis, a number of different scale engines could be used in the experimental work and these would have the same geometric configuration. Nondimensional parameters would be held constant and/or varied in a controlled manner for the engine testing.
- Radiation modelling developments would also benefit from the availability of additional data (including KL values and apparent flame temperature) for a range of engine scales.
- The radiation probe could be improved through addition of a soot cleaning mechanism. A cavity or gas purging technique might offer a solution although these may not be effective in high load cases.
- Failure of the thermocouple probe in service arose primarily because of debonding between thermocouple and the probe housing. An improved design is required.
- The spatial variability of the radiation and convection heat flux in the present work has not been quantified. Future experiments and analysis should seek to clarify this potential variability.

References

[1] T. Kamimoto and Y. Murayama, "Re-examination of the Emissivity of Diesel Flames," *International Journal of Engine Research*, vol. 12, Oct 2011.

[2] N. Ladommatos and H. Zhao, "A Guide to measurement of flame temperature and soot concentration in diesel engines using the two-colour method, part 1: Principles," *SAE Paper*, Oct. 1994, no. 941956.

[3] N. Jackson, A. Pilley, and N. Owen, "Instantaneous heat transfer in a highly rated DI truck engine," *SAE Paper*, Feb. 1990, no. 900692.

[4] T. LeFeuvre, P. Myers, and O. Uyehara, "Experimental Instantaneous Heat Fluxes in a Diesel Engine and Their Correlation," *SAE Paper*, Feb. 1964, no. 690464.

[5] G. Sitkei and G. Ramanaiah, "Rational approach for calculation of heat transfer in diesel engines," *SAE Paper*, 1972, 720027.

[6] P. F. Flynn, "An Experimental Determination of the Instantaneous Potential Radiant Heat Transfer Within an Operating Diesel Engine," Ph.D. dissertation, University of Wisconsin-Madison, 1971.

[7] F. Struwe, "In-Cylinder Measurement of Particulate Radiant Heat Transfer In a Direct-Injection Diesel Engine," Master's thesis, University of Wisconsin-Madison, 2002.

[8] J. Yan, "Analysis and In-Cylinder Measurements of Local and Hemispherical

Particulate Radiant Emissions and Temperatures in a Direct Injection Diesel Engine," Ph.D. dissertation, University of Wisconsin-Madison, 1988.

[9] W. Qiong, Z. Xin, J. Pinwen, and L. Jianhua, "Comparison of a radiation model with experiment in a diesel engine," *SAE Paper*, May 1998, no. 981452.

[10] "Diesels Are More Than Half of New Cars Sold in Western Europe," http://www1.eere.energy.gov/vehiclesandfuels/facts/2012_fotw716.html, US Department of Energy, 2012.

[11] *The Road Ahead 2011*, US Department of Commerce, 2011.

[12] *Light Duty and Medium Duty Clean Diesel Vehicles: Global Market Analysis and Forecasts*, Pike Research, 2012, executive Summary.

[13] T. V. Johnson, "Diesel emission control in review," *SAE Technical Paper Series*, Jan. 2008, no. 2008-01-0069.

[14] T. Morel and R. Keribar, "Heat Radiation in D.I. Diesel Engine," *SAE Paper*, Mar. 1986, no. 860445.

[15] M. Nuti, "Small Engines Evolution: The Road Ahead," *SAE Technical Paper*, no. 2001-12-01, Dec. 2001, doi:10.4271/2001-01-2041.

[16] D. Boggs, R. C. Belaire, B. Bartunek, M. Drnholz, and H. Ecker, "A Small Displacement DI Diesel Engine Concept for High Fuel Economy Vehicles," *SAE Paper*, Aug. 1997, no. 972680.

[17] W. L. Chang, W. G. Hai, R. D. Reitz, E. Kurtz, and W. Willems, "Computational Optimization of a Down-Scaled Diesel Engine Operating in the Conventional Diffusion Combustion Regime Using a Multi-Objective Genetic Algorithm," *Combustion Science and Technology*, vol. 184, no. 1, pp. 78–96, Jan. 2012.

[18] L. A. Stager and R. D. Reitz, "Assessment of Diesel Engine Size-Scaling Relationships," *SAE Technical Paper*, no. 2007-01-0127, Apr. 2007.

[19] J. Heywood, *Internal Combustion Engine Fundamentals*, 1st ed. New York, NY: McGraw-Hill, 1988.

[20] G. Borman and K. Nishiwaki, "Internal-combustion Engine Heat Transfer," *Progress in Energy and Combustion Science*, vol. 13, no. 1, pp. 1–46, Aug. 1987.

[21] G. D. Ebersole, P. Meyers, and O. Uyehara, "The Radiat and Convective Components of Diesel Engine Heat Transfer," *SAE Technical Paper Series*, Jan. 1963, no. 630148.

[22] P. Flynn, M. Mizukawa, O. Uyehara, and P. Myers, "An Experimental Determination of the Instantaneous Potential Radiant Heat Transfer Within an Operating Diesel Engine," *SAE Paper*, Feb. 1972, no. 720022.

[23] J. Yan and G. Borman, "Analysis and In-Cylinder Measurement of Particulate Radiant Emissions and Temperature in a Direct Injection Diesel," *SAE Paper*, Sep. 1988, no. 881315.

[24] F. Struwe and D. Foster, "In-Cylinder Measurement of Particulate Radiant Heat Transfer In a Direct-Injection Diesel Engine," *SAE Paper*, Sep. 2003, no. 2003-01-0072.

[25] Y. Matsui, T. Kamimoto, and S. Matsuoka, "Study on the Time and Space Resolved Measurement of Flame Temperature and Soot Concentration in a D. I. Diesel Engine by the Two-Color Method," *SAE Paper*, Feb. 1979, no. 790491.

[26] W. Annand and T. Ma, "Instantaneous Heat Transfer Rates to the Cylinder Head Surface of A Small Compression-Ignition Engine," *Proc Instn Mech Engrs*, vol. 185, no. 1, pp. 976–987, Nov. 1970.

[27] J. Dent and S. Sulaiman, "Convective and Radiation Heat Transfer in High Swirl Direct-Injection Diesel Engine," *SAE Paper*, Feb. 1977, no. 770407.

[28] C. Rakopoulos and G. Mavropoulos, "Experimental Instantaneous Heat Fluxes in the Cylinder Head and Exhaust Manifold of an Air-Cooled Diesel Engine," *Energy Conversion and Management*, vol. 41, no. 12, p. 12651281, Aug. 2000.

[29] T. Oguri and S. Inaba, "Radiant Heat Transfer in Diesel Engines," *SAE Paper*, Feb. 1972, no. 720023.

[30] O. Uyehara, P. Meyers, K. M. Watson, and L. A. Wilson, "Flame Temperature in Internal-Combustion engines," *Transactions of the ASME*, vol. 68, no. 1, pp. 17–30, Jan. 1946.

[31] N. Ladommatos and H. Zhao, "A Guide to measurement of flame temperature and soot concentration in diesel engines using the two-colour method, part 2: Implementation," *SAE Paper*, Oct. 1994, no. 941956.

[32] H. Hottel and F. Broughton, "Determination of True Temperature and Total Radiation From Luminous Gas Flames," *Industrial and Engineering Chemistry, Analytical Ed.*, vol. 4, no. 2, pp. 166–175, Apr. 1932.

[33] Y. Matsui, T. Kaminoto, and S. Matsuoka, "A Study on the Application of the Two-Color Method to the Measurement of Flame Temperature and Soot Concentration in Diesel Engines," *SAE Paper*, Sep. 1980, no. 800970.

[34] Incropera and D. Witt, *Introduction to Heat Transfer*, 4th ed. New York, NY: John Wiley and Sons, 2002.

[35] Y. Matsui, T. Kaminoto, and S. Matsuoka, "Formation and Oxidation Processes of Soot Particulates in a DI Diesel Engine An Experimental Study via the Two-Color Method," *SAE Paper*, Feb. 1982, no. 820464.

[36] X. Li and J. Wallace, "In-Cylinder Measurement of Temperature and Soot Concentration Using the Two-Color Method," *SAE Paper*, Feb. 1995, no. 950848.

[37] J. McDonald, "Construction and testing of facility for diesel engine," Master's thesis, University of Wisconsin-Madison, 1984.

[38] V. Overbye, J. Bennethum, O. Uyehara, and P. Myers, "Unsteady Heat Transfer in Engines," *SAE Technical Paper*, Jan. 1961, no. 610041.

[39] M. Hara and T. Oguri, "Measurement of Piston Temperature," *Bulletin of Japan Society of Mechanical Engineers*, vol. 2, no. 7, pp. 382–389, Jan. 1959.

[40] N. Whitehouse, "Heat Transfer in a Quiescent Chamber Diesel Engine," *Proceedings of the Institution of Mechanical Engineer*, vol. 185, no. 1, pp. 963–975, Nov. 1970.

[41] W. Annand, "Heat Transfer in the Cylinders of Reciprocating Internal Combustion Engines," *Proc Instn Mech Engrs*, vol. 177, pp. 973–990, 1963.

[42] C. A. Finol and K. Robinson, "Thermal modelling of modern engines: a review of empirical correlations to estimate the in-cylinder heat transfer coefficient," *Proceedings of the Institution of Mechanical Engineers, Part D: Journal of Automobile Engineering*, vol. 220, no. 12, pp. 1765–1781, Dec. 2006.

[43] C. Tiena and S. Lee, "Flame radiation," *Progress in Energy and Combustion Science: An International Review Journal*, vol. 8, no. 1, pp. 41–59, 1982.

[44] *LA Series Service Manual*, Yanmar Co. Ltd., 2000, operating Manual.

[45] *Operating Instructions and Specifications: NI 9205*, National Instruments, 2008, operating Manual.

[46] M. L. G. Oldfield, "Impulse Response Processing of Transient Heat Transfer Gauge Signals," *ASME Conf. Proc.: Heat Transfer, Parts A and B*, vol. 3, pp. 739–750, May 2006, no. GT2006-90949.

[47] *PDA55 Operating Manual*, Thorlab Inc., 2005, operating Manual.

[48] *PDA36A Operating Manual*, Thorlab Inc., 2007, operating Manual.

[49] I. Mohammad, "Simultaneous pyrometer measurements along three path directions in open chamber diesel," Ph.D. dissertation, University of Wisconsin-Madison, 1990.

[50] R. Peterson and K. Wu, "The Effect of Operating Conditions on Flame Temperature in a Diesel Engine," *SAE Technical Paper*, Oct. 1986, no. 861565.

[51] C. Schubert, A. Wimmer, and F. Chmela, "Advanced Heat Transfer Model for CI Engines," *SAE Technical Paper*, Apr. 2005, no. 2005-01-0695.

[52] J. Doorly and M. Oldfield, "The Theory of Advanced Multi-layer Thin Film Heat Transfer Gauges," *International Journal of Heat and Mass Transfer*, vol. 30, no. 6, pp. 1159–1168, Jun. 1987.

[53] D. R. Buttsworth, "Spark Ignition Internal Combustion Engine Modelling using Matlab," *Faculty of Engineering and Surveying Technical Reports, University of Southern Queensland, Australia*, Oct. 2002, report TR-2002-02.

[54] C. Ferguson, D. Tree, and D. DeWitt, "Design, Calibration and Error Analysis of Instrumentation for Heat Transfer Measurements in Internal Combustion Engines," *Developments in Experimental Techniques in Heat Transfer and Combustion; ASME Proceedings of the Twenty-fourth National Heat Transfer Conference and Exhibition*, pp. 67–82, Aug. 1987, a88-18505 05-35 US DOE-sponsored research.

[55] C. Olikara and G. Borman, "A Computer Program for Calculating Properties of Equilibrium Combustion Products with Some Applications to I.C. Engines," *SAE Technical Paper*, no. 750468, Feb. 1975.

[56] S. Wahiduzzaman and T. Morel, "Eexperimental and Analytical Study of Heat Radiation in a Diesel Engine," *SAE Paper*, Feb. 1987, no. 870571.

[57] H. C. van de Hulst, "Light Scattering by Small Particles," *Quarterly Journal of the Royal Meteorological Society*, vol. 84, no. 360, p. 198199, 1958.

[58] I. Sher, D. Levinzon-Sher, and E. Sher, "Miniaturization Limitations of HCCI Internal Combustion Engines," *Journal of Applied Thermal Engineering*, vol. 29, p. 400411, Mar. 2008.

[59] P. Therkelsena and D. Dunn-Rankina, "Small-Scale HCCI Engine Operation," *Combustion Science and Technology*, vol. 183, no. 9, pp. 928–946, May 2011.

[60] G. Woschni and W. Spindler, "Heat Transfer With Insulated Combustion Chamber Walls and Its Influence on the Performance of Diesel Engines," *Journal of Engineering for Gas Turbines and Power*, vol. 110, no. 3, pp. 482–488, Jul. 1988.

[61] G. Woschni, "A Universally Applicable Equation for the Instantaneous Heat Transfer Coefficient in the Internal Combustion Engine," *SAE Technical Paper*, Feb. 1967, no. 670931.

[62] B. Lawton, "Effect of Compression and Expansion on Instantaneous Heat Transfer in Reciprocating Internal Combustion Engines," *Proceedings of the Institution of Mechanical Engineers, Part A: Journal of Power and Energy*, vol. 201, no. 3, pp. 175–186, Aug. 1987.

[63] A. Alkidas, "Heat Transfer Characteristics of a Spark Ignition Engine," *Journal of Heat Transfer, Trans ASME*, vol. 102, pp. 817–830, May 1980.

[64] R. Siegel and J. Howell, *Thermal Radiation Heat Transfer*, 4th ed. New York, NY: Taylor and Francis, 2002.

[65] C. Ferguson, *Internal Combustion Engines*, 1st ed. New York, NY: John Wiley and Sons, 1986.

[66] *Report of Calibration for One Standard of Spectral Irradiance OL 200M*, Optronic Laboratories, 2009, calibration Report.

[67] "Diesel Technology Forum," http://http://www.dieselforum.org, Diesel Technology Forum, 2012.

Appendix A

Tabulated data from various sources

Table A.1: Experimental parameters for selected instantaneous radiation heat transfer works

		USQ	Qiong	Flynn	Jackson	Yan	Struwe
Engine Parameter	Combustion chamber	Swirl	Swirl	Swirl	Swirl	quiescent	quiescent
	Bore (mm)	70	100	114.3	130.2	139.7	139.7
	Stroke (mm)	55	110	114.3	150	152.4	152.4
	Compression Ratio	19.9	18.4	16.7	13.5	13.23	13.1
	Displacement (L)	0.211	0.864	1.1728	2.0	2.33	2.33
‘ Radiation Probe Feature	Field of view (deg)	14	NA	NA	Theoretical hemispherical based on calculated window factor of 0.455.	14	Theoretical hemispherical via extrapolation of Probe 1 and 2 Probe 1 : 57.7% hemispherical Probe 2 : 84.25% hemispherical
	Method	Two-colour	Shielded thermocouple	Two-colour	Shielded thermocouple	Two-colour	Two-colour
	Rod Window	Quartz, 1.8mm diameter	Sapphire window	2x 0.25 inch diam Quartz	Sapphire, 4mm diameter	sapphire, 6.35mm diameter	lucalox, 6.35mm diameter
		On the cylinder head	On the cylinder head	On the side of cylinder head	On the cylinder head	On the cylinder head	On the cylinder head
	Position	Facing piston bowl	Facing piston bowl	Facing piston bowl	Facing piston bowl	Facing piston bowl	Facing piston bowl
	Special feature	Interpolated Calibration Constant based on post-calibration	Jet purging soot cleaning	Windows can be changed while engine operating where tranmission are maintained above 0.7 .	Calculation of window factor taking account of reflection, refraction and shadowing effect. Radiation Heat Flux measured on few cycles after IMEP established to obtain ’soot free’ result	Soot cleaning mechanism - cavity	Soot cleaning mechanism - cavity
Engine Operating Condition	Mean Speed (RPM)	1800, 2500	2300	2000	1300	1500, 1900	1200, 1500
	Info on Load	IP: 1.0 kW, 1.46 kW, 1.53 kW, 2.10 kW	IMEP: 2.98 bar, 4.46 bar, 5.06 bar, 5.95 bar	Fuel Equivalence ratio : 0.230-0.749	100% load	Fuel Equivalence ratio: 0.3-0.5	50%, 75% and 100% load
	Other Parameters			Injection timing: 30-10 BTDC 2 Different Nozzle 3 Type of Fuel: No. 2D, 50/50 SRF and N-Heptane			Injection timing: 30 deg BTDC, 24 deg BTDC , 21 deg BTDC, 18 deg BTDC, 15 deg BTDC

Table A.2: Selected data presented by Flynn [6].

No	Run	RPM	Eq. Ratio	Manifold Pressure (Hg)	Injection Advance (°CA BTDC)	Fuel	Nozzle	Cetane No.	Energy Fuel Rate (btu/cyc)	IMEP (psi)	Fuel Rate (lb/cyc)	Indicated Power (HP)	Time Average RHF (btu/h/ft^2)
1	20	2000	0.514	59.8	20	2D	1	40	3.459	194	0.000188	35.06	NA
2	27	2010	0.23	60.2	20	2D	1	40	1.529	104.4	0.000083	18.96	NA
3	77	2000	0.749	59.6	20	2D	1	40	4.871	244.8	0.000265	44.24	NA
4	84	1995	0.459	59.8	20	2D	1	40	3.059	180.8	0.000167	32.59	22957
5	91	2005	0.469	75.4	20	2D	1	40	3.998	237.2	0.000218	42.98	28441
6	98	1995	0.438	30.1	20	2D	1	40	1.492	94.4	0.000081	17.02	14893
7	111	2005	0.455	60.2	20	2D	2	40	3.069	188	0.000167	34.06	27531
8	118	2005	0.439	59.7	20	50/50 SRF	2	44	2.954	185.6	0.000161	33.63	25850
9	125	1995	0.455	59.9	30	50/50 SRF	2	44	3.038	184	0.000165	33.17	31466
10	140	1980	0.434	60.4	20	50/50 SRF	2	44	2.984	185.6	0.000163	33.21	25850
11	148	2000	0.445	60.3	20	N-Heptane	2	55	3.027	184.8	0.000165	33.4	23072

Table A.3: Calculated results based on data available from Flynn et al. [6].

No	Run	IMEP (kPa)	Fuel Rate per Cycle (kg/cyc)	Fuel Rate per Second (kg/s)	Energy Fuel per Cycle (J/cyc)	Fuel Energy Injected per Second (J/s)	Specific Energy Injected (J/kg)	Time Average RHF (W/m^2)	Time Average RHTransfer (kW)	Indicated Power (kW)	Indicated Power per Piston due to IMEP (kW/m^2)	Indicated Power due to Fuel Energy (kW)
1	20	1337.582912	0.0000853	0.001421256	3649.439	60823.9784	42795931.51	82.928	1.70181963	26.14556517	2548.095448	60.8239784
2	27	719.81266	0.0000376	0.000630607	1613.181	27020.77545	42848849.36	46.31	0.95035775	14.14043809	1378.099333	27.02077545
3	77	1687.836582	0.0001202	0.002003366	5139.178	85652.96293	42754519.18	69.863	1.43370424	32.99192966	3215.328689	85.65296293
4	84	1246.572116	0.0000757	0.001259343	3227.416	53655.79605	42606197.57	72.41992239	1.48617651	24.3056721	2368.783082	53.65579605
5	91	1635.436427	0.0000989	0.001652172	4218.114	70477.65288	42657565.59	89.7196939	1.84119642	32.04758958	3123.295159	70.47765288
6	98	650.8650872	0.0000367	0.000610819	1574.144	26170.13655	42844351.66	46.98130872	0.96413411	12.69057216	1236.798246	26.17013655
7	111	1296.214369	0.0000757	0.001265655	3237.967	54101.02969	42745479.02	86.84901701	1.78228538	25.4002818	2475.461593	54.10102969
8	118	1279.666951	0.0000730	0.001220182	3116.635	52073.78354	42677049.44	81.54615123	1.67346181	25.07602288	2443.859956	52.07378354
9	125	1268.63534	0.0000748	0.001244261	3205.26	53287.44963	42826599.92	99.26232862	2.03702705	24.73586099	2410.708446	53.28744963
10	140	1279.666951	0.0000739	0.001219937	3148.287	51946.73722	42581502.88	81.54615123	1.67346181	24.76335426	2413.387887	51.94673722
11	148	1274.151145	0.0000748	0.001247379	3193.655	53227.5752	42671533.23	72.78270024	1.49362131	24.90567239	2427.257932	53.2275752

Table A.4: Calculated ratios based on data available from Flynn et al. [6].

No	Run	Ratio of Time Average Radiation Heat Flux to Indicated Power per Piston Area	Ratio of Time Average Radiation Heat Transfer to Indicated Power	Ratio of Time Average Radiation Heat Transfer to Fuel Energy Rate Injected
1	20	0.032545092	0.065090183	0.02797942
2	27	0.033604254	0.067208508	0.035171372
3	77	0.021728105	0.04345621	0.016738525
4	84	0.030572627	0.061145255	0.027698341
5	91	0.028725973	0.057451947	0.026124542
6	98	0.037986235	0.07597247	0.036841004
7	111	0.035083969	0.070167937	0.03294365
8	118	0.033367768	0.066735535	0.032136359
9	125	0.041175584	0.082351168	0.038227145
10	140	0.033789078	0.067578156	0.032214955
11	148	0.029985565	0.05997113	0.028061044

Table A.5: Selected data presented by Struwe [7].

No	Run	RPM	Injection Timing signal °ATDC	Load (%)	Equivalent Ratio	Time Average Radiant Heat Flux (kW/m^2)	Energy per Cycle (J/cyc)	Fuel Flow (kg/cyc)	IMEP (kPa)
1	230_15	1200	-15	50	0.482	26.94	4610	0.000106	842.7
	230_18	1200	-18	50	0.482	25.12	4610	0.000106	831.9
	230_21	1200	-21	50	0.482	28.49	4610	0.000106	831.9
	230_30	1200	-30	50	0.482	27.29	4610	0.000106	829.8
2	278_15	1200	-15	75	0.585	38.61	6790	0.000156	1194
	278_21	1200	-21	75	0.585	36.91	6790	0.000156	1206.9
	278_24	1200	-24	75	0.585	40.19	6790	0.000156	1209.1
	278_30	1200	-30	75	0.585	43.62	6790	0.000156	1209.1
3	331_15	1200	-15	75	0.635	48.62	9230	0.000212	1558.2
	331_18	1200	-18	75	0.635	49.1	9230	0.000212	1575.5
	331_21	1200	-21	75	0.635	52.29	9230	0.000212	1584.1
	331_24	1200	-24	75	0.635	53.87	9230	0.000212	1584.1
4	217_18	1500	-18	50	0.413	11.61	3980	0.0000915	724.2
	217_21	1500	-21	50	0.413	15.71	3980	0.0000915	724.2
	217_24	1500	-24	50	0.413	18.5	3980	0.0000915	730.6
	217_30	1500	-30	50	0.413	17.36	3980	0.0000915	734.9
5	260_18	1500	-18	75	0.526	50.65	6060	0.000139	1064.7
	260_21	1500	-21	75	0.526	52.28	6060	0.000139	1075.5
	260_24	1500	-24	75	0.526	49.46	6060	0.000139	1077.6
	260_30	1500	-30	75	0.526	47.76	6060	0.000139	1090.6
6	295_18	1500	-18	100	0.536	54.7	7510	0.000173	1316.9
	295_21	1500	-21	100	0.536	48.46	7510	0.000173	1334.1
	295_24	1500	-24	100	0.536	49.19	7510	0.000173	1340.6
	295_30	1500	-30	100	0.536	49.93	7510	0.000173	1347

Table A.6: Calculated results based on data available from Struwe [7].

No	Run	Specific Energy (J/kg)	Mass Fuel Flow Rate (kg/s)	Fuel Energy Injected per Second (J/s)	Time Average Radiation Heat Transfer (kW)	Indicated Power (kW)	Indicated Power per Piston Area (kW/m^2)	Fuel Energy Rate (kW)
1	230_15	43490566.04	0.00106	46100	0.825867	19.6852373	1284.2748	46.1
	230_18	43490566.04	0.00106	46100	0.770074	19.43295231	1267.8156	46.1
	230_21	43490566.04	0.00106	46100	0.873384	19.43295231	1267.8156	46.1
	230_30	43490566.04	0.00106	46100	0.836597	19.3838969	1264.6152	46.1
2	278_15	43525641.03	0.00156	67900	1.183621	27.89150746	1819.656	67.9
	278_21	43525641.03	0.00156	67900	1.131506	28.19284787	1839.3156	67.9
	278_24	43525641.03	0.00156	67900	1.232057	28.24423926	1842.6684	67.9
	278_30	43525641.03	0.00156	67900	1.337206	28.24423926	1842.6684	67.9
3	331_15	43537735.85	0.00212	92300	1.490485	36.39911803	2374.6968	92.3
	331_18	43537735.85	0.00212	92300	1.5052	36.80324121	2401.062	92.3
	331_21	43537735.85	0.00212	92300	1.602992	37.00413482	2414.1684	92.3
	331_24	43537735.85	0.00212	92300	1.651428	37.00413482	2414.1684	92.3
4	217_18	43497267.76	0.00114375	49750	0.355914	21.14638788	1379.601	49.75
	217_21	43497267.76	0.00114375	49750	0.481603	21.14638788	1379.601	49.75
	217_24	43497267.76	0.00114375	49750	0.567132	21.33326565	1391.793	49.75
	217_30	43497267.76	0.00114375	49750	0.532185	21.45882416	1399.9845	49.75
5	260_18	43597122.3	0.0017375	75750	1.552716	31.08886934	2028.2535	75.75
	260_21	43597122.3	0.0017375	75750	1.602685	31.40422558	2048.8275	75.75
	260_24	43597122.3	0.0017375	75750	1.516236	31.46554485	2052.828	75.75
	260_30	43597122.3	0.0017375	75750	1.464121	31.84514033	2077.593	75.75
6	295_18	43410404.62	0.0021625	93875	1.676872	38.45302154	2508.6945	93.875
	295_21	43410404.62	0.0021625	93875	1.48558	38.95525556	2541.4605	93.875
	295_24	43410404.62	0.0021625	93875	1.507959	39.14505329	2553.843	93.875
	295_30	43410404.62	0.0021625	93875	1.530644	39.33193107	2566.035	93.875

Table A.7: Calculated ratios based on data available from Struwe [7].

No	Calculated Ratios Run code	Ratio of Time Average Radiation Heat Flux to Indicated Power per Piston Area	Ratio of Time Average Radiation Heat Transfer to Indicated Power	Ratio of Time Average Radiation Heat Transfer to Fuel Energy Rate Injected
1	230_15	0.020976819	0.041953638	0.017914692
	230_18	0.019813607	0.039627214	0.01670442
	230_21	0.022471722	0.044943444	0.018945419
	230_30	0.021579687	0.043159374	0.018147437
2	278_15	0.021218296	0.042436592	0.017431819
	278_21	0.020067247	0.040134494	0.016664296
	278_24	0.021810761	0.043621522	0.018145165
	278_30	0.023672192	0.047344384	0.019693757
3	331_15	0.020474193	0.040948385	0.016148268
	331_18	0.020449285	0.040898569	0.016307691
	331_21	0.021659632	0.043319265	0.017367193
	331_24	0.022314102	0.044628204	0.017891962
4	217_18	0.008415477	0.016830953	0.007154048
	217_21	0.01138735	0.022774701	0.009680455
	217_24	0.013292207	0.026584413	0.011399645
	217_30	0.012400137	0.024800275	0.010697181
5	260_18	0.024972224	0.049944447	0.020497906
	260_21	0.025517034	0.051034067	0.021157562
	260_24	0.024093592	0.048187184	0.020016317
	260_30	0.022988141	0.045976281	0.019328332
6	295_18	0.021804169	0.043608339	0.017862822
	295_21	0.019067776	0.038135552	0.015825089
	295_24	0.019261168	0.038522337	0.016063477
	295_30	0.019458035	0.038916071	0.016305131
	Mean	0.019965202	0.039930404	0.016556253

Table A.8: Selected data presented by Yan [8].

Run code	Mean RPM	RPM	Inlet Pressure (kPa)	Inlet temperature (K)	Coolant Temperature (K)	Equivalence Ratio	IMEP (kPa)	Fuel Injected per Cycle (kg/cyc)	Time Average Radiation Heat Flux (kW/m^2)
14	1500	1499	202	333	383	0.287	870	0.000093578	39.9627
15	1500	1495	203	333	381	0.394	1027	0.00012824	46.1194
16	1500	1505	203	333	384	0.493	1307	0.00015974	51.2687
23	1900	1896	200	333	356	0.307	831	0.00010009	40.4104
24	1900	1893	200	333	356	0.398	1072	0.00012982	54.9627
25	1900	1893	200	333	356	0.463	1229	0.00015129	58.097

Table A.9: Calculated results based on data available from Yan. [8].

Run code	Energy Injected per Cycle (J/cyc)	Energy Injected per Second (J/s)	Mass Fuel Rate (kg/s)	Fuel Specific Energy (J/kg)	Time Average Radiation Heat Transfer (kW)	Indicated Power (kW)	Indicated Power per Piston Area (kW/m^2)	Fuel Energy Rate (kW)
14	4197.44119	52433.0362	0.001168945	44855000	1.225088638	25.38676133	1656.2451	52.4330362
15	5752.2052	71662.88978	0.001597657	44855000	1.413827217	29.88808233	1949.91355	71.6628898
16	7165.1377	89862.76865	0.002003406	44855000	1.571683141	38.29115814	2498.13445	89.8627687
23	4489.53695	70934.68381	0.001581422	44855000	1.238813241	30.67084713	2000.98152	70.9346838
24	5823.0761	91859.02548	0.002047911	44855000	1.684925675	39.50315782	2577.20592	91.8590255
25	6786.11295	107050.9318	0.0023866	44855000	1.781010157	45.28860165	2954.65119	107.050932

Table A.10: Calculated ratios based on data available from Yan. [8].

Run code	Ratio of Time Average Radiation Heat Flux to Indicated Power per Piston Area	Ratio of Time Average Radiation Heat Transfer to Indicated Power	Ratio of Time Average Radiation Heat Transfer to Fuel Energy Rate Injected
14	0.02412849	0.048256988	0.023364824
15	0.02365202	0.047304046	0.019728861
16	0.02052279	0.041045589	0.017489814
23	0.02019529	0.040390578	0.01746414
24	0.02132647	0.042652936	0.018342516
25	0.0196629	0.039325793	0.016637036
Mean	0.02158133	0.043162655	0.018837865

Table A.11: Selected data from Qiong et al. [9].

No	RPM	BMEP (Pa)	Measured Total Heat Flux (MW/m^2)	Ratio of Radiation Heat Flux to Total Heat Flux	IMEP (kPa)	Time Average Radiation Heat Flux (kW/m^2)
1	2300	298000	0.242	7.3	303.3259	18.2609
2	2300	446000	0.266	8.83	452.9933	23.8509
3	2300	506000	0.292	9.55	514.8559	28.1366
4	2300	595000	0.336	10.36	604.6563	33.7267

Table A.12: Calculated results based on data available from Qiong et al. [9].

No	Time Average Radiation Heat Transfer (kW)	Indicated Power (kW)	Indicated Power per Piston Area (kW/m^2)
1	0.28684155	5.022716334	639.5121058
2	0.37464906	7.501030565	955.0608742
3	0.44196868	8.525401684	1085.487856
4	0.52977776	10.01238956	1274.817033

Table A.13: Calculated ratios based on data available from Qiong et al. [9].

No	Calculated Ratios Ratio of Time Average Radiation Heat Flux to Indicated Power per Piston Area	Ratio of Time Average Radiation Heat Transfer to Indicated Power
1	0.02855442	0.057108849
2	0.02497317	0.049946345
3	0.0259207	0.051841391
4	0.02645611	0.052912221
Mean	0.0264761	0.052952201

Table A.14: Selected data obtained during radiation measurements of this study

Condition	Fuel Equivalent Ratio	IMEP (kPa)	Fuel Injected per Cycle (kg/cyc)	Fuel Injected Rate (kg/s)	Energy Injected per Cycle (J/cyc)	Time Average Radiant Heat Flux (kW/m^2)	Time Average Radiation Heat Transfer (kW)	Indicated Power (kW)	Indicated Power per Piston (kW/m^2)	Fuel Energy Rate Injected (kW)
1	0.3029	315.2025	5.14E-06	0.000077094	218.94696	2.2392	0.0172349	1.000759136	260.0420625	3.2842044
2	0.3245	330.6857	5.18E-06	0.000108	220.8384	2.2599	0.01739423	1.458219255	378.9106979	4.6008
3	0.4925	482.3291	8.01E-06	0.00012019	341.32398	7.944	0.06114419	1.531381424	397.9215075	5.120094
4	0.5516	475.2805	6.72E-06	0.00014	286.272	4.3361	0.03337454	2.095836549	544.5922396	5.964

Table A.15: Calculated ratios obtained from this study.

Condition	Ratio of Time Average Radiation Heat Flux to Indicated Power per Piston Area	Ratio of Time Average Radiation Heat Transfer to Indicated Power	Ratio of Time Average Radiation Heat Transfer to Fuel Energy Rate Injected
1	0.008610915	0.017221829	0.005247817
2	0.005964202	0.011928404	0.003780697
3	0.019963736	0.039927472	0.011942005
4	0.007962104	0.015924208	0.005595999
Mean	0.010625239	0.021250478	0.006641629